



NTNU – Trondheim
Norwegian University of
Science and Technology

Seismic Response of Wind Turbines

Time Domain Simulations Including SSI

Jeanett Rørvig

Civil and Environmental Engineering (2 year)

Submission date: June 2014

Supervisor: Amir Kaynia, KT

Norwegian University of Science and Technology
Department of Structural Engineering

Master's Thesis

Seismic Response of Wind Turbines

TIME DOMAIN SIMULATIONS INCLUDING SSI

TRONDHEIM, JUNE 2014

CANDIDATE

JEANETT RØRVIG

SUPERVISOR

AMIR M. KAYNIA

Norwegian University of Science and Technology

Department of Structural Engineering



NTNU – Trondheim
Norwegian University of
Science and Technology

Sammendrag

Denne masteravhandlingen presenterer den seismiske responsen av en parkert vindturbin ut-satt for jord-struktur interaksjon i tidsdomenet. Vindturbinens egenskaper etterligner en V90-3.0MW turbin produsert av Vestas og er montert på et skjørtfundament som etterligner proto-typen installert i Aalborg. Vindturbinen er diskretisert i elementer i analyseprogrammet *ABAQUS/CAE* og responsen i form av forskyvninger, akselerasjoner, skjærkrefter og momenter langs tår-net er beregnet for to sammenlignbare modeller. Bare den horisontale komponenten fra virke-lige jordskjelvmålinger er inkludert i analysene.

Referansemodellen integrerer vindturbinen, fundamentet og jorda i en sammensatt model hvor tårnet er modellert ved bruk av skallelementer. Jorda er validert med hensyn til den teoretiske amplifisering av et homogent jordvolum, mens eksperimentelle resultater er brukt til å valid-ere den numeriske algoritmen for tårnet. En forenklet fjærmodell er etablert i samsvar med tre-steps metoden. Modellen bruker bjelkeelementer til å representere tårnet, mens jorda og fundamentet er representert av to statiske fjærer og en viskøs demper. Alle simuleringene er ut-ført i det linær-elastiske området og fundamentet er antatt å være i full kontakt med jorda under den seismiske belastningen.

Den seismiske responsen fra den forenklete modellen er sammenlignet og evaluert med refer-ansemodellen. Det er vist at den forenklete modellen underestimerer viktige designparametre som skjærkrefter og momenter langs tårnet, men at dynamikken ivaretas. Relevante feilkilder er verdien på dempningskoeffisienten som representerer dempningen i kontaktsonen mellom fundament og jord i tillegg til de frekvensuavhengige stivhetene i fjærene. Den største feilkilden antas likevel å være relatert til bjelkeegenskapene i tårnet, ettersom identiske forskyvninger

oppnås i tårnets bunn og avviket i bunnens rotasjoner er ubetydlige for bjelkens respons. Forbedringer på bjelkemodellen må foretas dersom modellen skal være et troverdig analyseverktøy hvor fokuset er å oppnå virkelige seismiske resultater.

Det er vist at høyere egenmoder dominerer deformasjonsforløpet i tårnet for turbiner i denne størrelsesordenen, mens derimot første mode dominerer responsen for mindre enheter.

Hovedbidraget i denne avhandlingen er en parameterstudie som undersøker endringer i maksimale responser langs tårnet for forskjellige fundamentgeometrier. Fundamentets radius og dybde er uavhengig variert og den samme seismiske eksitasjonen er påført alle simuleringer. Det er vist at en økning i fundamentets fleksibilitet gir større responser i tårnet for alle betraktede fundamentgeometrier. Den tilsvarende "fixed-base" responsen underestimerer betraktelig den seismiske belastningen for visse geometrier. Denne observasjonen illustrerer viktigheten av å inkludere effekten av jord-struktur interaksjon for høye og slanke konstruksjoner, som samsvarer med kravet gitt i Eurokode 8.

Det vises videre at fundamentets radius påvirker den seismiske responsen i større grad enn dybden på grunn av den dominerende svingebevegelsen i tårnet og radiusens dominerende innflytelse på rotasjonsstivheten. Sist, så varieres tårnets høyde for å undersøke endringer i basekrefter og momenter i tillegg til nacelleforskyvninger og akselerasjoner. Det vises at visse kombinasjoner av tårnhøyde, fundamentstivheter og seismisk last kan betydelig forsterke responsen i tårnet.

Summary

This thesis presents the time-domain seismic response of a parked wind turbine with a skirted foundation exposed to soil-structure interaction. The properties of the wind turbine imitate the V90-3.0MW turbine produced by Vestas, while the skirted foundation imitates the prototype installed in Aalborg. The wind turbine is discretized using the finite element program *ABAQUS/CAE* and the response in terms of displacements, accelerations, shear and moments along the tower height is computed using two comparative models. Only the horizontal component of real earthquake measurements is considered in the simulations.

The reference model assembles the wind turbine, the foundation and the soil into a single model where shell elements are used to represent the tower. The soil is validated with respect to theoretical transfer functions for homogeneous soils while seismic experimental results are used to validate the numerical algorithm applied to the tower. A simplified model is established in accordance with the three-step method. The model uses beam elements to represent the tower, while the underlying soil and foundation are represented by two static springs and a viscous dashpot. All simulations are performed in the linearly elastic range and the foundation is assumed bounded to the soil during the seismic excitation.

The seismic response of the simplified model is compared and evaluated to the reference model. It is shown that the simplified model underestimates important design quantities such as shear and moments along the tower, whereas the dynamic oscillations are well represented. Sources of errors are the radiation damping coefficient and the frequency independent spring. The major source of error is assumed to be related to the beam properties in the tower, since identical displacements are obtained in the tower bottom and the deviation in the bottom rotation is shown to be insignificant to the beam response. Improvements must be made to the spring model if the approach should produce real-life reliable results.

It is demonstrated that higher modes are important to the seismic response for wind turbine heights in this range, whereas the first mode dominates the response for smaller units. This suggests that careful considerations regarding seismic design should be taken for the middle tower sections as well, in addition to the base.

The main contribution in this thesis is a parametric study which investigates changes in peak responses along the tower for different foundation geometries. The foundation radius and depth is independently varied and the same seismic excitation is applied to the spring model in all simulations. It is shown that an increase in the flexibility of the foundation gives larger peak responses along the tower for all the geometries considered. The corresponding fixed-base solution is shown to highly underestimate the seismic loads for certain geometries. This observation illustrates the importance of including the effects of soil-structure interaction for tall and slender structures, which is in accordance with the requirement given in Eurocode 8.

It is further shown that the foundation radius influences the seismic behaviour to a larger extent than the depth due to the dominating rocking oscillations and the radius' particularly influence on the rotational stiffness. Lastly, the tower height is varied to investigate changes in base moments and shear forces in addition to nacelle displacements and accelerations. It is demonstrated that certain combinations of tower heights and seismic load can result in large amplifications of all response quantities.

Contents

Sammendrag	i
Summary	iii
Contents	v
List of Figures	ix
List of Tables	xv
List of Symbols & Abbreviations	xvii
Acknowledgment	xx
1 Introduction	1
1.1 Background	1
1.2 Problem Formulation & Objectives	1
1.3 Limitations	3
1.4 Approach	3
1.5 Structure of the Thesis	3
2 Concepts of Wind Turbines, Skirted Foundations & Earthquakes	5
2.1 Wind Turbines	5
2.2 Skirted Foundations	5
2.3 Earthquakes	6
3 Theory	8

3.1	Seismic Response: Equation of Motion for Linear Systems	8
3.2	Seismic Response: Solving the Equation of Motion	11
3.2.1	Time history methods	11
3.2.2	Response Spectrum Methods	17
3.3	Damping	18
3.3.1	Rayleigh damping	19
3.4	Transfer function of linear elastic soil with harmonic ground excitation	21
3.4.1	Uniform Soil without damping	21
3.4.2	Uniform Soil with damping	24
3.5	Soil-Structure Interaction	26
3.5.1	Equivalent System Frequency	27
3.6	Three-Step-Method	27
3.6.1	The superposition theorem	28
3.6.2	Method	29
3.6.3	Dynamic Impedances	30
4	State of the Art	32
4.1	Wind Turbines, Skirted Foundations and SSI	32
4.2	Full-scale Shake Table Test of a Nordtank Wind Turbine	34
5	Numerical Model of Soil	38
5.1	Model Description	38
5.1.1	Results	41
6	Validation of a Nordtank Wind Turbine Model	44
6.1	Experimental Results	44
6.2	Model Description	45
6.3	Model Simplifications & Sources of Errors	48
6.4	Results & Discussion	50
6.5	Parametric Study	53
7	Model of a Vestas 3.0-MW Wind Turbine with a Skirted Foundation	57

7.1	Model Description	57
7.2	Model simplifications	62
7.3	Seismic Load & Eigenmodes	62
8	Simplified FE-models	65
8.1	Static Stiffnesses & Damping of the Bucket Foundation	65
8.1.1	Analytical Formulas	66
8.1.2	Different Soil/Skirt Interface Conditions	70
8.2	Kinematic Interaction of the Skirted Foundation	72
8.3	Spring & Dashpot Model	73
9	Results	77
9.1	Part A: Three-Step Method	78
9.2	Part B: Parametric Study	91
9.2.1	Geometry of the skirted foundation	91
9.2.2	Response for different tower heights	95
9.2.3	Period elongation	96
10	Conclusions & Further Work	99
A	MatLAB Scripts	102
A.1	Theoretical Amplification Function	102
A.2	Fourier Amplitude Spectra	104
A.3	Pseudo-Acceleration Response Spectra	106
B	Additional Theory	111
B.1	Direct Numerical Integration	111
B.2	Derivation of the solution to the harmonic equation of motion $m\ddot{u} + c\dot{u} + ku = P_0 \cos(\omega t)$	114
B.3	Derivation of the Dynamic Impedance Function for a Single Oscillator	116
C	Additional Information	118
C.1	Influence of damping on seismic response	118

C.2 EC8 Concepts 118

D Additional Results 122

D.1 Validation of the Soil 122

D.2 Validation of Nordtank Wind Turbine Model 123

D.3 Time history seismic response of the spring model 125

D.4 Stiffnesses of the Skirted Foundation with varying geometry 143

Bibliography 144

Bibliography 144

List of Figures

1.1	Global cumulative installed wind capacity [4].	2
2.1	Components of a wind turbine [23].	6
2.2	Skirted foundation components and installation [21].	7
3.1	Dynamic systems.	9
3.2	L-frame with 2-DOF	10
3.3	Variation of modal damping ratio ξ with frequency.	21
3.4	Plot of the five first modeshapes of a uniform linear elastic soil	24
3.5	Theoretical amplification factor for uniform linear elastic soil for different V_s and damping ratios ξ	25
3.6	Kinematic interaction with free-field motion indicated by dashed lines	26
3.7	Excitation of rocking in embedded foundations by vertically propagating S-waves.	27
3.8	Superposition theorem	29
3.9	The three-step method	30
4.1	Shake-table test from 2004	35
4.2	Shake-table test from 2010	36
5.1	Behaviour of soil and water near the boundaries subjected to seismic excitation.	39
5.2	Applied tie constraints in the soil model	40
5.3	Different soil meshes.	41
5.4	The six first eigenmodes of the homogenous linear-elastic soil model.	42

5.5	Amplification of soil with harmonic base excitation, 5 % Rayleigh damping, $V_s = 300$ m/s and linear elements. The purple dots indicates the maximum displacement from the steady-state phase from a time-domain simulation.	43
5.6	Time domain response of a soil with a base excitation with frequencies $f = 1.5050 Hz$ (1 st natural frequency) and $f = 2.0 Hz$ with 5 % damping.	43
6.1	Observed 1 st tower mode shapes [24]	45
6.2	Observed 2 nd tower mode shapes [24]	45
6.3	The two FE-models of the 65-kW Nordtank wind turbine	46
6.4	Applied constraints to the Nordtank wind turbine model.	49
6.5	The six first modeshapes and corresponding eigenfrequency of model 1.	51
6.6	Acceleration time serie, Fourier amplitude spectra and response acceleration spectra ($\beta = 5\%$) for the normal component of the Landers earthquake.	52
6.7	Localization of output sections and points	53
6.8	Experimental acceleration time history response of the Nordtank wind turbine. . .	54
6.9	Acceleration time response of the shell model for <i>a</i>) model 1 which explicitly represent the nacelle and blades and <i>b</i>) model 2 which has a lumped mass representation of the nacelle and blades	55
6.10	Change in the first natural frequency for different model parametres.	56
7.1	Sketch of the different parts of the wind turbine and skirted foundation [15].	58
7.2	Stress field in bucket and soil with a <i>contact</i> formulation. A unit moment is applied at the top lid.	59
7.3	Model of the Vestas wind turbine mounted in soil.	60
7.4	Visualization of the skin elements in the soil.	60
7.5	Acceleration time serie, Fourier amplitude spectra and response acceleration spectra ($\beta = 5\%$) of the horizontal component of the Nahanni earthquake.	63
7.6	Output nodes and eigenfrequencies of the wind turbine tower.	64
8.1	Displacements for a unit force and moment at the bucket foundation. Scale $1 \cdot 10^{10}$	66
8.2	Comparison of the horizontal and rocking deformation between the analytical rigid embedded foundation and the partly deformable bucket foundation.	67

8.3	Variation of static stiffnesses in a homogenous soil.	69
8.4	Inner soil layer modeling the soil/skirt interface conditions.	70
8.5	Static stiffnesses for varying soil/bucket interface conditions. Outer soil has elasticity $E = 200MPa$ and $V_S = 200\frac{m}{s}$	71
8.6	Kinematic base input in the spring and dashpot model for the Nahani earthquake	73
8.7	The three-step method for the skirted foundation and wind turbine.	74
8.8	Numerical procedure to create a spring model in accordance to the three-step-method.	74
8.9	The two first fore-aft eigenfrequencies of the Vestas wind turbine.	76
9.1	The model setups for the comparisons.	78
9.2	A homogenous and a layered soil stratum used in the comparison between the shell model and the three-step-method.	79
9.3	Horizontal time history displacement for the fully integrated model the a spring model for the stiff soil condition.	81
9.4	Acceleration along the tower for the fully integrated model and the spring model for the stiff soil condition.	81
9.5	Moment along the tower for the full model and the spring model for the stiff soil condition.	82
9.6	Shear forces along the tower for the fully integrated model and the spring model for the stiff soil condition.	82
9.7	Accuracy of the spring model bottum displacement and rotation compared to the reference shell model.	83
9.8	Deformation profiles during seismic excitation for the two soil deposits.	84
9.9	Close up of the skirted foundation during seismic excitation for the two soil deposits.	84
9.10	Comparison of the spring input translation and rotation against the bottum beam node. The graphs shows the inertial interaction for the two soil profiles.	85
9.11	Displacements for a stiff and a soft soil; (1) a homogeneous soil with $V_S = 200\frac{m}{s}$ and (2) a three-layered soil with $V_S = 50\frac{m}{s}$ for the weakest upper layer.	86

9.12 Accelerations for a stiff and a soft soil; (1) a homogeneous soil with $V_S = 200 \frac{m}{s}$ and (2) a three-layered soil with $V_S = 50 \frac{m}{s}$ for the weakest upper layer.	86
9.13 Moments for a stiff and a soft soil; (1) a homogeneous soil with $V_S = 200 \frac{m}{s}$ and (2) a three-layered soil with $V_S = 50 \frac{m}{s}$ for the weakest upper layer.	87
9.14 Shear forces for a stiff and a soft soil; (1) a homogeneous soil with $V_S = 200 \frac{m}{s}$ and (2) a three-layered soil with $V_S = 50 \frac{m}{s}$ for the weakest upper layer.	87
9.15 Displacements for (a) a fixed base and (b) a flexible base for the stiff soil condition.	88
9.16 Accelerations for (a) a fixed base and (b) a flexible base for the stiff soil condition. .	89
9.17 Moments for (a) a fixed base and (b) a flexible base for the stiff soil condition. . . .	89
9.18 Shear forces for (a) a fixed base and (b) a flexible base for the stiff soil condition. .	90
9.19 Swaying and rocking static stiffnesses for different bucket depths and radius. . . .	92
9.20 Changes in peak response quantities along the tower as a function of foundation radius R . The same spring input motion is applied in all cases.	94
9.21 Changes in peak response quantities along the tower as a function of foundation depth D . The same spring input motion is applied in all cases.	94
9.22 Change in peak responses as a function of a geometric foundation changes relative to the reference geometry ($D = R = 6m$). The variables D and R are independently varied.	95
9.23 Maximum responses for varying tower height.	98
9.24 Natural frequency elongation as a function of tower/foundation stiffness ratio. The first graph studies changes in bucket geometry and the second studies changes in tower height.	98
B.1 Linear acceleration in Newmark's method	112
B.2 The response $u_p = \rho e^{i(\omega t - \theta)}$ drawn in an Argand diagram.	116
B.3 Dynamic stiffness and damping coefficients of a 1-DOF oscillator.	117
C.1 Influence of damping on seismic response for different earthquake records. A critical modal damping ratio of 5% and 0.5% of the first modes are used.	120
C.2 Classification of ground types according to EC8 [22].	121

D.1 Amplification of homogeneous soil with harmonic base excitation, 5 % Rayleigh damping, $V_s = 300$ m/s and quadratic tetrahedron elements.	122
D.2 Displacement time response of the shell model for <i>a</i>) model 1 which has a lumped mass representation of the nacelle and blades and <i>b</i>) model 2 which explicitly represent the nacelle and blades	124
D.3 Displacements along the tower for the full model and the spring model for the soft soil condition.	126
D.4 Accelerations along the tower for the full model and the spring model for the soft soil condition.	126
D.5 Moments along the tower for the full model and the spring model for the soft soil condition.	127
D.6 Shear forces along the tower for the full model and the spring model for the soft soil condition.	127
D.7 Time history displacement along the tower for 1) kinematic spring input and 2) free-field input.	128
D.8 Time history acceleration along the tower for 1) kinematic spring input and 2) free-field input.	129
D.9 Time history displacements along the tower for 1) translational and rotational spring input (U+UR) and 2) only translational spring input (U).	130
D.10 Time history acceleration along the tower for 1) translational and rotational spring input (U+UR) and 2) only translational spring input (U).	131
D.11 Time history displacement along the tower for 1) a fixed-base configuration and 2) a flexible base configuration.	132
D.12 Time history accelerations along the tower for 1) a fixed-base configuration and 2) a flexible base configuration.	133
D.13 Time history moments along the tower for 1) a fixed-base configuration and 2) a flexible base configuration.	134
D.14 Time history shear forces along the tower for 1) a fixed-base configuration and 2) a flexible base configuration.	135
D.15 Nacelle displacements for different bucket radius.	137

D.16 Nacelle accelerations for different bucket radius. 137

D.17 Base moment for different skirt radius. 138

D.18 Base shear for different skirt radius. 138

D.19 Nacelle displacements for different bucket depths. 139

D.20 Nacelle accelerations for different bucket depths. 139

D.21 Base moments for different skirt depths. 140

D.22 Base shear for different skirt depths. 140

D.23 Nacelle time history acceleration for different tower heights. 141

D.24 Nacelle time history acceleration for different tower heights. 141

D.25 Base moment (time history) for different tower heights. 142

D.26 Base shear (time history) for different tower heights. 142

List of Tables

3.1	Overview of the analysis methodologies	12
4.1	Summary of experimentally and numerically obtained eigenfrequencies of the parked 65-kW wind turbine. The numerical result represent model 2.	37
5.1	Material properties of modelled soil	39
5.2	Natural frequencies of soil for elements C3D8R (linear), C3D20R (quadratic) and C3D10 (quadratic).	41
6.1	Summary of the modal properties of the parked 65-kW wind turbine ¹⁾ [24]	46
6.2	Properties of the experimental 65-kW wind turbine subjected to the shake table test. The data is also transferred to the FE-model in <i>ABAQUS</i> [25, 24]	47
6.3	Material properties and element types in the FE-model in <i>ABAQUS</i>	47
6.4	Mesh properties	48
6.5	Eigenfrequencies obtained from two different models; one model including hub and blades and one with a lumped top mass.	50
7.1	Properties of the Vestas V90 3.0 MW wind turbine [2, 15].	59
7.2	Properties of the bucket foundation [15].	61
7.3	Material properties in the fully integrated model.	61
7.4	Mesh properties Vestas wind turbine model.	62
7.5	The two first natural frequencies of a parked V90 3.0 MW wind turbine installed at the bucket foundation [15]. Compared to a FE-beam model.	63

8.1	Static stiffnesses of rigid embedded cylindrical foundation welded into a homogenous soil stratum-over-bedrock	67
8.2	Static stiffnesses of bucket foundation compared to formulas for varying soil elasticity in a homogenous soil stratum-over-bedrock.	70
8.3	Static stiffnesses of bucket foundation for varying interface conditions. The outer soil layer has an elasticity of $E = 200MPa$	71
8.4	Frequency-independent damping coefficients of rigid embedded cylindrical foundation welded into a homogenous soil stratum-over-bedrock	72
9.1	Soil material properties	79
D.1	Static stiffnesses of the bucket foundation for different skirt radius and constant bucket depth of $D=6m$. $E = 50MPa$ and $V_S = 100\frac{m}{s}$	143
D.2	Static stiffnesses of the bucket foundation for different skirt depths and constant bucket radius of $R=6m$. $E = 50MPa$ and $V_S = 100\frac{m}{s}$	143

List of Symbols & Abbreviations

Small latin letters

f	Frequency
k	Stiffness
m	Mass
u	Total displacement
z	Height coordinate

Large latin letters

\tilde{C}	Modal damping
H	Height
\tilde{K}	Modal stiffness
\tilde{L}	vv
\tilde{M}	Modal mass
N	Number of degrees of freedom
T	Period
U	Translational displacement obtained in <i>Abaqus</i>
UR	Rotation obtained in <i>ABAQUS</i>
V_S	Shear wave velocity

Greek symbols

ξ	Relative modal damping
ω	Frequency in Hz
ω_n	Natural frequency
η	Modal coordinate related to expansion of the displacement vector
Σ	Summation symbol
Γ	Modal coordinate related to the expansion of the effective earthquake forces

Bold symbols

Bold symbols are used as matrix or vector notation.

s	Spatial distribution of the effective earthquake forces
u	Relative displacement vector
u_g	Ground displacement vector
u_t	Total displacement vector
1	Unit vector
0	Zero vector
f_I	Inertia forces vector
f_D	Damping forces vector
f_S	Internal forces vector
K	Stiffness matrix
\tilde{K}	Modal stiffness matrix
C	Damping matrix
\tilde{C}	Modal damping matrix
M	Mass matrix
\tilde{M}	Modal mass matrix
ι	Influence vector
η	Modal coordinate vector
φ	Natural mode shape vector

Φ	Natural mode shape matrix
Γ	Modal coordinate vector

Abbreviations

DOF	Degree-of-freedom
FEM	Finite element method
Joint	A point along the wind turbine tower
Link	A connector type in <i>ABAQUS</i> which constrains all selected translational DOF to a master point
MDOF	Multi degree-of-freedom
MPC	Multi-point constraint
Node	A coordinate in a FE-mesh where DOFs are defined
PEER	Pacific Earthquake Engineering Research center
SDOF	Single degree-of-freedom
SSI	Soil-structure interaction

Acknowledgment

Acknowledgement must be given to my supervisor Amir M. Kaynia for all his help and support during the work with this thesis.

J.R.

Chapter 1

Introduction

1.1 Background

The global cumulative energy from wind turbines continues to increase as shown in figure 1.1. More than 350 000 MW is installed world-wide at the end of 2013 and the technology is now also considered used in seismic active zones in North America, China, India and other countries. This makes wind energy to an increasingly important energy source that is essential to maintain electrical power supply.

Hence, during the possible event of an earthquake, it is important to assure a maximum of safety for the power supply and reduce potential damages of wind turbines to a minimum. A damaged wind turbine causes direct cost related to the repairs in addition to the indirect costs related to the disturbance in the electric power supply. It is hence crucial to understand the seismic behaviour of wind turbines such that preventive seismic design can be implemented.

1.2 Problem Formulation & Objectives

This thesis focuses on the global seismic response of the wind turbine tower. A particular problem of interest is how the *soil-structure interaction* influences the seismic response. Soil-structure

interaction (SSI) is the process in which the soil influences the response of the structure and vice versa. Eurocode 8 (EC8) requires that SSI is included in seismic simulations for tall and slender structures. Wind turbine towers are indeed tall and slender structures, which could make SSI to an important factor for the seismic response. This motivated for closer investigation of the SSI-problem.

Including SSI in numerical simulations generally increases the complexity of the model. Therefore, the main aim is to develop a *simplified* model which includes this interaction such that parametric studies can effectively be carried out. It is interesting to investigate how changes in the foundation geometry or the tower's height influence the peak structural responses along the tower and in which cases SSI-effects can be ignored.

The main objectives of this Master's thesis are:

1. Establish a fully integrated FE-model consisting of soil, foundation and a wind turbine and validate each part against theoretical solutions or experimental results.
2. Establish a simplified FE-model which includes the effects of SSI.
3. Study the importance of kinematic interaction for the skirted foundation.
4. Investigate the importance of SSI compared to a fixed-base configuration.
5. Examine how changes in the geometry of the skirted foundation and the tower's height influence relevant peak structural responses.

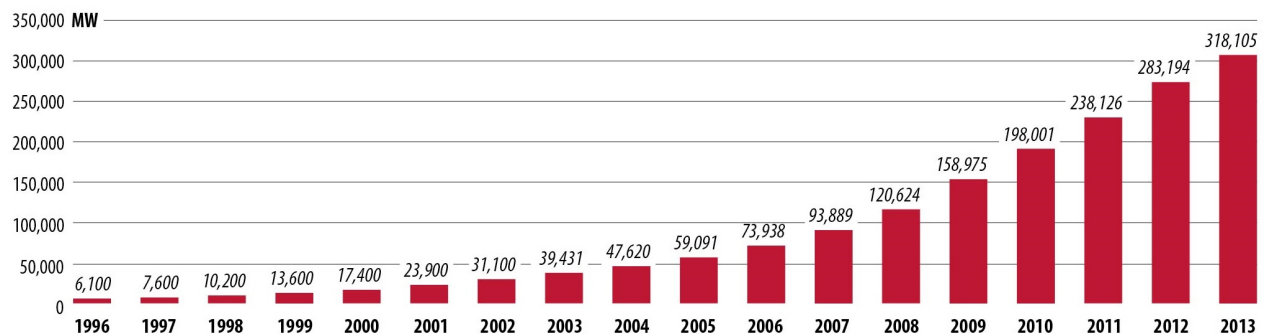


Figure 1.1: Global cumulative installed wind capacity [4].

1.3 Limitations

The numerical results are limited to the linearly elastic range for both the wind turbine tower, the skirted foundation and the soil. Further, the foundation is assumed bounded to the soil, which prevents sliding and occurrence of gaps in the foundation/soil interface. Rayleigh damping is used to represent material damping. Static spring stiffnesses and a viscous dashpot representing the radiation damping is applied in the simplified models.

The seismic response is computed for the horizontal component of the 1985 Nahanni earthquake if nothing else is specified. Thus, the response from earthquakes with a different frequency content or magnitudes are not investigated.

1.4 Approach

The numerical models are established in the finite element program *ABAQUS/CAE*. To ensure that the established models behave in a realistic manner, the separate parts (i.e the tower and the soil) are validated with respect to theoretical or experimental results.

Two different real-life wind turbines from the wind turbine producers Vestas and Nordtank are used as reference for the geometry and mass properties in the models. There exists no *detailed* information freely available about these properties. Consequently, several approximations and simplifications are adopted to the models.

1.5 Structure of the Thesis

The thesis is structured as follows:

- *Chapter 2; Concepts of Wind Turbines, Skirted foundations & Earthquakes* introduces the most important terminology and concepts related to wind turbines, skirted foundations and earthquakes.

- *Chapter 3; Theory* presents the dynamic equations related to seismic excitation of MDOF-systems and selected solution procedures.
- *Chapter 4; State of the Art* presents the most relevant research related to wind turbines, skirted foundations and SSI.
- *Chapter 5; Numerical Model of Soil* presents and validates a linearly elastic numerical model of a homogeneous soil profile.
- *Chapter 6; Validation of the Nordtank Wind Turbine Model* validates the numerical algorithm applied to the wind turbine tower against experimental results.
- *Chapter 7; Model of a Vestas 3.0-MW Wind Turbine with a Skirted Foundation* presents a fully integrated model consisting of the soil, skirted foundation and the wind turbine.
- *Chapter 8; Simplified FE-models* presents a simplified spring and dashpot model developed in accordance with the three-step-method.
- *Chapter 9; Results* is divided into two parts. Part A compares the accuracy of the simplified model with respect to the fully integrated model. Response in terms of accelerations, displacements, shear forces and moments are computed in the time domain for several points along the wind turbine tower. Effect of soil-structure interaction is studied for two soil profiles. Part B is a parametric study which studies the change in peak responses for different foundation geometries and tower heights.
- *Chapter 10; Conclusions & further Work* presents the conclusions obtained from the results provided in chapter 9 and answers the problem definition defined. Lastly, suggestions to further work is proposed.

Additional theory, MatLAB scripts and results are provided in the appendix. Note that some results supporting the conclusions made is found here to reduce the amount of graphs in the main text.

Chapter 2

Concepts of Wind Turbines, Skirted Foundations & Earthquakes

2.1 Wind Turbines

Figure 2.1 provides a sketch of the main parts in the wind turbine; the tower, nacelle, hub and blades. The blades capture the energy from the wind and spins a generator in the nacelle. The nacelle contains all the machinery and hence stands for a large part of the total weight. The hub is fixed to the rotor shaft which drives the generator through a gearbox.

2.2 Skirted Foundations

Figure 2.2 provides sketches of the different components of a skirted foundation. The foundation consists roughly of a skirt penetrating the seabed and a top lid where the superstructure is mounted. The skirt is made of hollow cylindrical concrete or steel walls connected to the tower through stiffeners as seen in figure 2.2b. The loads from the superstructure are transmitted into deeper and stronger soil strata by friction forces and skirt tip forces.

The skirted foundation is often installed into the soil by suction as illustrated in figure 2.2c. By

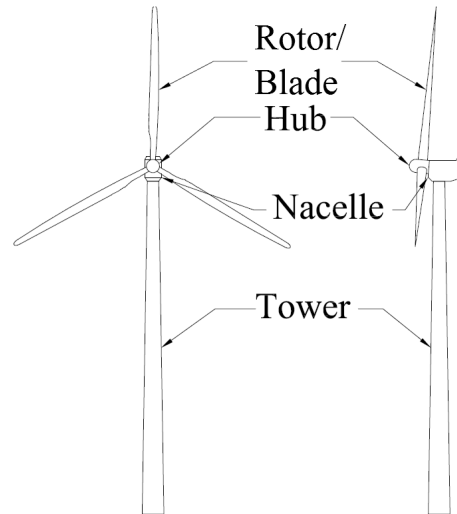


Figure 2.1: Components of a wind turbine [23].

lowering the water pressure inside the skirt, a water flow is generated flowing from the outside to the inside of the skirt. The flow reduces the stresses at the skirt tip and reduces the penetration resistance during installation. Skirted foundations are extensively used as anchors and foundations of offshore platforms in deep water and are currently being considered as possible foundations for offshore wind turbines [14].

Skirted foundations provide a reduction up to 50 % in steel weight compared to traditional monopile solutions in addition to the easy installation [16]. This makes large skirted foundations for offshore wind turbines an upcoming cost-effective technology. Structural buckling during installation is a relevant risk for such foundations and is further studied by Madsen [21].

2.3 Earthquakes

An earthquake is the result of a sudden release of energy in the earth's crust that creates seismic waves. The waves propagate through the soil medium as shear and pressure waves and their amplitudes can either increase or decrease depending on the soil material properties. For example, the 1985 Mexico City earthquake were amplified by over a factor of five due to the local soil properties [28]. Hence, the determination of realistic free-field surface motions is of strongest importance in the seismic design of any structure.

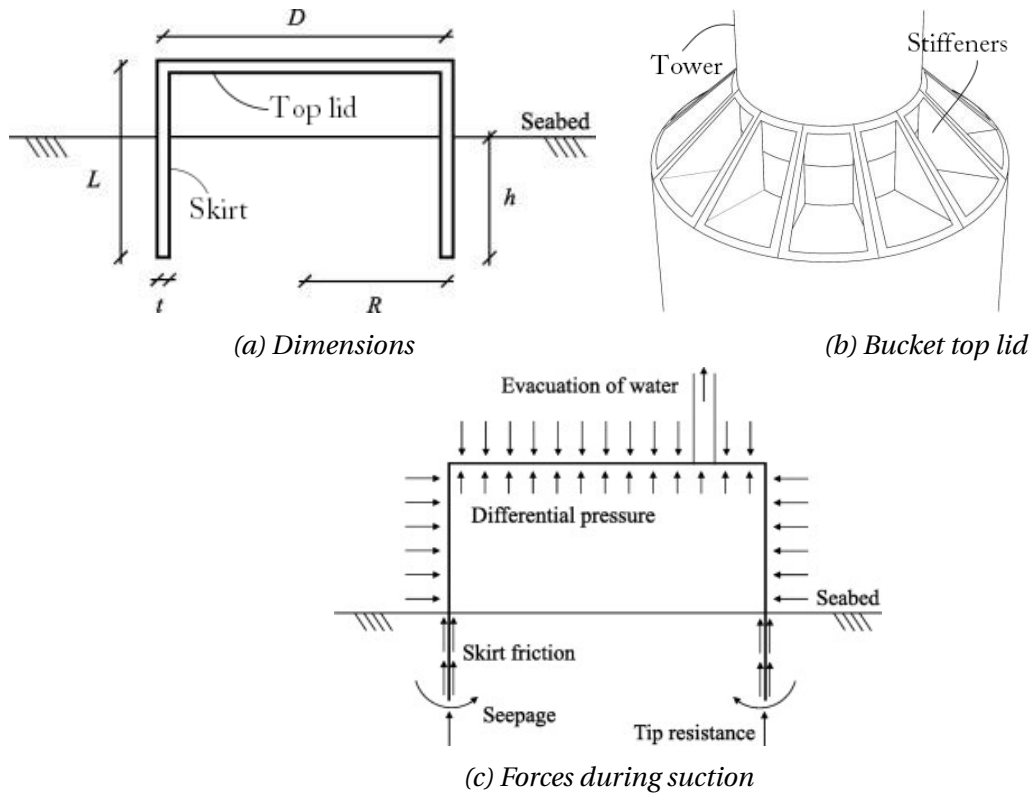


Figure 2.2: Skirted foundation components and installation [21].

A commonly used approach to site response analysis is the concept of transfer functions [20]. A transfer function gives the ratio between the steady-state harmonic response of two points as a function of frequency. This approach is later used as a validation tool for the numerical soil model. Free-field motions for more realistic soil profiles can be computed using for example SHAKE2000 software [12].

Chapter 3

Theory

3.1 Seismic Response: Equation of Motion for Linear Systems

This section presents the equation of motion for linear systems subjected to seismic loadings. All theory presented originate from Chopra [3]. The *general* equation of motion for a single degree of freedom system (SDOF) is given as

$$f_I + f_D + f_S = p(t) \quad (3.1)$$

where f_I is the inertia force related to the total acceleration \ddot{u}_t of the mass m , f_D is the damping force, f_S is the internal force in the structure due to the *relative* displacements of the structure and $p(t)$ is an external force. An example of a SDOF-system is shown in figure 3.1a; a cantilevered beam with a concentrated top mass m and stiffness k .

One important application of structural dynamics is to predict base moments and shear in the structure during a seismic event. Knowing the total displacement of the structure is useful to provide enough separation between adjacent buildings to prevent their pounding against each other. The total accelerations are relevant if the structure is supporting sensitive equipment as is the case with wind turbines.

The internal forces are linearly related to the displacement u when the displacement does not

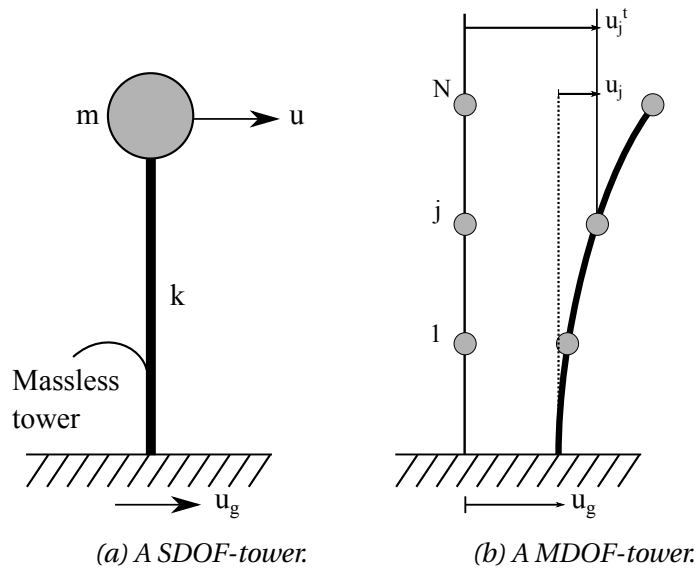


Figure 3.1: Dynamic systems.

exceeds the linear elastic range. Assuming viscous damping the equation of motion for a SDOF-system can further be expressed as

$$m\ddot{u}_t + c\dot{u} + ku = p(t) \quad (3.2)$$

For a system subjected to seismic loading the total displacement is decomposed into a relative displacement u and the ground displacement u_g such that

$$m(\ddot{u} + \ddot{u}_g) + c\dot{u} + ku = 0 \quad (3.3a)$$

$$m\ddot{u} + c\dot{u} + ku = -m\ddot{u}_g \quad (3.3b)$$

Adapting the dynamic properties $k = \omega_n^2 m$ and $c = 2\xi\omega_n m$ give

$$\ddot{u} + 2\xi\omega_n\dot{u} + \omega_n^2 u = -\ddot{u}_g(t) \quad (3.4)$$

All structures have an infinite number of degrees-of-freedom, but only a finite number is needed to accurately describe the dynamic response. The dynamic equations for multi-degree-of-freedom structures (MDOF) are first established for a case where all the dynamic degrees of freedom are displacements in the same direction as the ground motion as the tower shown in figure 3.1b. Later a more general approach is derived. The total displacement for each degree of freedom is expressed in vector form as

$$\mathbf{u}_t(t) = u_g \mathbf{1} + \mathbf{u}(t) \quad (3.5)$$

where $\mathbf{1}$ is a vector of order N (number of DOF) with each element equal to unity. The equations in (3.3) is expressed for a MDOF-system under the given conditions as

$$\mathbf{m}(\ddot{\mathbf{u}} + \ddot{\mathbf{u}}_g) + \mathbf{c}\dot{\mathbf{u}} + \mathbf{k}\mathbf{u} = \mathbf{0} \quad (3.6a)$$

$$\mathbf{m}\ddot{\mathbf{u}} + \mathbf{c}\dot{\mathbf{u}} + \mathbf{k}\mathbf{u} = -\mathbf{m}\mathbf{1}\ddot{u}_g(t) \quad (3.6b)$$

where \mathbf{m} is the mass matrix, \mathbf{c} is the damping matrix and \mathbf{k} is the stiffness matrix. A generalization of the preceding derivation is useful for structures where not all the DOFs are in the same direction as the seismic excitation. The L-shaped frame in figure 3.2 illustrates such a system. In this approach the total displacement of each mass can be represented as

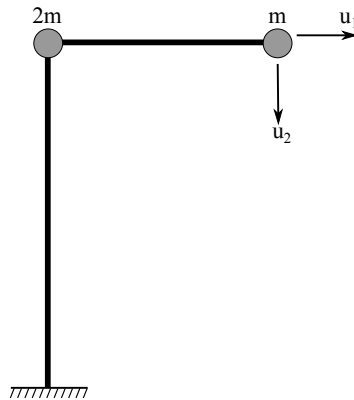


Figure 3.2: L-frame with 2-DOF

$$\mathbf{u}^t(\mathbf{t}) = \boldsymbol{\iota} u_g(t) + \mathbf{u}(t) \quad (3.7)$$

where the *influence* vector $\boldsymbol{\iota}$ represent the displacement of the masses resulting from static application of a unit ground displacement. For the L-frame the influence vector reads $\boldsymbol{\iota} = \begin{bmatrix} 1 & 0 \end{bmatrix}^T$ since the vertical DOF is not affected by the horizontal ground displacement. The equation of motion for this general approach is then

$$\mathbf{m}\ddot{\mathbf{u}} + \mathbf{c}\dot{\mathbf{u}} + \mathbf{k}\mathbf{u} = -\mathbf{m}\boldsymbol{\iota}\ddot{u}_g(t) \quad (3.8)$$

3.2 Seismic Response: Solving the Equation of Motion

The response of a system subjected to dynamic loading can be obtained in the time-domain (RHA) or in the frequency domain (RSA). An RSA analysis concerns the computation of the *peak* response of a structure during an earthquake *directly* from the earthquake response (or design) spectrum. The method is not exact, but provides sufficiently accurate results for structural design applications.

3.2.1 Time history methods

This section focuses mainly on the *modal* method used to determine the response of a MDOF-system. Only a brief introduction is given to the *direct* method. Table 3.1 gives an overview of the area of application and their solution for the two time-domain analysis methodologies. Modal analysis can only be applied to linear systems with classical damping.

The modal method

The modal method utilize the *orthogonality* properties of the modes to reduce a MDOF-system to n sets of SDOF-systems. Mathematically stated, any set of N independent vectors can be

Table 3.1: Overview of the analysis methodologies

	Modal Analysis	Direct Analysis
Characteristics	$\tilde{\mathbf{M}}\{\ddot{\eta}\} + \tilde{\mathbf{C}}\{\dot{\eta}\} + \tilde{\mathbf{K}}\{\eta\} = \tilde{\mathbf{R}}^{\text{ext}}$	$\mathbf{M}\{\ddot{\mathbf{u}}\} + \mathbf{C}\{\dot{\mathbf{u}}\} + \mathbf{K}\{\mathbf{u}\} = \mathbf{R}^{\text{ext}}$
Application	<ul style="list-style-type: none"> • Linear systems • Classical damping 	<ul style="list-style-type: none"> • Linear or non-linear systems • Classical or non-classical damping
Solution	<ul style="list-style-type: none"> • Simple excitation: Closed form • Complex excitation: Numerical 	<ul style="list-style-type: none"> • Numerical

used as a basis for representing any other vector of order N . The natural modes φ_i of a dynamic system are independent, and thus any displacement vector u can be represented by a modal expansion as

$$\mathbf{u}(t) = \sum_{i=1}^n \varphi_i \eta_i(t) = \mathbf{\Phi} \boldsymbol{\eta} \quad \text{where } i = 1, 2, \dots, n_{dof} \quad (3.9)$$

where φ_i is the i -th natural mode shape and η_i is the i -th modal coordinate. The natural mode shapes represent the nodal displacements *relative* to other nodes and the modal coordinates are scalars and adjust the *amplitude* of the modes.

The same principle is used to expand the inertia forces $\mathbf{M}\mathbf{t}$ into a summation of the modal inertia forces as

$$\mathbf{M}\mathbf{t} = \sum_{n=1}^N \mathbf{s}_n = \sum_{n=1}^N \Gamma_n \mathbf{M}\varphi_n = \mathbf{M}\mathbf{\Phi}\mathbf{\Gamma} \quad \text{where } i = 1, 2, \dots, n_{dof} \quad (3.10)$$

where \mathbf{s}_n is the spatial distribution of the effective earthquake forces, Γ_n is the n -th modal coordinate adjusting the contribution of the n -th modal inertia force $\mathbf{M}\varphi_n$. Premultiplying both sides by φ_r^T and utilizing the orthogonality property of modes gives

$$\varphi_r^T \mathbf{M} \mathbf{u} = \varphi_r^T \sum_{n=1}^N \Gamma_n \mathbf{M} \varphi_n = \Gamma M_n \quad \text{since} \quad \varphi_r^T \mathbf{M} \varphi_n = 0 \quad \text{for} \quad n \neq r \quad (3.11)$$

Hence

$$\Gamma_n = \frac{\tilde{L}_n}{M_n} \quad \tilde{L}_n = \varphi_n^T \mathbf{M} \mathbf{u} \quad M_n = \varphi_n^T \mathbf{M} \varphi_n \quad (3.12)$$

The modal contribution \mathbf{s}_n represents the contribution of mode n to the total excitation vector $\mathbf{M} \mathbf{u}$ and is independent of how the modes are normalized.

The modal SDOF equation for a seismic system is obtained by substituting the modal expansions for both the displacement and the inertia force vector in equation 3.8 and premultiply by Φ^T . Thus

$$\underbrace{\Phi^T \mathbf{M} \Phi}_{\tilde{\mathbf{M}}} \cdot \ddot{\boldsymbol{\eta}} + \underbrace{\Phi^T \mathbf{C} \Phi}_{\tilde{\mathbf{C}}} \cdot \dot{\boldsymbol{\eta}} + \underbrace{\Phi^T \mathbf{K} \Phi}_{\tilde{\mathbf{K}}} \cdot \boldsymbol{\eta} = \underbrace{-\Phi^T \mathbf{M} \Phi \Gamma}_{\tilde{\mathbf{R}}^{\text{ext}}} \ddot{u}_g \quad (3.13)$$

Using the notation indicated, the *modal equation* is expressed as

$$\tilde{\mathbf{M}}\{\ddot{\boldsymbol{\eta}}\} + \tilde{\mathbf{C}}\{\dot{\boldsymbol{\eta}}\} + \tilde{\mathbf{K}}\{\boldsymbol{\eta}\} = \tilde{\mathbf{R}}^{\text{ext}} \quad (3.14)$$

where the content in each matrix is given in equation (3.15), (3.16) and (3.17).

$$\begin{aligned}
\tilde{\mathbf{M}} &= \begin{bmatrix} \tilde{M}_1 & 0 & \cdots & 0 \\ 0 & \tilde{M}_2 & \cdots & 0 \\ \vdots & \vdots & \ddots & 0 \\ 0 & 0 & 0 & \tilde{M}_n \end{bmatrix} = \text{diag} [\tilde{M}_i] & \tilde{\mathbf{C}} &= \begin{bmatrix} \tilde{C}_1 & 0 & \cdots & 0 \\ 0 & \tilde{C}_2 & \cdots & 0 \\ \vdots & \vdots & \ddots & 0 \\ 0 & 0 & 0 & \tilde{C}_n \end{bmatrix} = \text{diag} [\tilde{C}_i] \\
\tilde{\mathbf{K}} &= \begin{bmatrix} \tilde{K}_1 & 0 & \cdots & 0 \\ 0 & \tilde{K}_2 & \cdots & 0 \\ \vdots & \vdots & \ddots & 0 \\ 0 & 0 & 0 & \tilde{K}_n \end{bmatrix} = \text{diag} [\tilde{K}_i] & \text{where } \tilde{M}_i &= \varphi_i^T \mathbf{M} \varphi_i \\
& & \text{where } \tilde{K}_i &= \varphi_i^T \mathbf{K} \varphi_i \\
& & \text{where } \tilde{C}_i &= \varphi_i^T \mathbf{C} \varphi_i
\end{aligned} \tag{3.15}$$

$$\Phi = \begin{bmatrix} \varphi_1 & \varphi_2 & \cdots & \varphi_n \end{bmatrix} = \begin{bmatrix} \varphi_{11} & \varphi_{12} & \cdots & \varphi_{1n} \\ \varphi_{21} & \varphi_{22} & \cdots & \varphi_{2n} \\ \vdots & \vdots & \ddots & \vdots \\ \varphi_{n1} & \varphi_{n2} & \cdots & \varphi_{nn} \end{bmatrix} \quad \eta = \begin{bmatrix} \eta_1 \\ \eta_2 \\ \vdots \\ \eta_n \end{bmatrix} \tag{3.16}$$

$$\begin{aligned}
\tilde{\mathbf{R}}^{\text{ext}} &= \begin{bmatrix} \tilde{M}_1 \Gamma_1 \\ \tilde{M}_2 \Gamma_2 \\ \vdots \\ \tilde{M}_n \Gamma_n \end{bmatrix} \quad \ddot{u}_g = \begin{bmatrix} \tilde{L}_1 \\ \tilde{L}_2 \\ \vdots \\ \tilde{L}_n \end{bmatrix} \quad \ddot{u}_g & \text{where } \Gamma_i &= \frac{\tilde{L}_i}{M_i} \\
& & \tilde{L}_i &= \varphi_i^T \mathbf{M} \mathbf{t}
\end{aligned} \tag{3.17}$$

The equivalent SDOF-system for the n -th mode is

$$m_n \ddot{q}_n + 2m_n \xi \omega_n \dot{q}_n + m_n \omega_n^2 q_n = \tilde{L}_n \ddot{u}_g \tag{3.18a}$$

$$\ddot{q}_n + 2\xi_n \omega_n \dot{q}_n + \omega_n^2 q_n = -\Gamma_n \ddot{u}_g(t) \tag{3.18b}$$

The factor Γ_n is sometimes called a *modal participation factor* even if it is not a measure of the contribution of the mode to a response quantity nor is it independent of the normalization of the modes. These drawbacks are overcome by the *modal contribution factor* \bar{r}_n later presented.

The solution to equation (3.18b) is written in terms of the response of a SDOF-system with unit mass

$$\ddot{D}_n + 2\xi_n\omega_n\dot{D}_n + \omega_n^2 D_n = -\ddot{u}_g \quad (3.19)$$

and identical natural frequency ω_n and damping ξ_n as the seismic n -th mode SDOF system. Comparing equation (3.18b) and (3.19) it is seen that the solution q_n is related to D_n by

$$q_n(t) = \Gamma_n D_n(t) \quad (3.20)$$

Thus, the solution to a MDOF-system subjected to seismic loading is found by first solving a SDOF-system with unit mass and equal natural frequency ω_n and damping ξ_n and multiply by the modal participation factor Γ_n . This is truly a smart approach, as solutions to SDOF-systems are available for harmonic, step and impulsive forces.

The equivalent static force associated with the n -th mode response is

$$\mathbf{f}_n(t) = \mathbf{k}\mathbf{u}_n(t) = \omega_n^2 \mathbf{m}\varphi_n q_n(t) = \underbrace{\mathbf{m}\varphi_n \Gamma_n}_{\mathbf{s}_n} \omega_n^2 D_n = \mathbf{s}_n \omega_n^2 D_n \quad (3.21)$$

The n -th mode contribution to any response quantity $r(t)$ is determined by static analysis

$$r_n(t) = r_n^{st} \left[\omega_n^2 D_n(t) \right] \quad (3.22)$$

where r_n^{st} is the modal static response. Combining the response contributions of all modes gives the total response

$$r(t) = \sum_{n=1}^N r_n(t) = \sum_{n=1}^N r_n^{st} \left[\omega_n^2 D_n(t) \right] \quad (3.23)$$

Equation (3.23) can further be expressed as

$$r_n(t) = r^{st} \bar{r}_n [\omega_n^2 D_n(t)] \quad (3.24)$$

where

$$\bar{r}_n = \frac{r_n^{st}}{r^{st}} \quad (3.25)$$

is referred to as the n -th modal contribution factor.

Modal Analysis

For a SDOF-system with cosine loading; $m\ddot{u} + c\dot{u} + ku = F_0 \cos(\omega t)$, basic vibration theory gives the following expression for the harmonic response:

$$\bar{u} = \frac{1}{\underbrace{[(1 - \beta^2)^2 + (2\xi\beta)^2]^{1/2}}_D} \left(\frac{F_0}{k} \right) \quad \text{where} \quad \theta = \arctan \frac{2\xi\beta}{1 - \beta^2} \quad (3.26)$$

$$u = \bar{u} \cos(\omega t - \theta) \quad \beta = \frac{\omega}{\omega_n} \quad \omega_n = \sqrt{k/m}$$

It is seen that the harmonic response amplitude \bar{u} is proportional to the static displacement F_0/k , modified by a *dynamic magnification factor* D that depends on β and ξ . The same equations are valid for the uncoupled modal equations for a MDOF-system subjected to sinusoidal loading; $\tilde{m}_i \ddot{\eta}_i + \tilde{c}_i \dot{\eta}_i + \tilde{k}_i \eta_i = \tilde{R}_i^{ext}$. The MDOF-system is solved for its natural frequencies ω_i and the corresponding eigenmodes φ_i by solving the eigenvalue problem $(\mathbf{k} - \omega_{n,i} \mathbf{m}) \varphi_i = \mathbf{0}$.

The Direct Method

The *direct* method uses numerical integration to solve the equation of motion directly with respect to \mathbf{u} .

$$\mathbf{M}\ddot{\mathbf{u}} + \mathbf{C}\dot{\mathbf{u}} + \mathbf{K}\mathbf{u} = \mathbf{P}(t) \quad (3.27)$$

A solution algorithm is the Newmark integration method given in appendix B.1.

3.2.2 Response Spectrum Methods

A plot of the peak value of a response quantity as a function of the natural vibration period of a SDOF-system is referred to as a *response spectrum*. Before proceeding to the response spectrum method, an introduction related to the origin of the *pseudo*-quantities is given to better understand how it differs from the real quantities.

Concept of equivalent static force

One important task in earthquake engineering is to estimate the internal forces as base shear and moments. This can be done by the concept of *equivalent static force*, which uses the lateral stiffness k of the structure found by for example static condensation.

$$f_S(t) = ku(t) \quad (3.28)$$

f_S can be interpreted as the static external force that will produce the same deformation u as a dynamic system including mass and damping. Using the relation $k = m\omega_n^2$ gives

$$f_S(t) = m\omega_n^2 u(t) = mA(t) \quad (3.29)$$

where

$$A(t) = \omega_n^2 u(t) \quad (3.30)$$

is the *pseudo-acceleration* of the SDOF-system. The term *pseudo* is used to separate this quantity from the *real* acceleration $\ddot{u}(t)$. Once the deformation response $u(t)$ is determined, the pseudo-acceleration can easily be determined and the internal forces as base shear $V_b(t)$ and base moment $M_b(t)$ then reads

$$V_b(t) = f_s \quad M_b(t) = h f_s \quad (3.31)$$

Deformation, pseudo-Velocity and pseudo-Acceleration Response Spectra

The deformation response spectra plots the peak value $u_0 = D$ of the deformation history for a range of SDOF-systems with varying natural periods T_n . The pseudo-acceleration and pseudo-velocity response spectra are related to the deformation response spectra as

$$A_n = \omega_n^2 D \quad V_n = \omega_n D \quad (3.32)$$

where A_n and V_n are the peak value of $A(t)$ and $V(t)$ for the n -th period correspondingly. The pseudo-acceleration $A(T_n)$ for a SDOF is related to the peak value of the base shear, whereas the pseudo-velocity $V(T_n)$ for a SDOF is related to the peak value of the systems strain energy E_S .

$$V = \omega_n D = \frac{2\pi}{T_n} D \quad (3.33)$$

$$E_{S0} = \frac{k u_0^2}{2} = \frac{k D^2}{2} = \frac{k \frac{V^2}{\omega_n^2}}{2} = \frac{m V^2}{2} \quad (3.34)$$

Thus RSA-analysis avoid the dynamic analysis of SDOF-systems since this is already done to establish the response spectras. The spectras can be used to *estimate* the peak response of MDOF-systems as the method is not exact for such systems, but accurate enough.

3.3 Damping

The process by which vibration steadily diminishes in amplitude is called *damping*. Energy dissipation sources are for example friction at steel connections, opening and closing of microcracks in concrete and friction between elements. In models, damping is most commonly

represented by a viscous dashpot because it is mathematically simplest.

The damping matrix must be completely defined if classical modal analysis cannot be used. This is the case for non-linear systems and for systems with non-classical damping.

Classical damping is an appropriate idealization if similar damping mechanisms are distributed throughout the structure, for example a multistory building with similar structural system and structural materials over its height.

Non-classical damping applies for systems that consist of two or more parts with significant different levels of damping, for example a soil-structure system. For such cases, the damping matrix is constructed by assembling the damping matrices for the two substructures; the soil and the structure.

The damping matrix for a structure should be determined from its modal damping ratios, which account for all energy-dissipating mechanisms. The Rayleigh Ritz methodology is commonly used to construct a classical damping matrix.

3.3.1 Rayleigh damping

Rayleigh damping is a classical damping modelling method that combines a mass-proportional and a stiffness-proportional damping matrix, hence

$$\mathbf{c} = a_0 \mathbf{m} + a_1 \mathbf{k} \quad (3.35)$$

The computational steps in establishing the Rayleigh coefficients as a function of modal damping ξ_n is shown in equation (3.36) for both the mass-proportional term and the stiffness-proportional term. The transformation from matrix \mathbf{c} to modal coordinates C_n is valid because the mass \mathbf{m} and stiffness \mathbf{k} both exhibit modal orthogonality properties.

$$\begin{aligned}
\mathbf{c} &= a_0 \mathbf{m} & \mathbf{c} &= a_1 \mathbf{k} \\
C_n &= a_0 M_n & C_n &= a_1 K_n = a_1 \omega_n^2 M_n \\
\xi_n &= \frac{C_n}{2M_n \omega_n} = \frac{a_0}{2\omega_n} & \xi_n &= \frac{C_n}{2M_n \omega_n} = \frac{a_1}{2} \omega_n \\
a_0 &= 2\xi_n \omega_n & a_1 &= \frac{2\xi_n}{\omega_n}
\end{aligned} \tag{3.36}$$

Equation (3.36) shows that the modal damping ratio ξ_n strongly depend on the natural frequency ω_n considered. This is not consistent with experimental data which indicates roughly the same damping ratios for several vibration modes of a structure. The damping ratio of the n th mode of a Rayleigh damped system is then

$$\xi_n = \frac{a_0}{2\omega_n} + \frac{a_1}{2} \omega_n \tag{3.37}$$

The damping coefficients a_0 and a_1 is determined by assigning specified modal damping ratios ξ_i and ξ_j to the i -th and j -th mode. This results in the algebraic system in equation, which needs to be solved for a_0 and a_1 .

$$\frac{1}{2} \begin{bmatrix} \frac{1}{\omega_i} & \omega_i \\ \frac{1}{\omega_j} & \omega_j \end{bmatrix} \begin{Bmatrix} a_0 \\ a_1 \end{Bmatrix} = \begin{Bmatrix} \xi_i \\ \xi_j \end{Bmatrix} \tag{3.38}$$

If both modes are assumed to have the same damping ratio, i.e $\xi_i = \xi_j = \xi$, then the following expressions for a_0 and a_1 is obtained

$$a_0 = \xi \frac{2\omega_i \omega_j}{\omega_i + \omega_j} \quad a_1 = \xi \frac{2}{\omega_i + \omega_j} \tag{3.39}$$

Figure 3.3 shows the variation of the modal damping with frequency f .

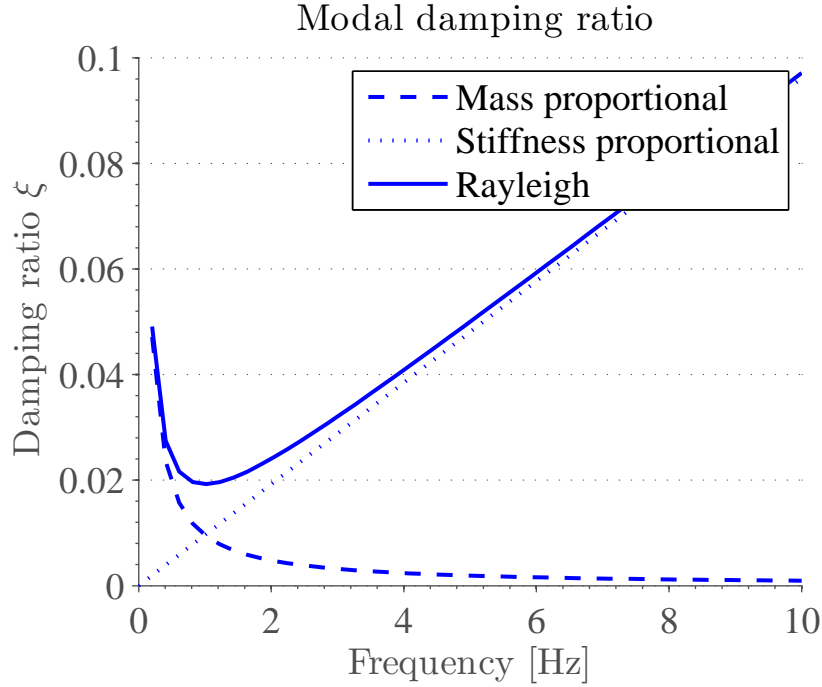


Figure 3.3: Variation of modal damping ratio ξ with frequency.

3.4 Transfer function of linear elastic soil with harmonic ground excitation

The derivation of the response and amplification function R_d of a uniform soil over rigid bedrock is presented in this section and follows the steps of Kramer [20].

3.4.1 Uniform Soil without damping

The partial differential equation of the soil is obtained by equilibrium of an infinitesimal element as

$$\begin{aligned}
 \sum F_x &= 0 && \text{Introduce} \\
 \Rightarrow \frac{\partial \tau}{\partial z} dz dA - \rho dA \ddot{u}(z, t) dz &= 0 && \tau = G\gamma = G \frac{\partial u(z, t)}{\partial z} \\
 \frac{\partial \tau}{\partial z} - \rho \ddot{u}(z, t) &= 0 && G \frac{\partial^2 u(z, t)}{\partial z^2} - \rho \ddot{u}(z, t) = 0
 \end{aligned} \tag{3.40}$$

The solution of this partial differential equation is obtained by assuming a harmonic displacement with time in each point of the soil, hence

$$u(z, t) = \bar{u}(z) \cos \omega t \quad \Rightarrow \quad \ddot{u}(z, t) = -\bar{u}(z) \omega^2 \cos \omega t \quad (3.41)$$

Insert these expressions into the partial differential equation to obtain the following general solution

$$\begin{aligned} G \frac{\partial^2 \bar{u}(z)}{\partial z^2} \cos \omega t + \rho \bar{u}(z) \omega^2 \cos \omega t &= 0 & \frac{\partial^2}{\partial z^2} \bar{u}(z) + \left(\frac{\omega}{V_s} \right)^2 \bar{u}(z) &= 0 \\ \frac{\partial^2}{\partial z^2} \bar{u}(z) + \frac{\rho}{G} \bar{u}(z) \omega^2 &= 0 & \text{This diff. eq. has the general sol.} & \\ \text{Insert for } V_s^2 = \frac{G}{\rho} \text{ and rewrite as} & & \bar{u}(z) &= A \cos \left(\frac{\omega}{V_s} z \right) + B \sin \left(\frac{\omega}{V_s} z \right) \end{aligned} \quad (3.42)$$

The two boundary conditions are 1. no shear forces at $z = H$ and 2. the displacement amplitude at the bedrock is identical to the ground displacement amplitude u_0 .

$$\text{at } z=0 \quad \Rightarrow \quad \bar{u} = u_0 \Rightarrow A = u_0 \quad (3.43a)$$

$$\text{at } z=H \quad \Rightarrow \quad \tau = G \frac{\partial u(z=H, t)}{\partial z} = 0 \quad (3.43b)$$

The boundary condition in equation 3.43b implies that the displacement amplitude term $\bar{u}(z)$ need to fulfill

$$\frac{\partial \bar{u}(z=H)}{\partial z} = 0 \quad (3.44)$$

$$\begin{aligned} \Rightarrow -A \frac{\omega}{V_s} \sin \left(\frac{\omega}{V_s} H \right) + B \frac{\omega}{V_s} \cos \left(\frac{\omega}{V_s} H \right) &= 0 \\ \Rightarrow B = A \tan \left(\frac{\omega}{V_s} H \right) = u_0 \tan \left(\frac{\omega}{V_s} H \right) \end{aligned} \quad (3.45)$$

Insert the expressions for the constants A and B into equations 3.42 to obtain the result for the

displacement amplitude $\bar{u}(z)$ in a linear elastic soil layer.

$$\bar{u}(z) = u_0 \cos\left(\frac{\omega}{V_s} z\right) + u_0 \tan\left(\frac{\omega}{V_s} H\right) \sin\left(\frac{\omega}{V_s} H\right) \quad (3.46)$$

To find the natural frequencies ω_n and the corresponding eigenmodes φ of the soil, the response $u(z, t)$ of the soil need to be analyzed when there are no excitation of the ground, i.e $u_0 = 0$ and also $A = 0$. Solving equation 3.44 when $A = 0$ for the natural frequencies of the soil gives the following result:

$$\begin{aligned} \frac{\partial \bar{u}(z=H)}{\partial z} &= 0 & \omega_n &= \frac{2n-1}{2} \frac{\pi V_s}{H} \\ \Rightarrow B \frac{\omega_n}{V_s} \cos\left(\frac{\omega_n}{V_s} z = H\right) &= 0 & \text{and the mode shapes} & \\ \text{Non-trivial sol. is obtained by} & & \bar{u}(z, \omega_n) &= B \sin\left(\frac{\omega_n}{V_s} z\right) \\ \left(\frac{\omega_n}{V_s} H\right) &= \frac{\pi}{2}(2n-1) \text{ for } n=1,2,\dots & &= B \sin\left(\frac{2n-1}{2} \frac{\pi z}{H}\right) \end{aligned} \quad (3.47)$$

The three first modeshapes of a linear elastic soil is plotted in figure 3.4. The expression for the three first modeshapes and the corresponding natural frequencies are

$$\omega_1 = \frac{\pi V_s}{2H} \Rightarrow \varphi_1 = \sin\left(\frac{\pi z}{2H}\right) \quad (3.48)$$

$$\omega_2 = \frac{3\pi V_s}{2H} \Rightarrow \varphi_2 = \sin\left(\frac{3\pi z}{2H}\right) \quad (3.49)$$

$$\omega_3 = \frac{5\pi V_s}{2H} \Rightarrow \varphi_3 = \sin\left(\frac{5\pi z}{2H}\right) \quad (3.50)$$

The theoretical amplification in displacement between a point at the bedrock and a point at the soil surface without damping in the soil is given as

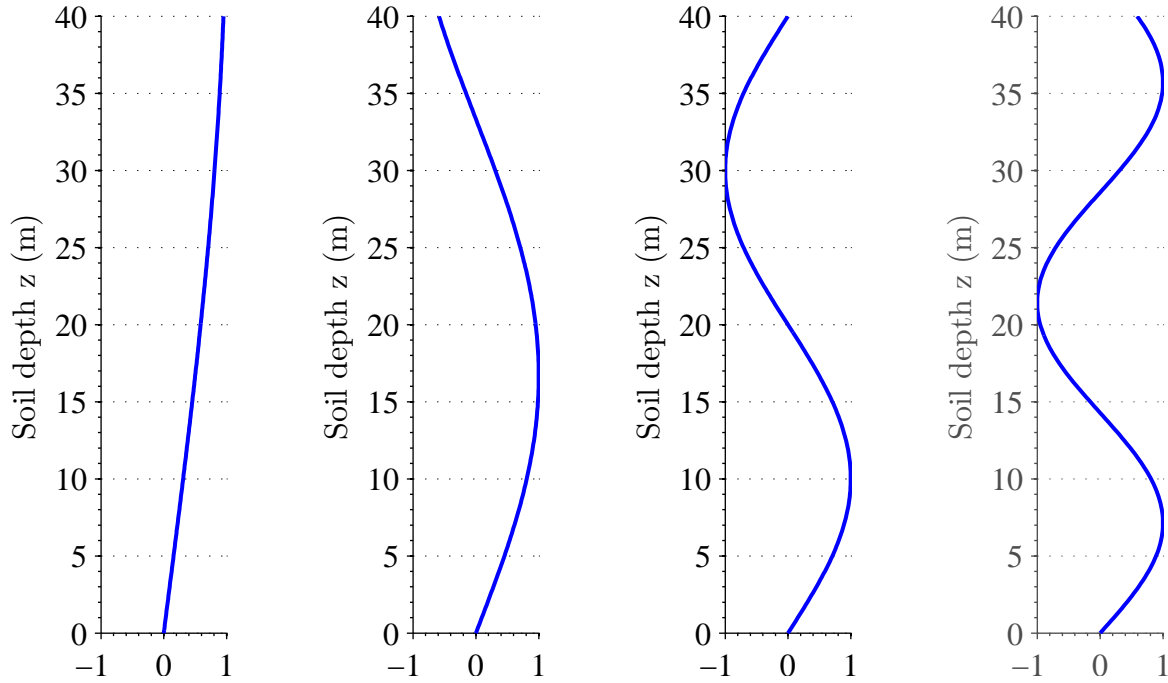


Figure 3.4: Plot of the five first modeshapes of a uniform linear elastic soil

$$\begin{aligned}
 R_d(\omega) &= \frac{|u|_{z=H}}{|u|_{z=0}} = \frac{u_0 \cos\left(\frac{\omega}{V_s} z\right) + u_0 \tan\left(\frac{\omega}{V_s} H\right) \sin\left(\frac{\omega}{V_s} H\right)}{u_0} \\
 &= \cos\left(\frac{\omega}{V_s} H\right) + \frac{\sin^2\left(\frac{\omega}{V_s} H\right)}{\cos\left(\frac{\omega}{V_s} H\right)} = \frac{1}{\left|\cos\left(\frac{\omega H}{v_s}\right)\right|}
 \end{aligned} \tag{3.51}$$

3.4.2 Uniform Soil with damping

Damping is present in all materials and needs to be included to obtain more realistic responses.

The differential equation of an infinitesimal soil element with damping is

$$G \frac{\partial^2 u(z, t)}{\partial z^2} + \eta \frac{\partial^3 u}{\partial z^2 \partial t} = \rho \ddot{u}(z, t) \tag{3.52}$$

where the only additional term compared to equation (3.42) is the frequency independent damping term $\eta \frac{\partial^3 u}{\partial z^2 \partial t}$. The solution of this wave equation is on the form

$$u(z, t) = Ae^{i(\omega t + k^* H)} + Be^{i(\omega t - k^* z)} \quad (3.53)$$

where k^* is the complex wave number. Further details of the derivation can be found in Kramer [20]. The final expression for the amplification factor $|H(\omega)|$ is

$$|H(\omega)| \approx \frac{1}{\sqrt{\cos^2(kH) + (\xi kH)^2}} = \frac{1}{\sqrt{\cos^2(\omega H/V_s) + [\xi(\omega H/V_s)]^2}} \quad (3.54)$$

The amplification for different soil materials is given in figure 3.5.

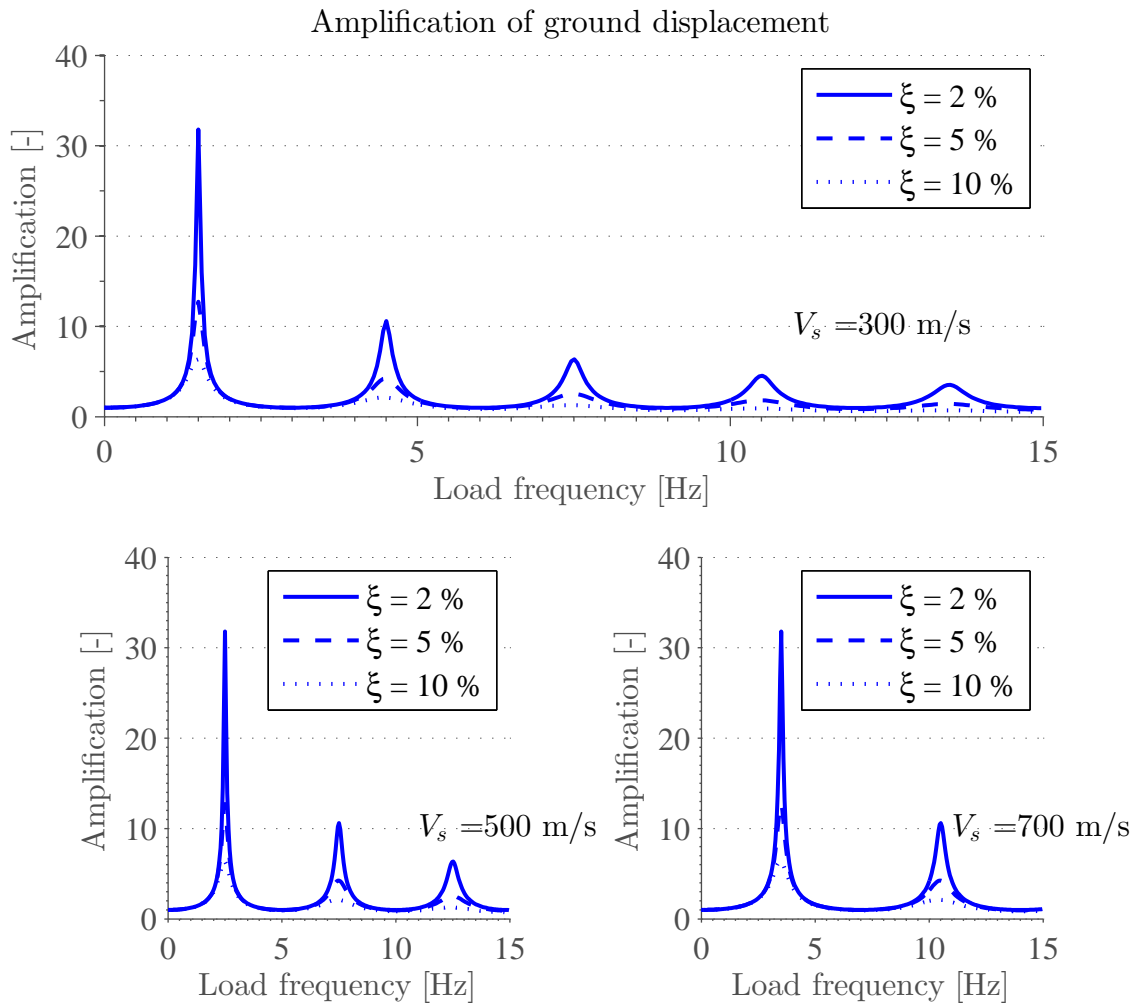


Figure 3.5: Theoretical amplification factor for uniform linear elastic soil for different V_s and damping ratios ξ

3.5 Soil-Structure Interaction

Soil-structure interaction (SSI) refers to the process in which the structure influences the response of the soil and vice versa. Ground motions not influenced by the presence of structures are referred to as *free-field motions*.

The two sources of soil-structure interaction are 1) the inability of the foundation to conform to the free-field motion of the soil and 2) the influence of the dynamic response from the structure-foundation system to the surrounding soil. The first cause is referred to as *kinematic interaction* and is illustrated in figure 3.6 for different foundation geometries.

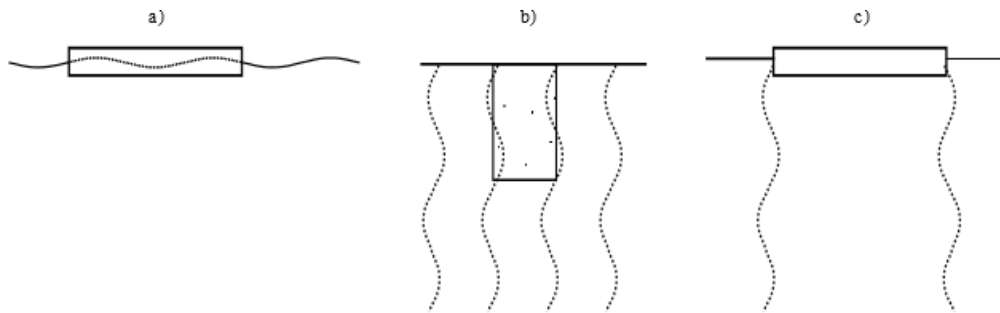


Figure 3.6: Kinematic interaction with free-field motion indicated by dashed lines

Figure *a)* shows a surface foundation subjected to vertical displacements due to wave travelling. The bending stiffness will prevent the foundation to entirely conform to the free-field motion indicated by the dashed lines. Figure *b)* shows an embedded foundation subjected to horizontal displacements where its rigidity prevents it from following the free-field motion. Figure *c)* shows that also the axial stiffness of a foundation can prevent immediately underlying soil to deform for a case with a incoherent (note the reversed wave) free-field motion.

Kinematic interaction is present whenever the *stiffness* of the foundation impedes development of the free-field motion. The relation between the wave length and the embedment depth is also important for the extent of rocking deformation in the structure. The first case in figure 3.7 will experience more rocking compared to the second case. The forces on the latter will to a greater extent outbalance each other and thus result in a smaller moment.

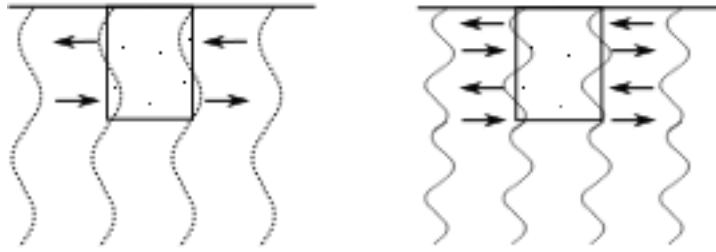


Figure 3.7: Excitation of rocking in embedded foundations by vertically propagating S-waves.

3.5.1 Equivalent System Frequency

An important effect of SSI is a reduction in the natural frequency of the soil-structure system compared to the corresponding fixed-base configuration. The derivation of the equivalent natural frequency for a SDOF-system is found in Kramer [20] and is repeated here as

$$\frac{1}{\omega_{eq}^2} = \frac{1}{\omega_0^2} + \frac{1}{\omega_h^2} + \frac{1}{\omega_r^2} \quad (3.55)$$

where ω_{eq} is the system equivalent natural frequency, ω_0 is the fixed-base natural frequency, ω_h is the swaying natural frequency of the foundation and ω_r is the rocking natural frequency of the foundation.

3.6 Three-Step-Method

The three-step method refers to a solution procedure where the kinematic and inertial interaction are separated. The theory presented originate from Kausel et al. [18].

3.6.1 The superposition theorem

The equations of motion for the soil/structure system are given by

$$\mathbf{M}\ddot{\mathbf{U}}^t + \mathbf{C}\dot{\mathbf{U}} + \mathbf{K}\mathbf{U} = \mathbf{0} \quad (3.56a)$$

$$\mathbf{M}\ddot{\mathbf{U}} + \mathbf{C}\dot{\mathbf{U}} + \mathbf{K}\mathbf{U} = -\mathbf{M}\ddot{\mathbf{U}}_g \quad (3.56b)$$

The equation system is equivalently described by a *kinematic* interaction and a *dynamic* interaction as

$$\text{Kinematic interaction: } \mathbf{M}_1 \ddot{\mathbf{U}}_1^t + \mathbf{C}\dot{\mathbf{U}}_1 + \mathbf{K}\mathbf{U}_1 = \mathbf{0} \quad (3.57a)$$

$$\text{Dynamic interaction: } \mathbf{M}\ddot{\mathbf{U}}_2 + \mathbf{C}\dot{\mathbf{U}}_2 + \mathbf{K}\mathbf{U}_2 = -\mathbf{M}_2 \ddot{\mathbf{U}}_1^t \quad (3.57b)$$

$$\text{Added: } \underbrace{\mathbf{M}_1 \ddot{\mathbf{U}}_1^t + \mathbf{M}_2 \ddot{\mathbf{U}}_1^t}_{\mathbf{M}\ddot{\mathbf{U}}_1^t = \mathbf{M}\ddot{\mathbf{U}}_1 + \mathbf{M}\ddot{\mathbf{U}}_g} + \mathbf{M}\ddot{\mathbf{U}}_2 + \underbrace{\mathbf{C}(\dot{\mathbf{U}}_1 + \dot{\mathbf{U}}_2)}_{\mathbf{C}\dot{\mathbf{U}}_2} + \underbrace{\mathbf{K}(\mathbf{U}_1 + \mathbf{U}_2)}_{\mathbf{K}\mathbf{U}_2} = \mathbf{0} \quad (3.57c)$$

where variables with subindex 1 (i.e. $\ddot{\mathbf{U}}_1, \dot{\mathbf{U}}_1, \mathbf{U}_1$) refers to the solution of a system with a *massless* structure and foundation, whereas subindex 2 (i.e. $\ddot{\mathbf{U}}_2, \dot{\mathbf{U}}_2, \mathbf{U}_2$) refers to the solution where the system is subjected to inertia forces originating from the kinematic step. When the two equation systems are added the original equations are obtained. The equations in 3.57 are visually illustrated in figure 3.8.

The *kinematic interaction* step represent the solution of the system with a massless structure and foundation subjected to a seismic ground motion $\ddot{\mathbf{U}}_g$. Thus, the inertia from the structure is excluded in this step. The total response in the kinematic interaction step is persued to the *dynamic interaction* step.

For the particular case where the combination foundation/structure is very rigid, the structure will move as a *rigid body*. The rigid body motion is then fully described by the vertical, torsional,

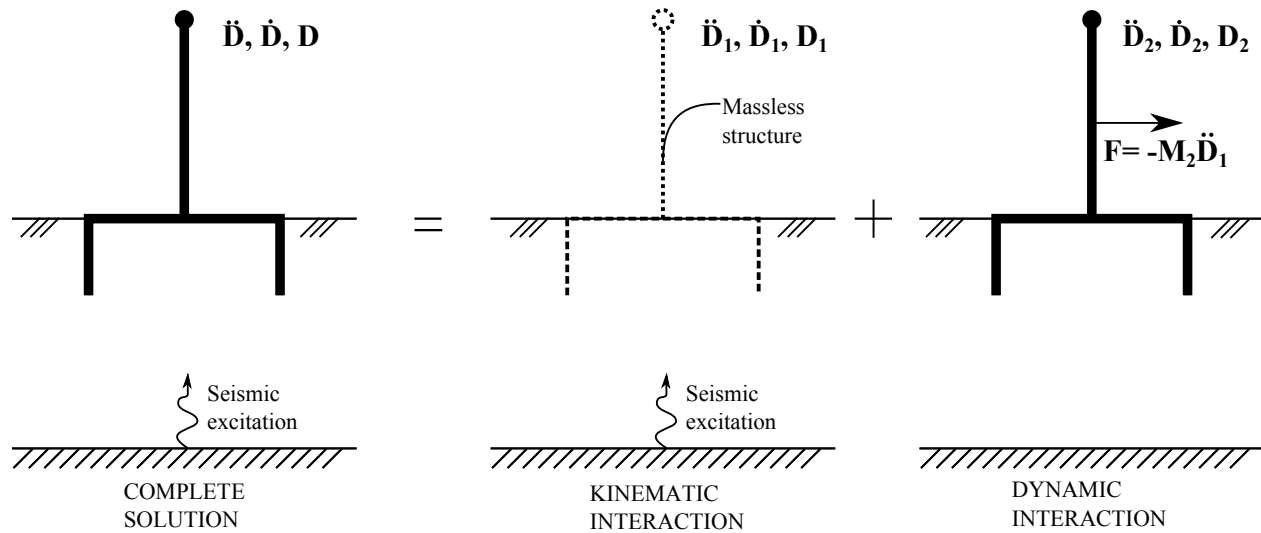


Figure 3.8: Superposition theorem

rocking and swaying stiffness functions at the foundation level.

3.6.2 Method

The three steps needed to obtain a simplified spring solution are illustrated in figure 3.9. The method consists of a kinematic step, an impedance step and a combination step.

1. **Kinematic interaction:** Kinematic interaction occurs whenever the stiffness of the foundation system impedes development of free-field motions. Determination of the input motion of the massless rigid foundation under seismic base loading; i.e solution to the kinematic interaction equations. For an *embedded* foundation it will yield, in general, both translations and rotations.
2. **Subgrade impedances:** Determination of soil stiffnesses as equivalent static or frequency dependent springs for the relevant degrees of freedom.
3. **Combination:** Computation of the response of the structure supported with springs and dashpots and subjected to the input motion calculated in step 1).

Note that the three-step-method is only a faster method compared to a full numerical model if reasonable approximations for the kinematic base inputs and foundation stiffnesses exists. If not, a numerical simulation of the seismic soil response with a massless foundation must be car-

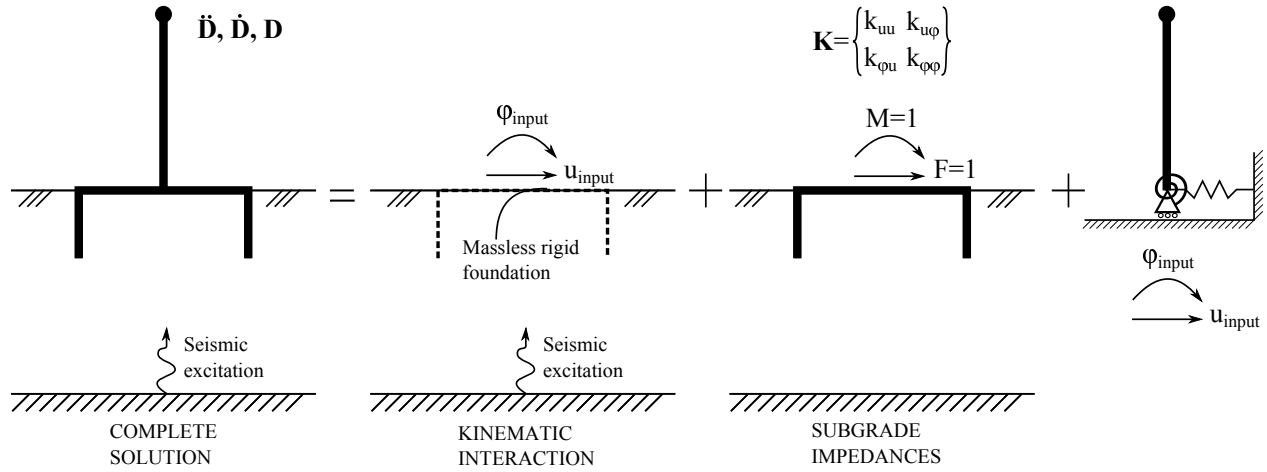


Figure 3.9: The three-step method

ried out. The three-step-method is a flexible method as it separates the base input motion from the inertial responses. This make the method highly suitable for parametric studies without the need to rerun entire analysis.

Note, that the superposition principle is only valid for linear systems. While the modulus and the damping of the soil are strain dependent, studies have shown that most of the non-linearity occurs as a result of the earthquake motion, and not as a results of soil-structure interaction [18].

3.6.3 Dynamic Impedances

The dynamic impedances represent the frequency dependent stiffness and damping characteristics in soil-foundation interaction. The importance of the frequency dependent properties varies with the foundation type considered and the soil material properties. Harte [13] suggest that the frequency variation can be important for soft soils materials.

For each harmonic excitation with frequency ω , the *dynamic impedance* (or the dynamic stiffness) is defined as the ratio between the steady-state force (or moment) and the resulting displacement (or rotation). For a SDOF-system, the dynamic impedance reads

$$K^* = \frac{P(t)}{u(t)} \tag{3.58}$$

where k^* consists of an imaginary part and a real part

$$K^*(\omega) = K_1(\omega) + iK_2(\omega) \quad (3.59)$$

where the imaginary component reflects the frequency dependent radiation damping and material damping of the system [9]. The derivation of the dynamic impedance for a single oscillator is given in section B.3 in the appendix to introduce the concept.

Chapter 4

State of the Art

A brief summary of the most relevant research related to wind turbines, bucket foundations and numerical methods is presented in this chapter. A more comprehensive description of two full-scale shake table experiments of a 65 kW wind turbine is given.

4.1 Wind Turbines, Skirted Foundations and SSI

The scientific development and basic theory for simplified methods in soil dynamics is summarized by Dobry [5]. Stiffness and damping formulas for *surface foundations* were first presented and validated in 1986 by Dobry and Gazetas for all six degrees of freedom [6] [7]. The formulas were further developed to include embedded foundations of arbitrary shape. In 1991 Gazetas presented formulas and charts for dynamic stiffnesses and damping coefficients in a homogeneous halfspace [10]. The formulas proved to accurately represent numerically obtained natural frequencies, but overestimates the radiation damping in swaying [11].

Kausel et al. [18] made the following conclusions for use of the spring method for embedded foundations:

- It is more important to correctly represent the *static* stiffnesses of embedded foundations than their complete frequency variation.

- The increase in stiffness due to embedment is very sensitive to the properties of the lateral soil, which may be disturbed, and to the degree of adhesion of the lateral walls to the soil.

Gazetas [9] presents simple formulas and dimensionless graphs for the dynamic impedance functions of circular, strip, rectangular and arbitrary-plan-shape foundations. The formulas are later used to estimate the stiffness of the bucket foundation.

Ishihara [17] made the following observations with respect to seismic simulation of wind turbines:

- The contribution of higher modes towards the structural response is small for middle-sized wind turbines. However it becomes important for large wind turbines resulting in overestimation of the base shear and base moment when WEE model, i.e rotor-system modeled as a lumped top mass, is used.
- The present acceleration response spectrum used in building codes in Japan does not capture the characteristics of the acceleration response spectrum obtained for structures with very low damping such as wind turbines.

Kourkoulis et al. [19] made the following observations concerning offshore bucket foundations subjected to lateral monotonic, cyclic and earthquake loading:

- In the case of monotonic and slow cyclic loading it is shown that imperfect interface bonding could reduce the moment capacity and may lead to foundation detachment or even uplifting in the case of shallowly embedded caissons.
- Increasing the bucket diameter while maintaining the embedment is more efficient in terms of material than increasing the skirt length while keeping the diameter constant.
- For soil/foundation/wind turbine interacting systems subjected to simultaneous environmental and seismic loads, the system kinematics may prove crucial to the response of large wind turbines. The accumulation of foundation rotation could lead to the turbine reaching serviceability limits early during its operation.

A recently study by Torabi [27] demonstrates that rigid slender structures are highly susceptible to the SSI effects including alternation of natural frequency, foundation rocking and excessive

base shear demand. The relative stiffness between the structure and foundation and their aspect ratio were found to be crucial parameters controlling the inertial soil-structure interaction in flexible-base structures.

4.2 Full-scale Shake Table Test of a Nordtank Wind Turbine

In 2004 and 2010 researches from University of California San Diego performed a full-scale shake table test of a 65 kW wind turbine. The aim was to assess natural frequencies, mode shapes and equivalent viscous damping and compare the result from numerical simulations with experimental results. A comprehensive description of the experiments are given, since the results are used to validate a FE-model of a wind turbine in chapter 6.

The wind turbine was excited at its fixed-base configuration with the East-West component of the strike-slip Landers earthquake from 1992, recorded at Desert Hot Spring station. The earthquake has a peak ground acceleration of $PGA = 0.15g$ and a moment magnitude of $M_w = 7.3$ [8]. The seismic response was measured on four points along the tower as seen in figure 4.2a.

From 2004

Figure 4.1 shows the wind turbine installed at the shake-table in its side-side direction with one blade pointing downwards. Two models were developed in OpenSees; an open-source system for earthquake engineering simulations. The first model consists of several beam elements representing the tower, whereas a lumped top mass accounts for the nacelle and blades. Additional beam elements were included in the second model to explicitly represent the geometric configuration of the nacelle and the rotor. A summary of the experimental and numerical eigenfrequencies of the parked wind turbine is given in table 4.1.

The following observations and conclusions were made:

- The simplified beam-column models estimated the fundamental modes accurately. The fundamental frequency estimation formula developed by the International Building Code

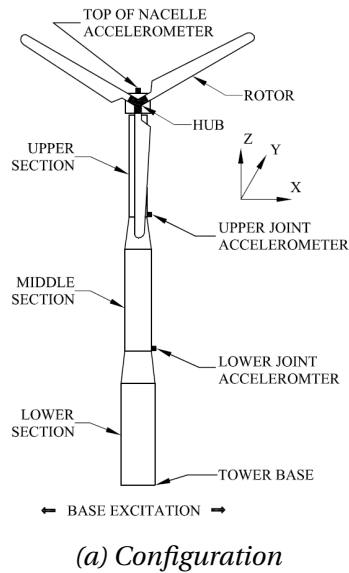


Figure 4.1: Shake-table test from 2004

(IBC) closely matches the experimental value when using the hub height and $2/3$ of the blade length as input.

- First mode damping was estimated below 1% for the parked wind turbine. Depending on the underlying ground properties, SSI may increase overall damping due to energy radiation.
- For small utility scale turbines, a first mode response was shown to provide a reasonable approximation. Hence, the response spectrum approach may provide a convenient approach for estimating the seismically induced peak shear force and moment.
- For larger modern wind turbines, higher modes may play an more important role in seismic response. More credible models needs to be developed for such cases.

From 2010

In 2010 an *extended* full-scale shake table test of the Nordtank wind turbine was carried out at the University of California San Diego. This time the response of the wind turbine was examined in two states; while the wind turbine rotor was still (parked state) and while spinning (operational state). The wind turbine was also shaken in both the fore-aft direction and the side-side

direction for different earthquake loads. The orientation of the blades was also different from the previous test; now one blade was horizontally oriented.

A FE-model of the wind turbine was developed in FAST, which uses modal damping. Several adjustments were made to match the experimental mode shapes.



(a) Fore-aft configuration



(b) Side-side configuration

Figure 4.2: Shake-table test from 2010

The following observations and conclusions were made:

- Shaking imparted in the fore-aft direction while spinning is the only observed situation where operational effects appear significant, with reduction up to 33% in seismic bending moment demand near the tower base [24].
- In the fore-aft direction the equivalent viscous damping was approximately twice as high in the operational state compared to the parked state (2.0% vs 1.0%). The higher damping is due to additional aerodynamic effects caused by blade flap vibrations. Gyroscopic forces from rotation of the rotor may also contribute to changes in the dynamics properties while the turbine is operating [23].
- When a wind turbine is subjected to both wind and seismic load it is important to consider the orientation of shaking and the aerodynamic damping.

Table 4.1: Summary of experimentally and numerically obtained eigenfrequencies of the parked 65-kW wind turbine. The numerical result represent model 2.

f_n	2004				2010			
	Shake table		FE-Model ¹⁾		Shake table		FE-Model ²⁾	
	Type	f [Hz]	Type	f [Hz]	Type	f [Hz]	Type	f [Hz]
1	S-S	1.70	S-S	1.68	F-A	1.70	F-A	1.70
2	Coupled	11.7-12.3	F-A	1.7	S-S	1.71	S-S	1.71
3	-	-	T	9.2	Coupled	11.3	-	-
4	-	-	F-A	9.7	F-A	11.9	F-A	11.9
5	-	-	S-S	12.1	S-S	12.4	S-S	12.4

S-S: Side-side, F-A: Fore-aft and T: Torsional

1) FE-program: OpenSees (Rayleigh damping)

2) FE-program: FAST (modal damping)

Chapter 5

Numerical Model of Soil

It is widely recognized that site effects can significantly change the nature of the ground motion. The 1985 Mexico City and 1989 Loma Prieta earthquakes revealed that soft soil deposits can significantly amplify the ground motion which in turn affects the response of the structures [27] on the surface. Therefore, it is important that the numerical model is able to accurately describe the correct soil amplification. To ensure correct behaviour of the modeled soil, this chapter validates the numerical soil algorithm with respect to the theoretical transfer function derived in chapter 3.4.

5.1 Model Description

When a soil in free-field conditions is excited by a horizontal ground motion, the soil behaves like a shear-beam where the soil particles in the same horizontal plane move together. The soil will not behave like water subjected to the same seismic loading, because it is not possible for the soil to slide on the rock surface. In comparison, the water is able to move up and down relative to the surface because of the low friction coefficient of water. This type of sliding is highly restricted in a soil, which causes pure horizontal motion. This difference between water and soil materials is illustrated in figure 5.1.

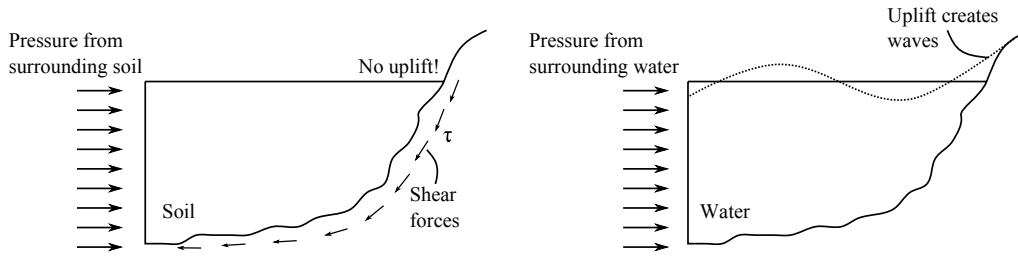


Figure 5.1: Behaviour of soil and water near the boundaries subjected to seismic excitation.

Geometry & Material Properties

The soil slice in figure 5.2b has a length of $L_x = 100m$ in the x-direction, $L_y = 1m$ in the y-direction and a depth of $H = 50m$. The relation between the shear modulus G , poisson's ratio ν and shear wave velocity V_s is

$$V_s = \sqrt{\frac{G}{\rho}} \quad \text{and} \quad G = \frac{E}{2(1 + \nu)} \quad (5.1)$$

The soil material properties is given in table 5.1. The first and fifth theoretical mode shape are assigned a damping coefficient of $\xi = 5\%$ which corresponds to the Rayleigh coefficients $a_0 = 0.8511$ and $a_1 = 0.0011$.

Table 5.1: Material properties of modelled soil

Young's mod. E [MPa]	Poisson's ratio ν [-]	Shear mod. G [Mpa]	Density ρ [kg/m^3]	Shear wave V_s [m/s]
540	0.50	180	2 000	300

Boundary Conditions & Constraints

The soil slice is excited in the longitudinal x-direction. The shear-beam lateral boundary condition is applied to the two vertical end planes by a *tie* constraint. Further, the bottom nodes are pinned to the ground and free to move in the excitation direction.

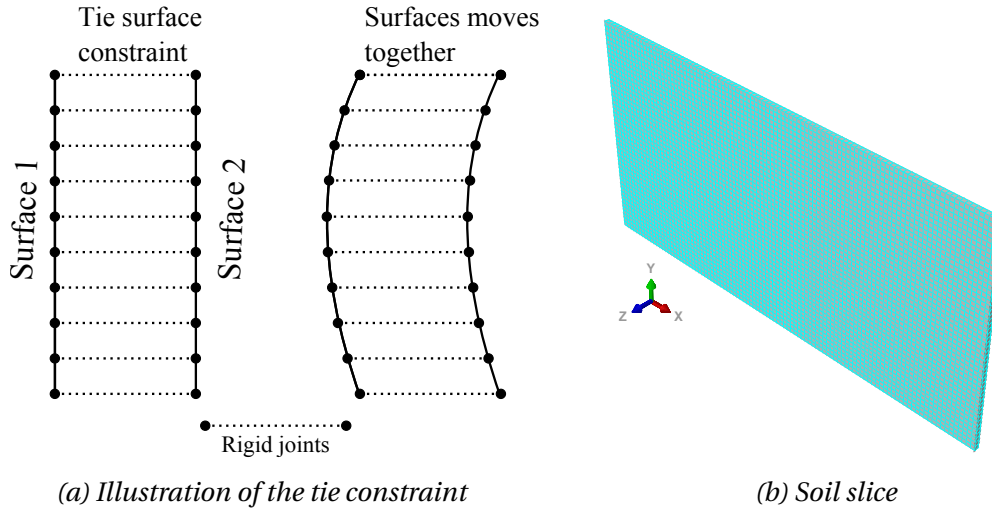


Figure 5.2: Applied tie constraints in the soil model

Elements & Mesh

The element size must be able to represent a propagating shear wave in the soil. A mesh with approximately 10 elements over the wave length λ is experienced to be adequately. The following relations are used to determine the element size;

$$\lambda = \frac{V_s}{f} \quad \text{and} \quad L_e = \frac{\lambda}{10} \quad (5.2)$$

where f is the highest harmonic load frequency of interest and L_e is the minimum element size for linear elements. For a maximum frequency in the considered earthquake of $f_{max} = 15Hz$ and a minimum shear wave velocity in the soil of $V_{s,min} = 300m/s$ the smallest wave length and element size required is then

$$\lambda_{min} = \frac{300 \frac{m}{s}}{15s^{-1}} = 20m \quad \text{and} \quad L_{e,max} = \frac{20m}{10} = 2m \quad (5.3)$$

The soil is validated for the three meshes shown in figure 5.3 which consists of *a*) a quadrilateral of linear order, *b*) a quadrilateral of second order and *c*) a tetrahedron on second order.

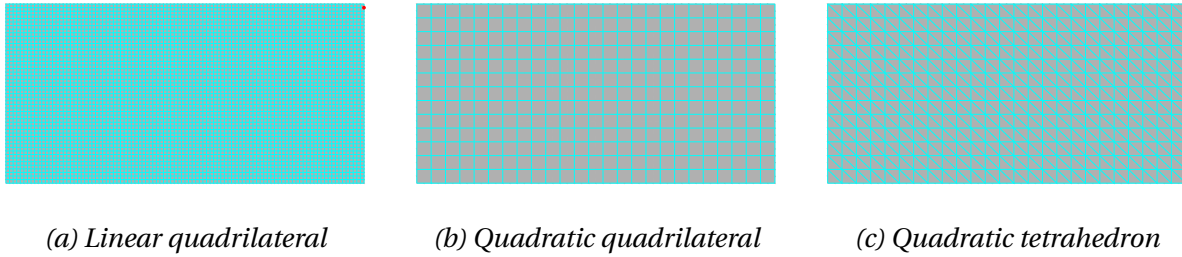


Figure 5.3: Different soil meshes.

5.1.1 Results

Accurate numerical results are obtained for both the natural frequencies and the amplification of the homogeneous soil for a range of harmonic base excitations. Table 5.2 shows that the five first modes shown in figure 5.4 are predicted by an error less than 0.4%. Identical results were obtained for both of the second order elements. Note that the size of the second order elements are four times larger than the linear elements, and still better results are obtained.

The ground amplification computation is done for three cases to control the agreement in the results; *a)* a soil-slice with only one element in the y -direction with a unit length, *b)* a soil-volume with ten elements in the y -direction and *c)* a time domain simulation. The two time domain simulations are given in figure 5.6. For an excitation frequency of $f = 2.00\text{Hz}$ it is shown that the maximum displacement occurs in the transient phase as shown in figure 5.6. However, the purple dots in figure 5.5 is taken as the maximum displacement in the steady-state phase of the time series plots.

Table 5.2: Natural frequencies of soil for elements C3D8R (linear), C3D20R (quadratic) and C3D10 (quadratic).

Mode	Theoretical [Hz]	Numerical [Hz]		Error	
		Linear ¹⁾	Quadratic ²⁾	Linear	Quadratic
1 st	1.5050	1.5050	1.5050	0.00 %	0.00%
2 nd	4.5150	4.5134	4.5151	0.04 %	0.00%
3 rd	7.5250	7.5174	7.5258	0.10 %	0.01%
4 th	10.535	10.514	10.539	0.20 %	0.04%
5 th	13.545	13.500	13.558	0.33 %	0.10%

1) Element size 1m; 2) Element size 4m

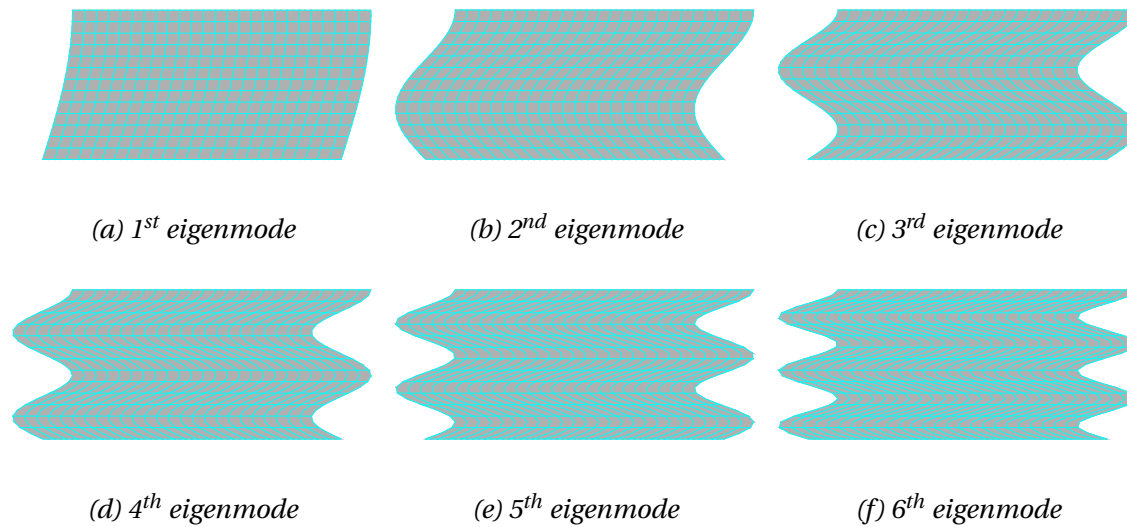


Figure 5.4: The six first eigenmodes of the homogenous linear-elastic soil model.

The result for the linear elements is shown in figure 5.5 together with the theoretical result. Since the damping coefficient ξ in the model depends on the excitation frequency due to applied Rayleigh damping, the damping in the theoretical result has been modified correspondingly. The mesh and the applied constraint is able to accurately represent the correct displacement amplification in all three cases. The same conclusion is also valid for the three element meshes. It is observed that the numerical result start to deviate from the theoretical solution for frequencies above approximately 12 Hz. An explanation to the deviation can be explained with respect to the chosen mesh size. Larger load frequencies require a smaller mesh size to obtain an adequate amount of elements per wave length.

The validation of the soil provided satisfactory results and the modelling techniques used can confidently be used in the fully integrated model.

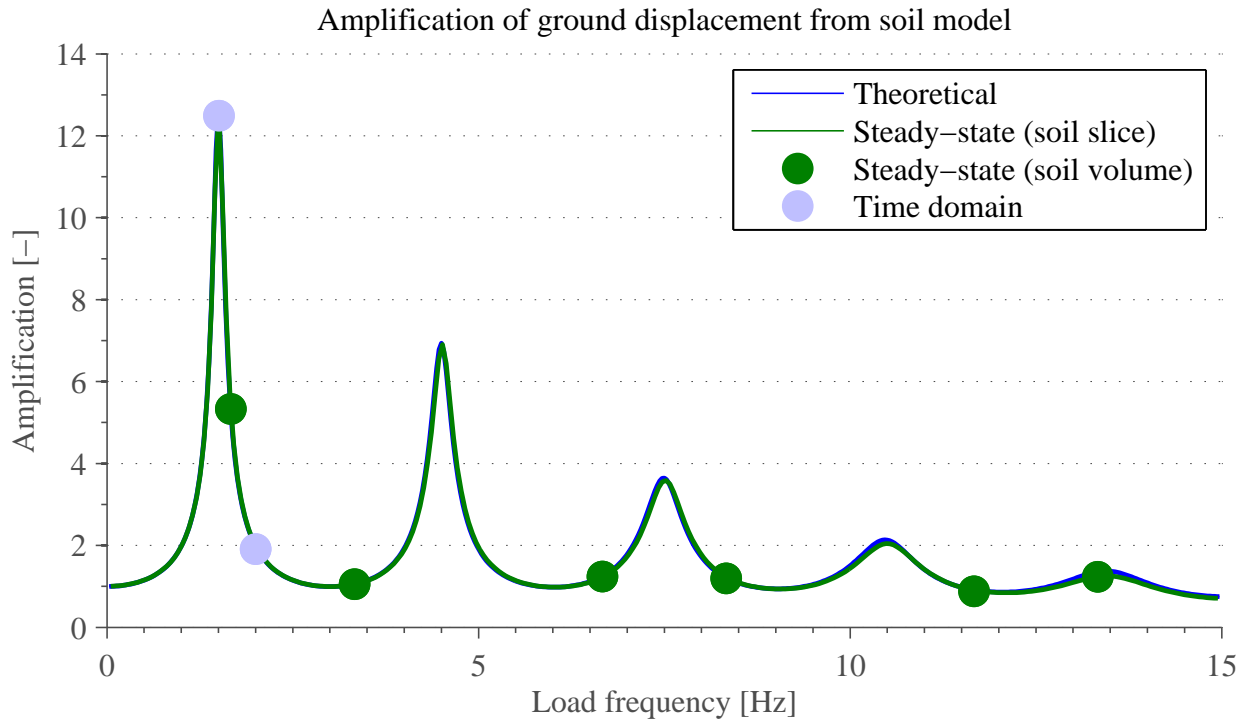


Figure 5.5: Amplification of soil with harmonic base excitation, 5 % Rayleigh damping, $V_s = 300$ m/s and linear elements. The purple dots indicates the maximum displacement from the steady-state phase from a time-domain simulation.

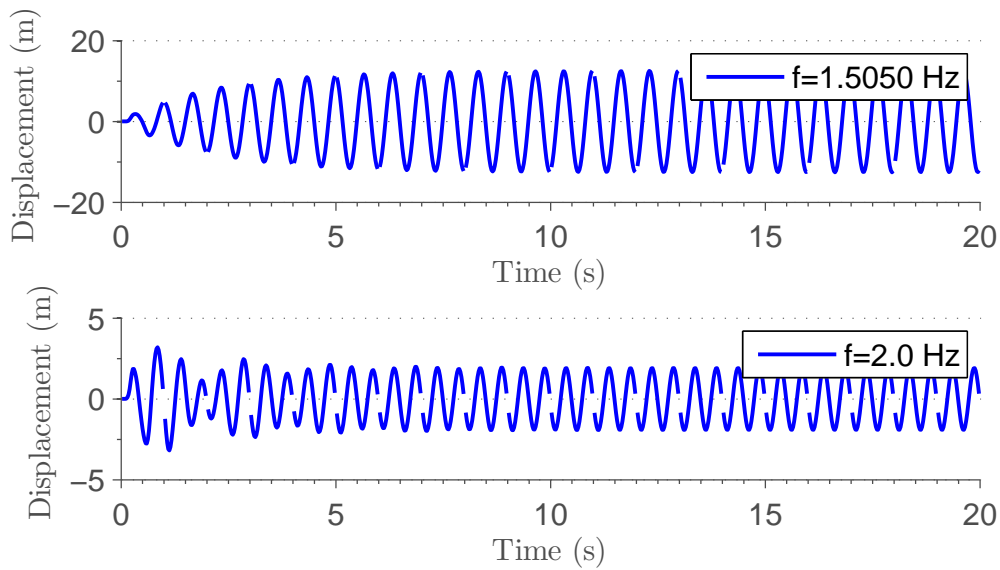


Figure 5.6: Time domain response of a soil with a base excitation with frequencies $f = 1.5050$ Hz (1^{st} natural frequency) and $f = 2.0$ Hz with 5 % damping.

Chapter 6

Validation of a Nordtank Wind Turbine

Model

In this section a FE-model of a *parked* 65-kW Nordtank wind turbine is presented and validated against experimental results from a full-scale shake table test performed at the university of California San Diego. The two models created are *a)* a model which explicitly models the blades and hub and *b)* a model with a lumped top mass which account for the mass of the blades and hub. The numerical algorithm in the most accurate model is transmitted to the four times higher Vestas model.

6.1 Experimental Results

A description of the experimental shake-table tests is given in section 4.2. The experiments provides useful information about natural frequencies, mode shapes and damping of the Nordtank 65-kW wind turbine for parked and operational conditons. The modal properties for the parked wind turbine is given in table 6.1 and shown in figure 6.1 and figure 6.2.

The bending mode in the fore-aft direction is the lowest mode, closely followed by the side-side direction. A coupled mode occurs at 11.3 Hz and the two second bending modes at 11.9 Hz and 12.4 Hz. Also a torsional mode around 9Hz was observed in addition to the modes shown. Note

that the modal values is from the shake table test from 2010 where one blade was horizontally orientated. Even if the blade orientation in the model differs from this, these values are chosen to comparison because the experiment from 2004 only studied the turbine properties in the side-side direction.

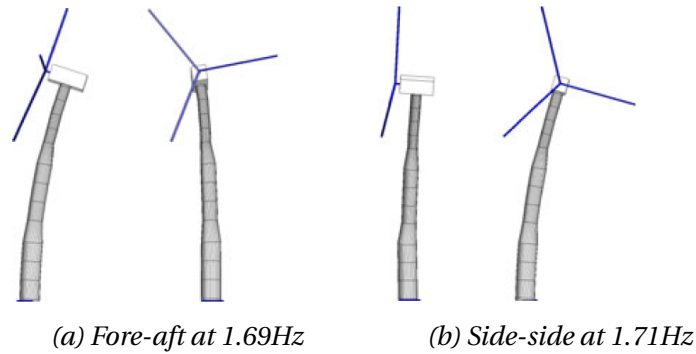


Figure 6.1: Observed 1st tower mode shapes [24]

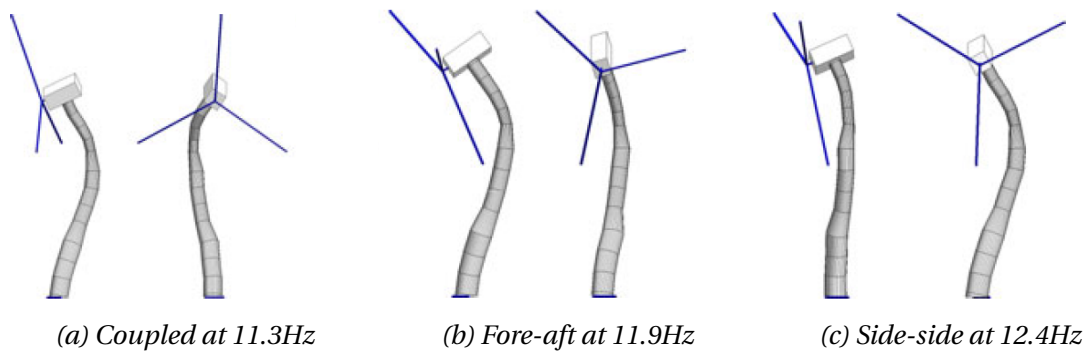


Figure 6.2: Observed 2nd tower mode shapes [24]

6.2 Model Description

This section presents the two established Nordtank wind turbine models. Model 1 explicit models the nacelle/rotor system and model 2 has a lumped top mass. The two models are shown in figure 6.3. Several simplifications and estimates are made due to insufficient available data concerning geometry, mass distribution and interior structural elements.

Table 6.1: Summary of the modal properties of the parked 65-kW wind turbine¹⁾ [24]

Number	Type	Frequency			Damping		
		Mean	Range	STD	Mean	Range	STD
1	FA	1.69	1.69-1.70	0.002	0.57	0.49-0.64	0.04
	SS	1.71	1.70-1.72	0.004	0.84	0.61-1.25	0.16
2	Coupled	11.3	11.2-11.4	0.054	1.5	0.9-1.9	0.27
	FA	11.9	11.8-11.9	0.041	1.6	1.4-2.0	0.21
	SS	12.4	12.3-12.6	0.065	1.9	1.5-2.7	0.29

Note: FA=fore-aft; SS=side-to-side; STD=Standard deviation

1) The blade orientation from the test in 2010 was different compared to the test in 2004 and the model.

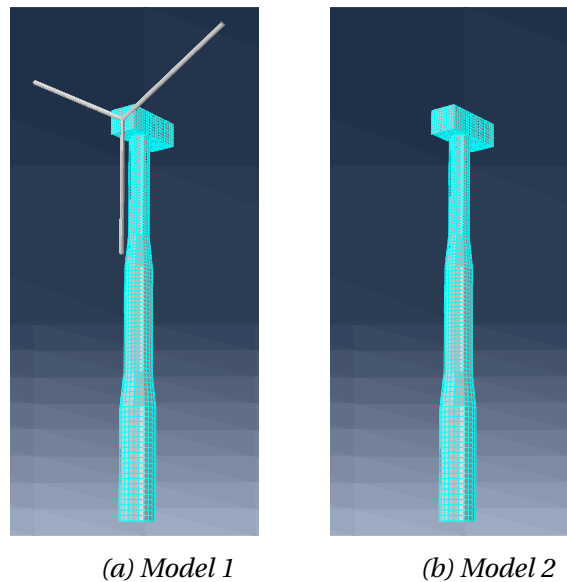


Figure 6.3: The two FE-models of the 65-kW Nordtank wind turbine

Geometry, Materials & Mesh

The tested unit is a 23m high wind turbine manufactured in Denmark by Nordtank. The wind turbine is relatively small in size and capacity, but represents after all the typical structure of a wind turbine with a tabular cylindrical steel tower topped with a nacelle [24]. The geometry and mass properties of the Nordtank 65-kW wind turbine is given in table 6.2. Note that 40% of the total weight is located at the top of the tower.

The mass properties and elements used in the model is given in table 6.3 and 6.4 respectively. The mass of each component is assumed uniformly distributed and the material damping is ap-

proximated from the experimental modal damping ratios. A damping of 1% for the first bending mode and 3.5% for the second bending mode is used which corresponds to Rayleigh coefficients $a_0 = 0.043$ and $a_1 = 0.0006$.

Table 6.2: Properties of the experimental 65-kW wind turbine subjected to the shake table test. The data is also transferred to the FE-model in ABAQUS [25, 24]

Component	Value
Geometry	
Rotor diameter	16.0 m
Tower height	21.9 m
Lower section length	8.0 m
Lower section diameter	2.0 m
Middle section length	7.9 m
Middle section diameter	1.6 m
Top section length	6.0 m
Top section diameter	1.2 m
Tower wall thickness	5.3 mm
Rotor hub height	22.6 m
Mass	
Tower	6 400 kg
Nacelle	2 700 kg
Hub	700 kg
Rotor blade (each)	300 kg
Nacelle + hub + blades	4 300 kg
Total mass	10 700 kg

Table 6.3: Material properties and element types in the FE-model in ABAQUS

Component	Mass density $\rho [kg/m^3]$	Youngs Modulus $E [MPa]$	Poisson's ratio $\nu [-]$
Tower	10947	200 000	0.3
Nacelle	492	210 000	0.3
Blades	1194	10 000	0.3

The geometry of the nacelle is visually determined from available figures in technical data sheets. In the FE-model the nacelle is modelled as a box with dimensions $l \times w \times h = 3.9m \times 1.6m \times 1.4m$ and the hub is modelled as a point mass at the connection between the nacelle and blades. The models matches the given hub height of 22.6m. The nacelle in the tested unit is slightly offset to

Table 6.4: Mesh properties

Component	Element	Number
Tower	Shell, S4R	2222
Nacelle	Solid, C3D8R	2112
Hub	Point mass	1
Blades	Beam, B31	24

reduce the overall eccentricity of the combined rotor/nacelle system [25]. In model 1 the nacelle is placed with an estimated offset of $e = 0.35m$ between the nacelle and tower's center of gravity. This reduces the bending moment from the hub and blades around the tower top from 30.6kNm ($e = 0m$) to 15.8kNm. The lumped top mass in model 2 has no offset.

Constraints & Boundary Conditions

The nacelle is coupled to the tower with a *shell-to-solid* coupling shown in figure 6.4a and the blades are constrained to follow the motion of the nacelle surface with a *beam* connector. In reality the wind turbine tower is stiffened by floors and other structural elements that are not known in detail. To make the tower deform in a realistic manner, stiffening rings are assigned to the tower approximately every fourth meter as shown in figure 6.4b. A *link* multipoint constraint constrains all the translational DOF in a node region to a master node. Further, the connection between the tower base and shake table is assumed rigid.

6.3 Model Simplifications & Sources of Errors

A FE-model contains two main sources of errors; *modelling* errors and *discretization* errors. A finite element analysis is performed on a *mathematical model* which represent a simplification of real geometries, boundary conditions, material properties and loads. The mathematical model is further discretized into a mesh of finite elements. Modelling errors can be reduced by making the mathematical model more realistic, and discretization errors can be reduced by mesh refinement and better suited element types. The simplifications listed under are all sources of

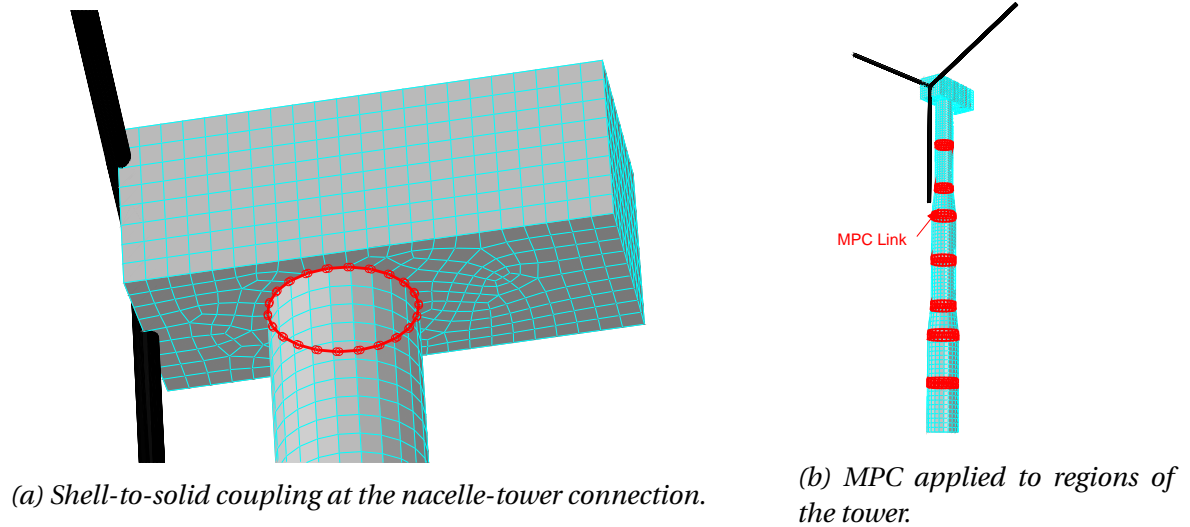


Figure 6.4: Applied constraints to the Nordtank wind turbine model.

modelling errors.

- The tower base is assumed rigidly connected to the shake table, whereas the bolted connection will behave more flexible in real-life.
- Interior structural elements are excluded. Real-life turbines have floors, stairs and additional stiffening along the tower. Instead, constraints are applied to the tower make it obtain a realistic deformation pattern during seismic excitation.
- The geometric shape, size and placement of the nacelle, hub and blades are simplified. In addition, constant thickness is assumed for all tower section.
- All masses are uniformly distributed, whereas real-life wind turbines have a more complex mass distribution along the tower and in the nacelle.
- Damping is represented by Rayleigh damping which depend on the assigned damping coefficient of two frequencies.

6.4 Results & Discussion

The six first eigenmodes for the two models are given in table 6.5 and shown in figure 6.5 for model 1. Both models are able to accurately represent the two first bending modes. Model 1 has an opposite order in which the modes occurs compared to the experimental results.

Table 6.5: Eigenfrequencies obtained from two different models; one model including hub and blades and one with a lumped top mass.

Number	Real		Model 1		Model 2	
	Type	f [Hz]	Type	f [Hz]	Type	f [Hz]
1	FA	1.69	SS	1.68	FA	1.69
2	SS	1.71	FA	1.68	SS	1.70
3	Coupled	11.3	T	8.05	FA	11.20
4	FA	11.9	SS	9.72	SS	11.74
5	SS	12.4	FA	9.93	T	13.09

Model 1: Explicit models hub and blades

Model 2: Lumped top mass

FA: fore-aft; SS: side-side; T: torsional

The reason can be the assumed geometry of the nacelle. 40% of the total mass is located in the tower top, and hence the distribution of this mass will highly influence the response. It is observed that the torsional mode increases from 8.05 Hz to 13.09 Hz in model 2. The blades and hub contribute to a large moment of inertia around the tower, and this contribution is significantly reduced in model 2. As a consequence the torsional frequency increases. Further work may suggest to study the torsional seismic response of wind turbines.

The second bending modes are less accurately compared to the first ones; model 1 and 2 exhibits 20% and 6% lower values respectively. The results may suggest a too soft tower. Assuming a too soft tower, accurate results for the first bending modes are still obtained due to the rigid base boundary condition which stiffens the response. A softer tower in combination with a rigid connection results in an overall accurate response.

For higher modes the eigenfrequencies are less influenced by the base boundary condition causing in softer response. The combination of a rigid base and a too soft tower is an explanation to the increasing deviation between the two first and the two second bending modes.

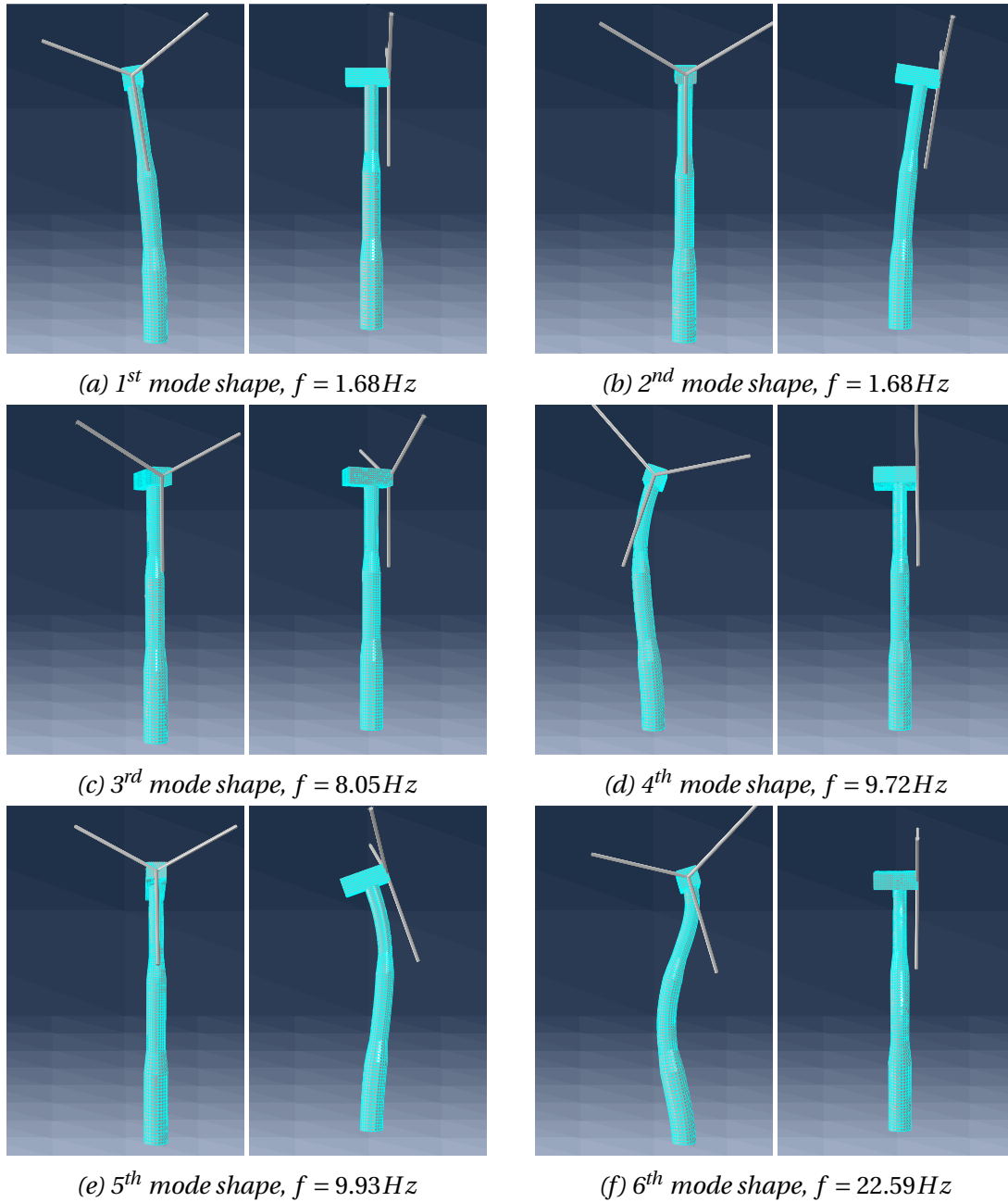


Figure 6.5: The six first modeshapes and corresponding eigenfrequency of model 1.

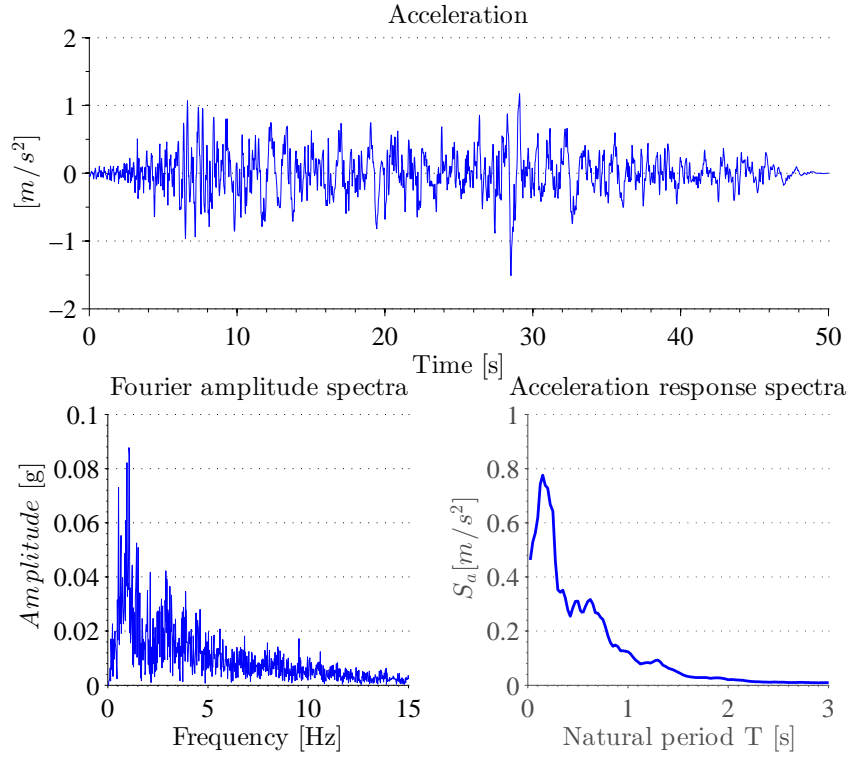


Figure 6.6: Acceleration time serie, Fourier amplitude spectra and response acceleration spectra ($\beta = 5\%$) for the normal component of the Landers earthquake.

The seismic excitation is from the Landers earthquake shown in figure 6.6. The models are excited in the side-side direction and the seismic response is given for the four localizations along the tower shown in figure 6.7. The time history response of the accelerations is given in figure 6.9 for both models. The displacements are given in figure D.2 in the appendix.

The experimental result in terms of acceleration time history response is shown in figure 6.8. It is seen that the tower is mainly excited in its fundamental mode since the response from the tower bottom to the nacelle is monotonically increasing. The numerical results for both models are shown figure 6.9. The peak nacelle acceleration is $a_{peak,1} = 0.4016g$ and $a_{peak,2} = 0.3545g$ for model 1 and model 2 respectively. The deviation compared to the experimental result of $a_{peak,exp} = 0.28g$ are 43% and 27%.

The validation concludes that model 2 with the lumped to mass gives more accurate results in both the modal analysis and in the time domain analysis. Model 1 contains too many uncertainties with respect to nacelle placement and blades properties. Since accelerations are a

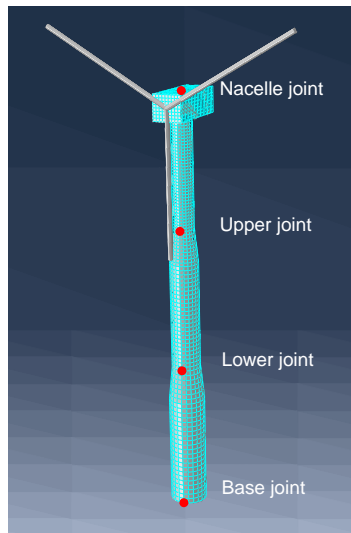


Figure 6.7: Localization of output sections and points

highly sensitive measurement, a error of 27% is satisfactory. Hence, this model type 2 will be used later in the simulations concerning the Vestas wind turbine.

6.5 Parametric Study

To obtain a better understanding of how changes in the model influence the response, a parameter study of selected parameters is carried out. The considered parameters are the tower stiffness, nacelle mass, tower mass and initial moment about the tower top. The parameters are independently varied with model 2 taken as the reference model and the appurtenant change in the eigenmodes are presented and discussed.

Figure 6.10 shows the variation of the first natural frequency as a function of different model properties. It is seen that the tower thickness and nacelle mass influences the natural frequency the most. These properties should be carefully determined to ensure correct responses. Further, all results coincide with the expected tendency; an increase in tower stiffness (tower thickness) increases the number of oscillations as the tower gets stiffer, an increase in the tower mass or the nacelle both give an reduction in frequency as the inertia gets larger and an increase in the tower top moment reduces the frequency for the same reason.

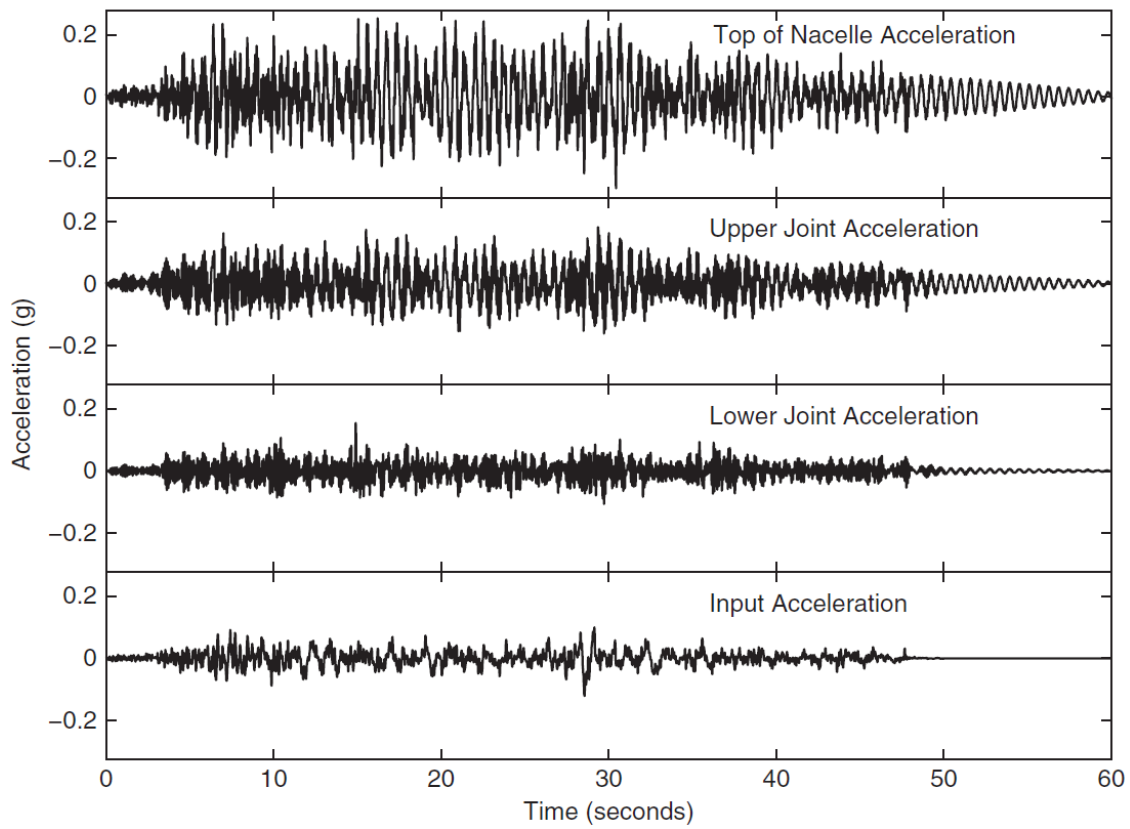


Figure 6.8: Experimental acceleration time history response of the Nordtank wind turbine.

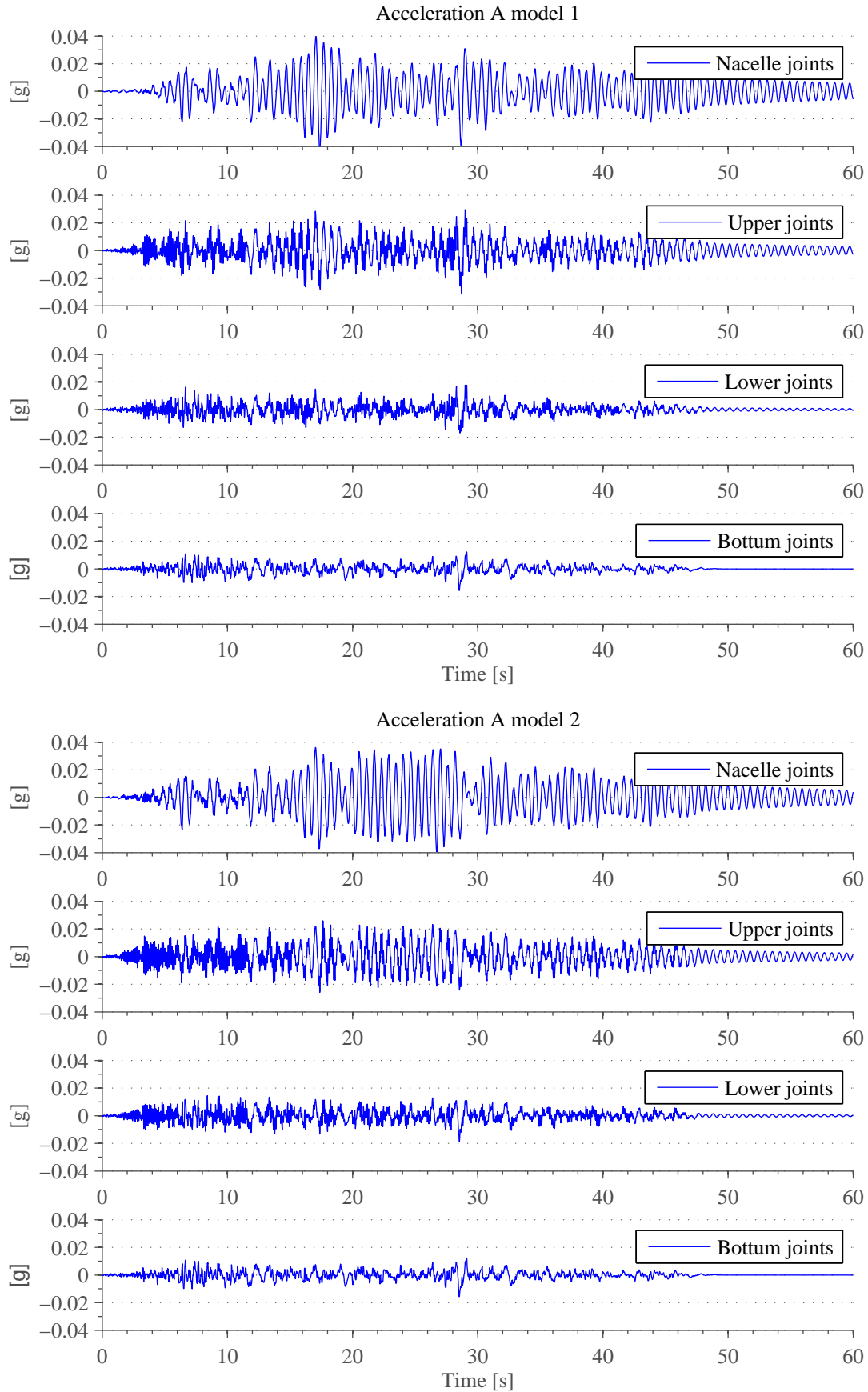


Figure 6.9: Acceleration time response of the shell model for a) model 1 which explicitly represent the nacelle and blades and b) model 2 which has a lumped mass representation of the nacelle and blades

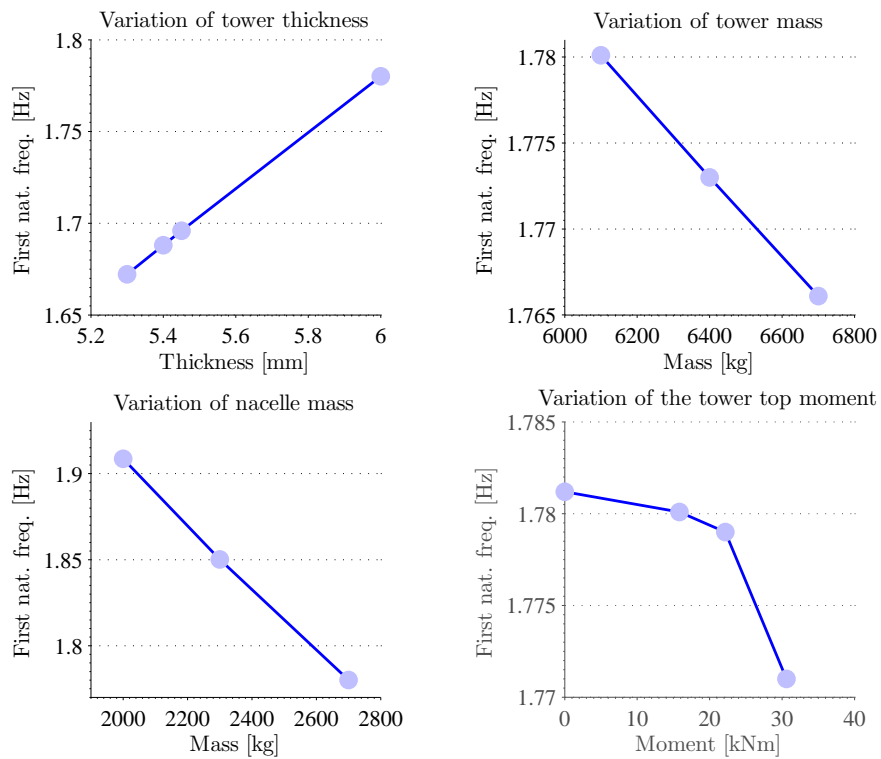


Figure 6.10: Change in the first natural frequency for different model parameters.

Chapter 7

Model of a Vestas 3.0-MW Wind Turbine with a Skirted Foundation

This section presents a fully integrated model consisting of a parked Vestas wind turbine, a skirted foundation and a uniform soil.

7.1 Model Description

Figure 7.1 provide a sketch of the Vestas wind turbine and the skirted foundation prototype installed in Aalborg. The tower is a tapered hollow steel tube mounted to the top lid of the skirted foundation and stiffened by twelve triangular plates. The turbine has a total weight of approximately 270 tons where as much as 40% of the mass is localized in the top.

The integrated model consists of four individual parts that must be correctly assembled; the soil, foundation, wind turbine shaft and the nacelle. The main challenge was to model the foundation into the soil. The two tested approaches were:

1. *Contact*: The bucket was created as an individual part and placed in the adapted cut in the soil. Contacting surfaces were defined and a *rough* sliding formulation was applied which represent fully bounded interacting surfaces.

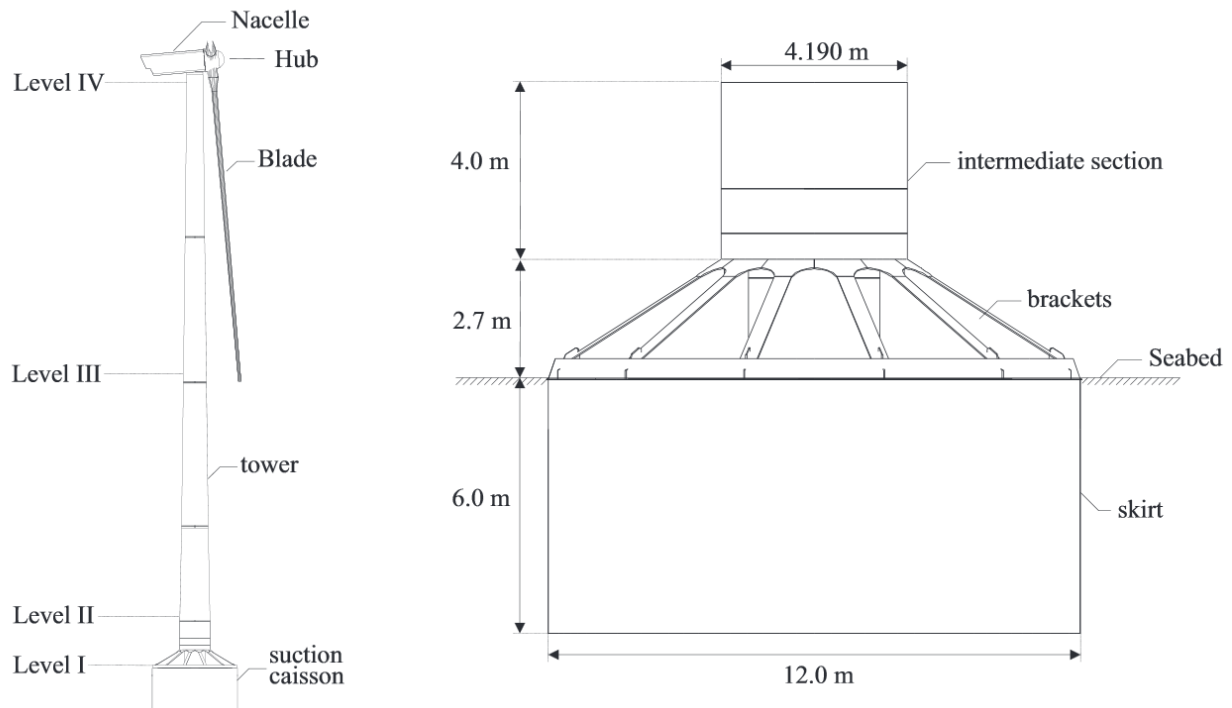


Figure 7.1: Sketch of the different parts of the wind turbine and skirted foundation [15].

2. *Skin*: The bucket was created as a skin property in the interior of the soil. A skin is a thin layer of elements sharing the same nodes as the surface it is assigned to, but can have different material properties. A skin is fully bounded to its surface.

The contact formulation was challenging to manage for the skirted foundation geometry because of all the contacting nodes at the skirt and soil and the circular skirt profile. The contact formulation was evaluated to contain to many uncertainties based on a visual observation of the obtained stress field shown in figure 7.2. The bucket obtained a realistic stress field for an applied unit moment, whereas the soil displayed an odd stress distribution.

To eliminate the uncertainties related to the contact approach, the simpler skin definition was adopted. The final model is shown in figure 7.3 and the skin definition is illustrated in figure 7.4.

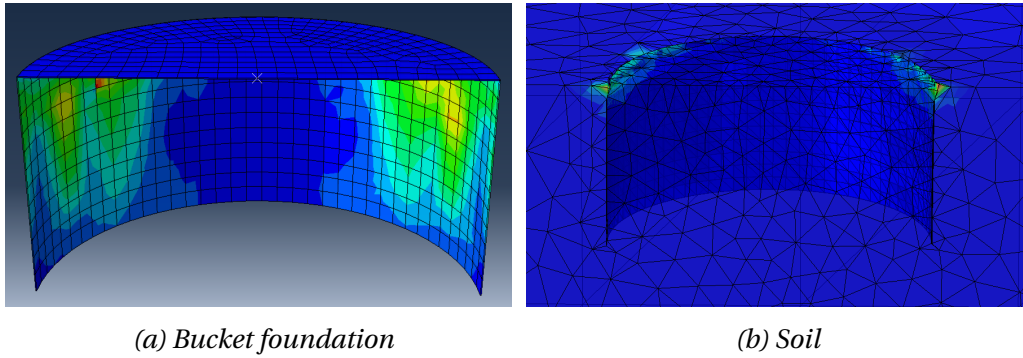


Figure 7.2: Stress field in bucket and soil with a contact formulation. A unit moment is applied at the top lid.

Geometry & Materials

The soil volume has dimensions $l_x = 120m$, $l_y = 30m$ and $l_z = 60m$. The geometry and mass properties of the wind turbine, foundation and soil are given in table 7.1, 7.2 and 7.3. All materials are assumed homogenous and linear elastic.

Table 7.1: Properties of the Vestas V90 3.0 MW wind turbine [2, 15].

Geometry	
Tower height	80 m
Tower diameter bottom	4.19 m
Tower diameter top	3.14 m
Rotor diameter	90 m
Blade length	45 m
Swept area	6.362 m ²
Nacelle length	9.65 m
Nacelle width	3.65 m
Nacelle height	~ 3.5 m
Mass	
Nacelle	70 t
Blade	6.7 t
Hub	22 t
Hub inc. blades	42.1 t
Tower	155 t
Total	267.1 t

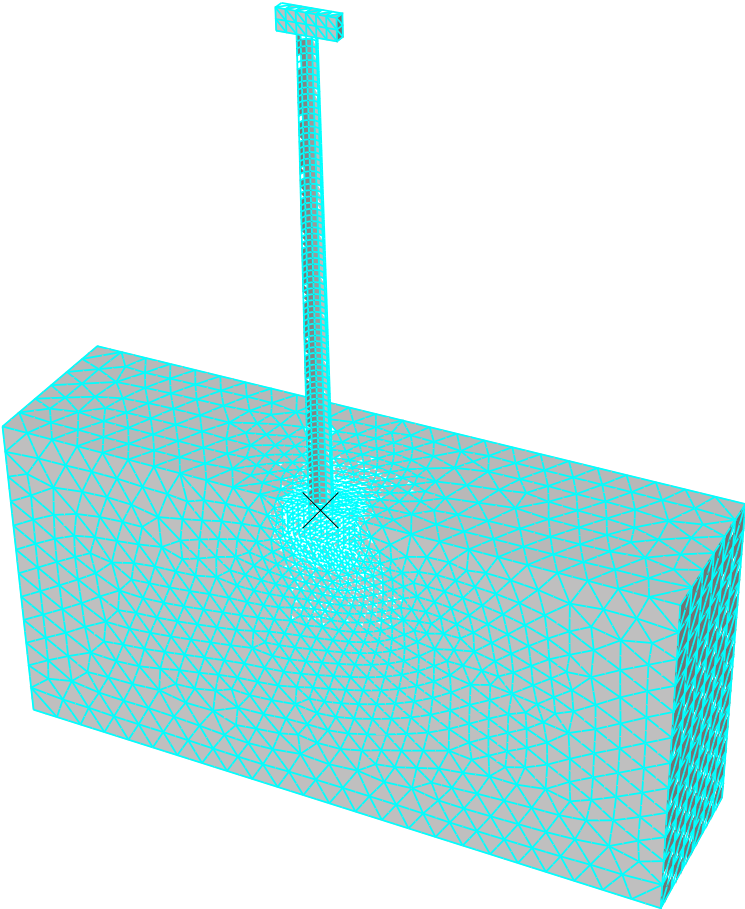


Figure 7.3: Model of the Vestas wind turbine mounted in soil.

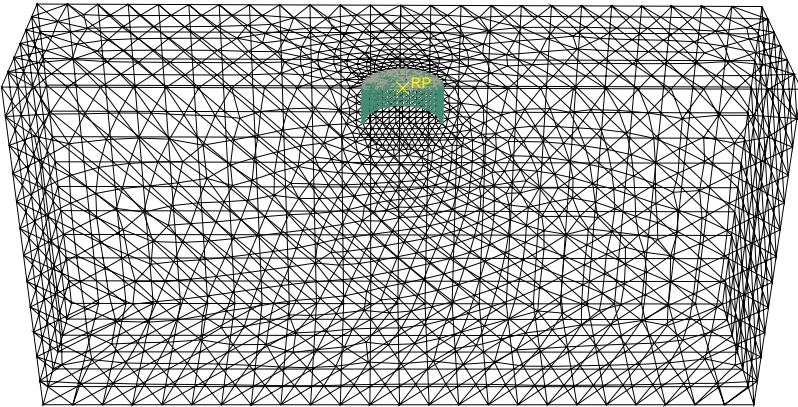


Figure 7.4: Visualization of the skin elements in the soil.

Table 7.2: Properties of the bucket foundation [15].

Component	Value
Geometry	
Radius	6.0 m
Skirt length	6.0 m
Skirt thickness ¹⁾	25-30 mm
Top lid thickness ²⁾	50 mm
Stiffener thickness	15-30 mm
Mass	
Total	~ 140 t
Mass density	11300 kg/m ³

1) 30mm is used in the FE-model

2) Estimated value

Table 7.3: Material properties in the fully integrated model.

Type	Density $\rho \left[\frac{kg}{m^3} \right]$	Elasticity $E \left[\frac{N}{mm^2} \right]$	Poisson's $\nu [-]$
Clay	1700	200	0.47

BC & Constraints

Only half parts are modeled due to the symmetric model definition. The tower is rigidly connected to the assumed rigid top lid of the foundation. Further, the boundaries and constraint defined in section 5 and 6 are adapted.

The seismic loads creates horizontally propagating waves which is reflected at the soil boundaries. It is effective to have a relative large soil length to reduce the wave reflections since the wave amplitudes decrease due to material damping. Hence, a soil length of 120 m is chosen in the longitudinal direction, whereas a shorter length of 30 m is used in the transversal direction. An improvement to the model would be to include dashpots at the wave reflecting surfaces. Then, also smaller soil volumes could be used in the simulations.

Elements & Mesh

A summary of the mesh properties is given in table 7.4. An element size of 1 m was requested at the skirt boundary to obtain a more detailed stress distribution in the interacting zone. The element size is linearly increasing to a maximum of 5m at the outer soil boundaries.

Table 7.4: Mesh properties Vestas wind turbine model.

Component	Element	Number
Tower	Shell, S4R	468
Nacelle	Solid, C3D4	158
Hub	Point mass	1
Soil	Solid, C3D10	26353
Foundation	Shell, S3	349

7.2 Model simplifications

In addition to the simplifications mentioned in section 5 and 6, the following simplifications applies to the fully integrated model:

- All materials are linearly elastic, whereas a more realistic soil material definition would have viscoelastic properties.
- The skin definition prevents occurrence of gaps and sliding in the foundation/soil interface, whereas this is highly present in real structures.

7.3 Seismic Load & Eigenmodes

The model is subjected to the Nahanni earthquake with properties given in figure 7.5. The frequency content in this earthquake matches the design response spectra in EC8. The fully integrated model is used as a reference to the simplified models later presented. The responses are given for the four points along the tower shown in figure 7.6a. An eigenfrequency analysis shows satisfactory results with experimental results. The result is given in table 7.5 and figure 7.6b.

Table 7.5: The two first natural frequencies of a parked V90 3.0 MW wind turbine installed at the bucket foundation [15]. Compared to a FE-beam model.

Configuration	Experimental		FE- model ¹⁾	
	f_1 [Hz]	f_2 [Hz]	f_1 [Hz]	f_2 [Hz]
Total	0.3	2.13	0.32/0.33	2.64/2.85
Without blades	0.33	2.10-2.14	-	-
Without blades + nacelle	0.72	2.88	-	-

1) Ten beam elements with varying profiles and a lumped top mass

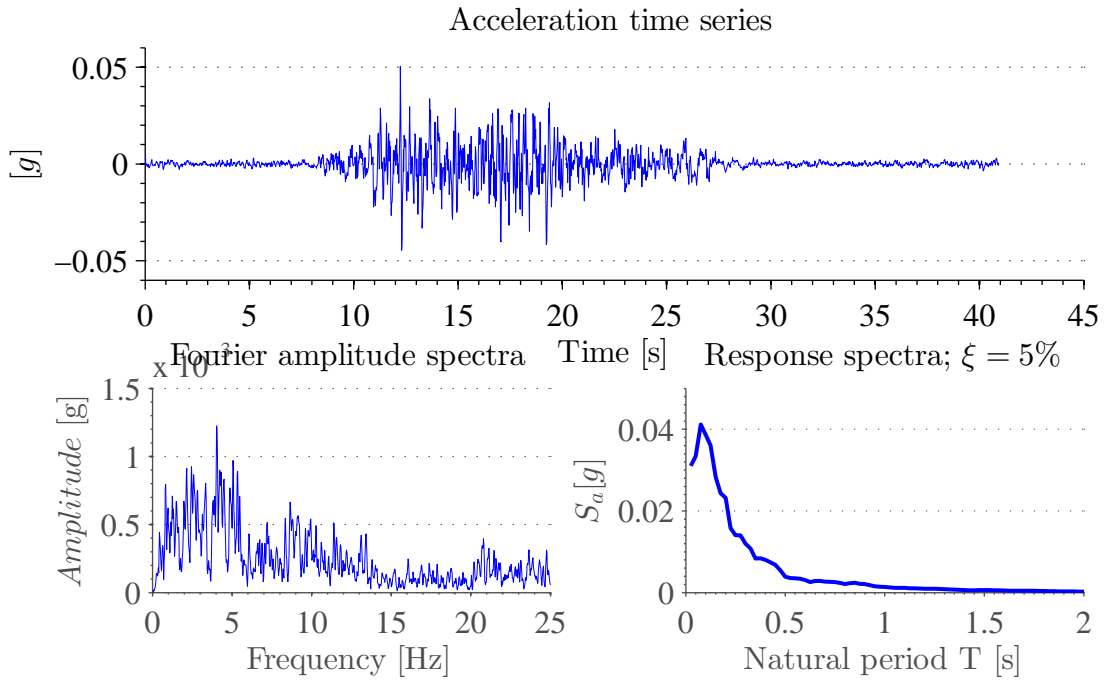


Figure 7.5: Acceleration time serie, Fourier amplitude spectra and response acceleration spectra ($\beta = 5\%$) of the horizontal component of the Nahanni earthquake.

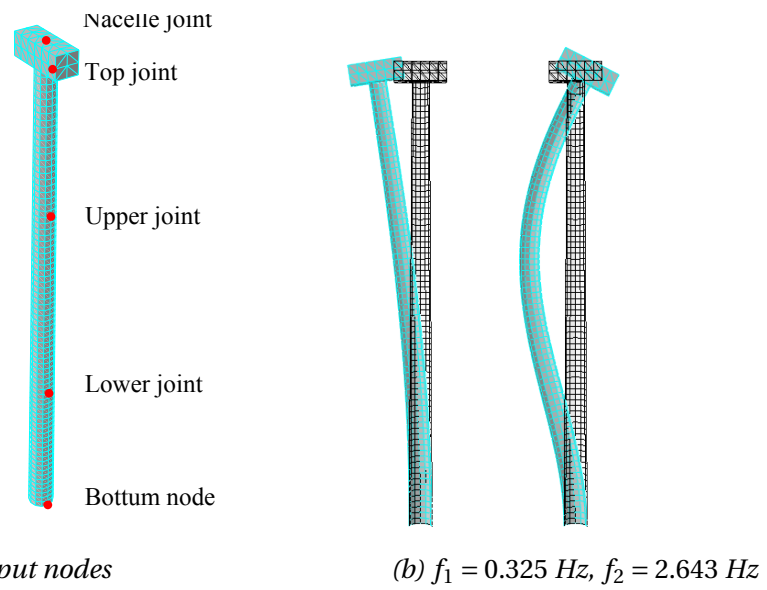


Figure 7.6: Output nodes and eigenfrequencies of the wind turbine tower.

Chapter 8

Simplified FE-models

This chapter presents the numerical procedure to create a linear elastic spring and dashpot model of the Vestas V-90 wind turbine installed at the skirted foundation. The three-step-method presented in section 3.6 is utilized. Further, focus is given to how changes in soil/foundation interface conditions influences the stiffness.

8.1 Static Stiffnesses & Damping of the Bucket Foundation

This section presents static stiffnesses and damping of the skirted foundation embedded into a soil stratum-over-bedrock. Numerical values are compared to analytical stiffness formulas for homogeneous soils provided by Gazetas [9]. The frequency dependent terms in the spring stiffnesses are ignored. The analysis is performed for two different soil profiles: 1) a *homogenous* soil and 2) a soil with a thin *inner* soil layer with varying elasticity to model soil/bucket interface conditions.

Methodology

A horizontal translational and rotational DOF are sufficient to describe the motion of the top lid of the foundation. A static unit force and moment is applied to the reference point of the foun-

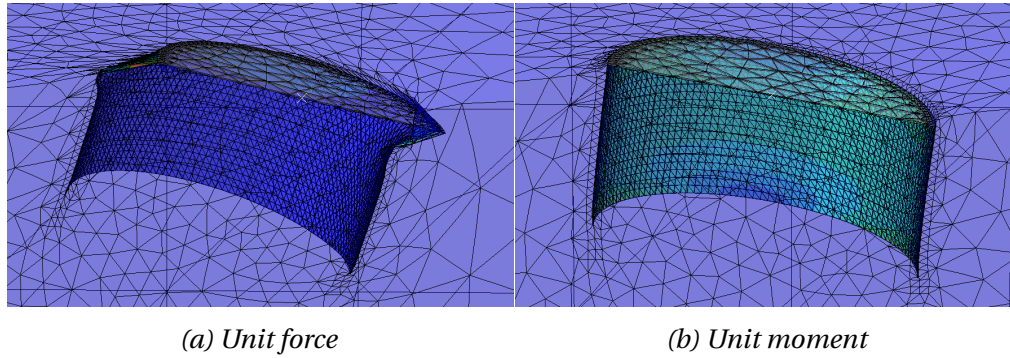


Figure 8.1: Displacements for a unit force and moment at the bucket foundation. Scale $1 \cdot 10^{10}$.

dation as shown in figure 8.1 and the correspondingly displacement and rotation is computed. Mathematically, the following relationship is established:

$$\mathbf{FR} = \mathbf{D} \longrightarrow \mathbf{KD} = \mathbf{R} \quad \text{where} \quad \mathbf{K} = \mathbf{F}^{-1} \quad (8.1)$$

The terms in the flexibility matrix f_{ij} reads displacement/rotation in node i due to a unit force/-moment in node j . The terms in the stiffness matrix k_{ij} reads force/moment in node i due to a unit displacement/rotation in node j . The matrices are symmetric about the diagonal, such that $i \neq j$ $f_{ij} = f_{ji}$ and $k_{ij} = k_{ji}$.

$$\mathbf{F} = \begin{bmatrix} f_{11} & f_{12} \\ f_{21} & f_{22} \end{bmatrix} \quad \text{and} \quad \mathbf{K} = \begin{bmatrix} k_{11} & k_{12} \\ k_{21} & k_{22} \end{bmatrix} \quad (8.2)$$

Note that an unit displacement in general also produces a rotation and vice versa. These responses are represented by the off-diagonal terms in the flexibility and stiffness matrix, but are not included in the spring model.

8.1.1 Analytical Formulas

A key parameter in determining the static stiffnesses for rigid embedded foundations is the embedment ratio $\frac{D}{R}$; the embedment depth to foundation radius. Table 8.1 gives the static stiff-

Table 8.1: Static stiffnesses of rigid embedded cylindrical foundation welded into a homogenous soil stratum-over-bedrock

Loading	Static stiffness	Profile
Vertical	$\frac{4GR}{1-\nu} \left(1 + 1.28 \frac{R}{H}\right) \left(1 + \frac{1}{2} \frac{D}{R}\right) \left(1 + 0.85 - 0.28 \frac{D}{R} \frac{D/H}{1-D/H}\right)$	
Horizontal	$\frac{8GR}{2-\nu} \left(1 + \frac{1}{2} \frac{R}{H}\right) \left(1 + \frac{2}{3} \frac{D}{R}\right) \left(1 + \frac{5}{4} \frac{D}{H}\right)$	
Rocking	$\frac{8GR^3}{3(1-\nu)} \left(1 + \frac{1}{6} \frac{R}{H}\right) \left(1 + 2 \frac{D}{R}\right) \left(1 + 0.7 \frac{D}{H}\right)$	
Coupled horizontal rocking	$0.40K_h D$	
Torsion	$\frac{16}{3} GR^3 \left(1 + 2.67 \frac{D}{R}\right)$	

nesses for different types of loading for a rigid foundation embedded into a *homogenous* soil. It is assumed that the foundation walls and the contacting soil remain in full contact during cyclic loadings. The formulas are developed for the geometry shown in table 8.1.

In reality no tensile stresses can be sustained in the soil and the shear tractions cannot violate Coulumb’s friction law. Hence, separation and sliding are likely to occur between sidewalls and backfill, depending primarily on the mode of vibration and the nature and method of placement of the soil [9]. The formulas represents thus an upper limit to the static stiffness values.

From the formulas it is evident that an increase in relative embedment $\frac{D}{R}$ is more beneficial to the rocking stiffness (a factor of 2) compared to the horizontal stiffness (a factor of $\frac{2}{3}$).

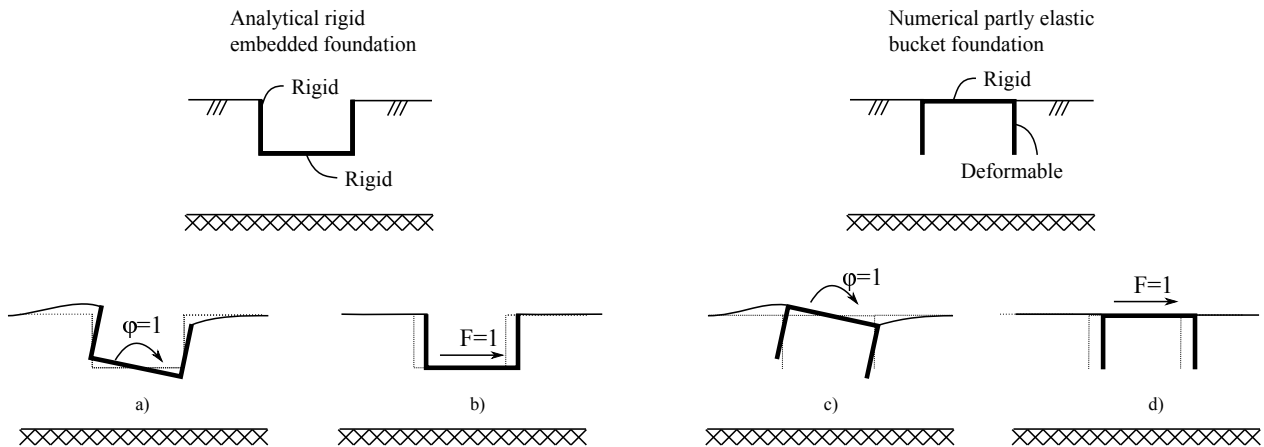


Figure 8.2: Comparison of the horizontal and rocking deformation between the analytical rigid embedded foundation and the partly deformable bucket foundation.

The skirted foundation deviates in geometry and elasticity from the foundation type given in table 8.1. The following points explain the sources of errors related to the use of the formulas for the skirted foundation:

1. *Elasticity in foundation:* The formulas are for a completely rigid foundation, whereas the skirt is deformable and hence reduces the stiffnesses.
2. *Foundation geometry:* The deviation in foundation geometry changes the deformation profile of the soil when subjected to external displacement. The skirted foundation gives an additional soil volume inside the skirt as illustrated in figure 8.2. The two zones where forces develop are 1) the skirt wall and 2) the bottom lid or top lid.
 - (a) *Horizontal loading:* The cylindrical wall compresses and tensions the outer surrounding soil for both foundation types as shown in figure b) and d). The inner soil volume in the bucket translates mainly as a rigid body and gives no additional resistance. Shear forces develop at the bottom lid for the rigid embedded foundation. The main part of the shear resistance of the skirted foundation develops in the horizontal soil plane at the skirt tip.
 - (b) *Moment loading:* For $\frac{D}{R} > 2$ the largest displacements occur at the free skirt tip at the surface for the rigid embedded foundation type seen in figure a). It is easier to deform the soil localized close to the surface since this area provides lower resistance. For the skirted foundation in figure c) the largest displacements occur at the skirt tip where the stiffness of the soil is higher than at the surface. Hence, a larger force is needed to deform the soil in this area.

Despite these differences a comparison between the formulas and the numerical stiffnesses for the bucket foundation is conducted for the case $D = R = 6m$, such that $\frac{D}{R} = 1$. The analysis is conducted for several homogenous soils with elasticities $E = 200MPa$, $E = 100MPa$ and $E = 50MPa$. The results are shown in figure 8.3 and given in table 8.2.

It is seen that the deviation between formulas and numerical results decreases with decreasing soil elasticity. This observation is explained with respect to the elasticity ratio of the bucket and soil. The formulas assume a rigid foundation, whereas the model has a deformable skirt

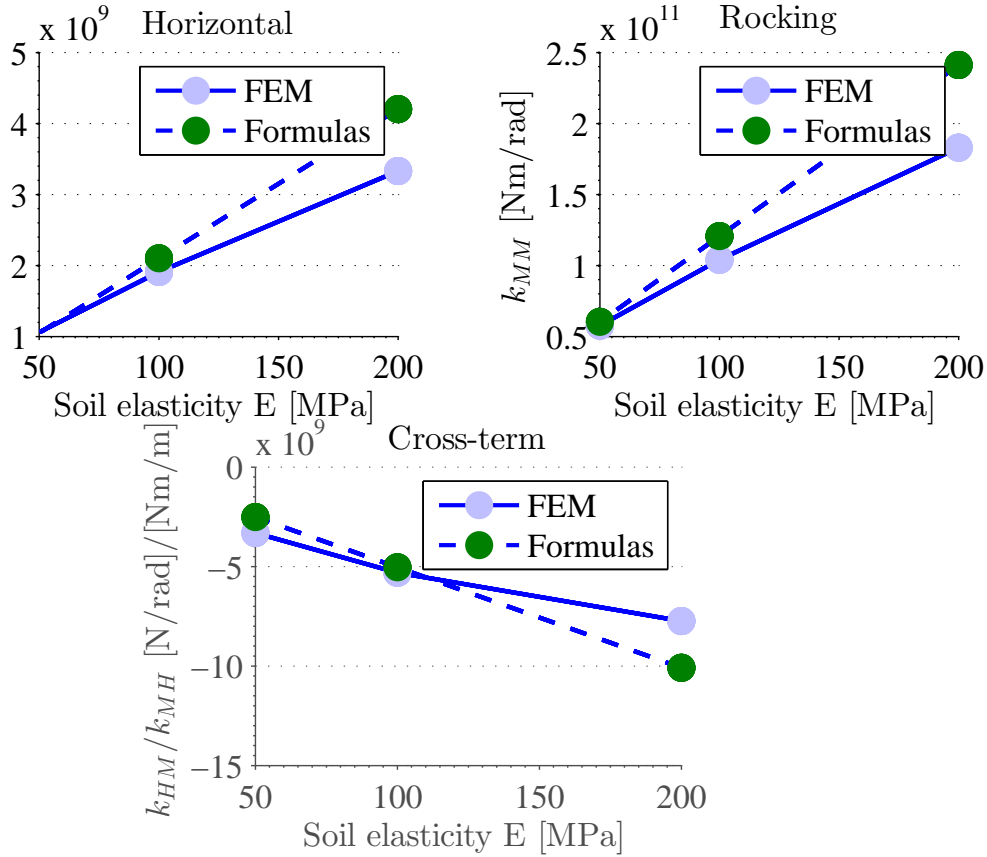


Figure 8.3: Variation of static stiffnesses in a homogenous soil.

with $E = 200\text{GPa}$. As the soil gets weaker the skirted foundation gets a relative larger stiffness, and hence the soil experiences the skirt as *rigid*.

The formulas give an error of only -1.2% and 4.5% for the horizontal stiffness k_{HH} and the rocking stiffness k_{MM} respectively for a soil with $E = 50\text{MPa}$, which is a satisfactory result. For soil elasticities above $E = 100\text{MPa}$ the formulas deviate more than 10% and 15% for k_{HH} and k_{MM} respectively. The formulas should be carefully applied to others foundation geometries, but it is demonstrated for the particular case $D = R = 6\text{m}$ that the formulas provide satisfactory results for soil elasticities below $E \sim 100\text{MPa}$.

8.1.2 Different Soil/Skirt Interface Conditions

Lower elasticity properties are assigned to a thin inner soil layer (as illustrated in figure 8.4a) to study the effect of a weaker soil/skirt interface to the soil/foundation stiffnesses. The weaker zone has a width of total 60cm and has a very fine mesh as shown in figure 8.4b.

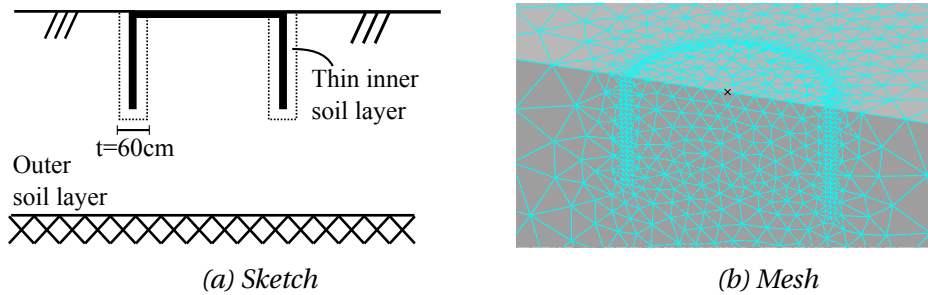


Figure 8.4: Inner soil layer modeling the soil/skirt interface conditions.

The results for different interface conditions are shown in figure 8.5 and given in table 8.3 together with the percentual decrease wrt. the homogeneous soil condition with $E = 200\text{MPa}$. A quadratic decrease in all stiffnesses are obtained as the inner soil gets weaker.

These results can provide valuable information in combination with the seismic response of the wind turbine tower. A reduction of -1.9% and -3.6% in the horizontal and rocking stiffnesses for a 25% weaker inner soil may appear small, but can still have a considerable impact on the seismic response.

Table 8.2: Static stiffnesses of bucket foundation compared to formulas for varying soil elasticity in a homogenous soil stratum-over-bedrock.

Soil E [MPa]	Horizontal			Rocking			Cross-term		
	Num.	Form.	Error	Num.	Form.	Error	Num.	Form.	Error
200	3.33	4.20	26.3%	1.83	2.41	31.6%	7.74	10.08	30.3%
100	1.91	2.10	10.2%	1.04	1.20	15.5%	5.31	5.04	-5.0%
50	1.06	1.05	-1.2%	0.58	0.60	4.5%	3.32	2.52	-24.0%

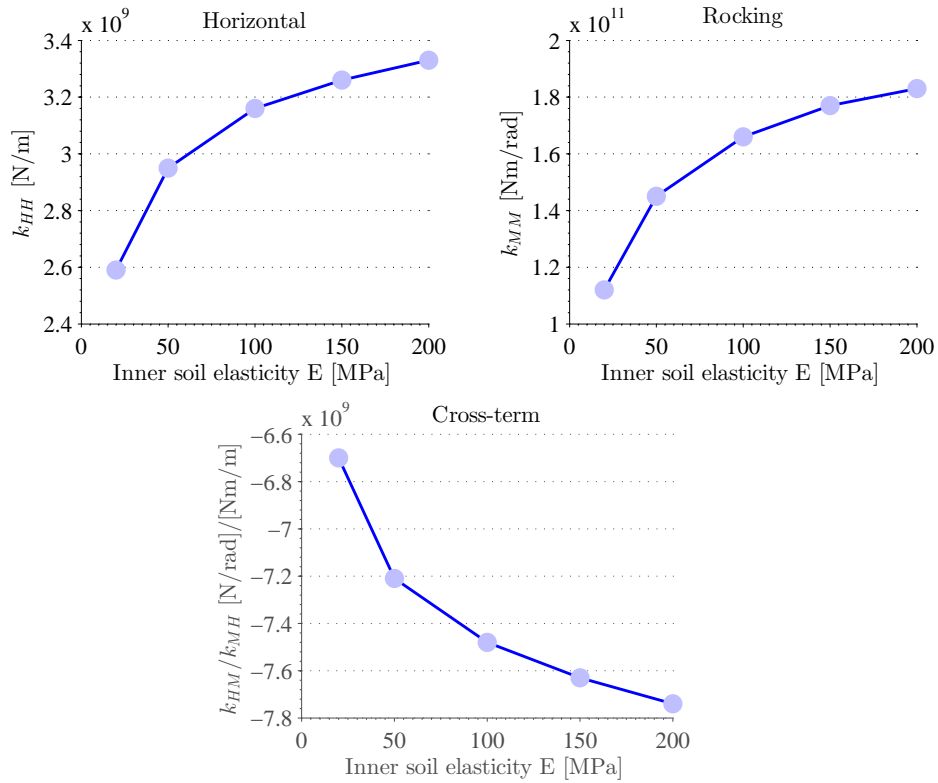


Figure 8.5: Static stiffnesses for varying soil/bucket interface conditions. Outer soil has elasticity $E = 200\text{MPa}$ and $V_S = 200\frac{m}{s}$

Table 8.3: Static stiffnesses of bucket foundation for varying interface conditions. The outer soil layer has an elasticity of $E = 200\text{MPa}$.

Inner soil E [MPa]	Horizontal k_{HH}		Rocking k_{MM}		Cross-term k_{HM}/k_{MH}	
	$10^9[\frac{N}{m}]$	Reduction	$10^{11}[\frac{Nm}{rad}]$	Reduction	$10^9[\frac{N}{rad} / \frac{Nm}{m}]$	Reduction
200 ¹⁾	3.33	Referance	1.83	Referance	7.74	Referance
150	3.26	-1.9 %	1.77	-3.6%	7.63	-1.5%
100	3.16	-4.9 %	1.66	-9.2%	7.48	-3.4%
50	2.95	-11.3 %	1.45	-20.8%	7.21	-6.9%
20	2.59	-22.3 %	1.12	-38.9%	6.70	-13.4%

1) Homogeneous soil condition. The reduction in stiffness is referred to this state.

Damping

The frequency-independent damping coefficient c for swaying and rocking is approximated by the following formulas for the foundation type in table 8.1 [9]

$$c_{HH} \approx \frac{\pi(2-\nu)}{8} \cdot \frac{1 + 1.3(D/R)[1 + (3.6/\pi(1-\nu))]}{1 + \frac{2}{3}(D/R)} \quad (8.3)$$

$$c_{HR} = 0 \quad (8.4)$$

The result for a range of embedment ratios $\frac{D}{R}$ is given in table 8.4. Note that the damping only depend on the ratio. In other words, a small and a large foundation will have the same damping as long as the embedment ratio is the same for both cases.

Table 8.4: Frequency-independent damping coefficients of rigid embedded cylindrical foundation welded into a homogenous soil stratum-over-bedrock

Ratio	Damping coefficient
$\frac{D}{R}$ [-]	$c_H \left[\frac{N}{m/s} \right]$
0	0.60
0.5	0.92
1.0	1.11
1.5	1.24
2.0	1.33

8.2 Kinematic Interaction of the Skirted Foundation

The kinematic step in the three-step method is only made half kinematic to separate the tower from the foundation in the simplified model. An equivalent alternative would be to have a massless foundation as originally proposed in the derivation in section 3.6 and later include the foundation (with mass) in the spring and dashpot model.

The kinematic base input in the spring model is collected at the reference point at the rigid foundation top lid. Figure 8.6 shows the kinematic response from the Nahanni earthquake together

with the free-field response. Note that the presence of the foundation in the soil generates both displacements and rotations and that the kinematic displacements are almost identical to the free-field response. This demonstrates that the skirted foundation conforms to the free-field motions and has little influence on the seismic waves. In addition, the rotations are of very low magnitude indicating that these can be neglected in the seismic simulations.

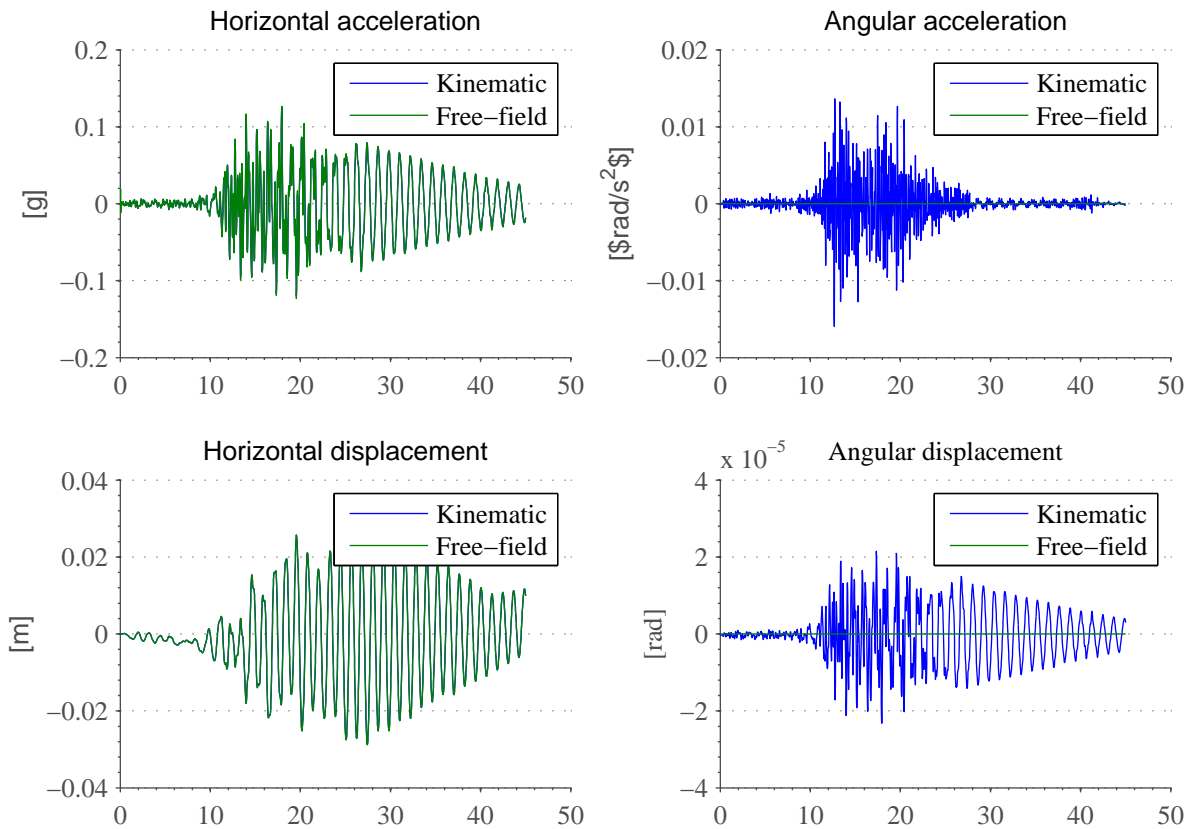


Figure 8.6: Kinematic base input in the spring and dashpot model for the Nahani earthquake

8.3 Spring & Dashpot Model

This section focuses on the last step in the *three-step-method*; i.e the inertial interaction illustrated in figure 8.7. The spring model consists of ten beam elements, two springs and one dashpot as shown in part 3 of figure 8.8 which illustrates the numerical procedure used to establish the spring models.

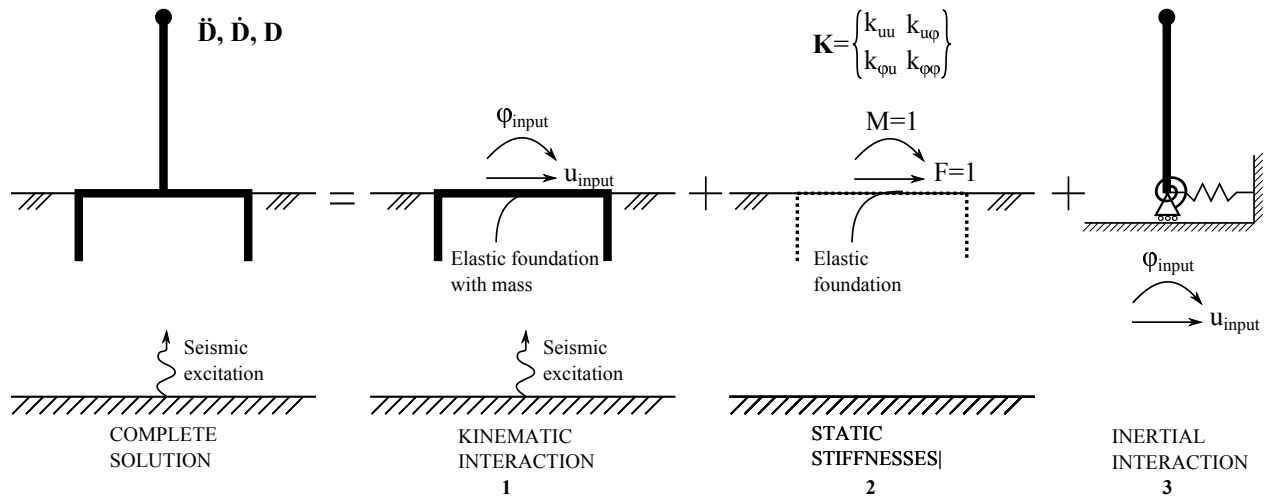


Figure 8.7: The three-step method for the skirted foundation and wind turbine.

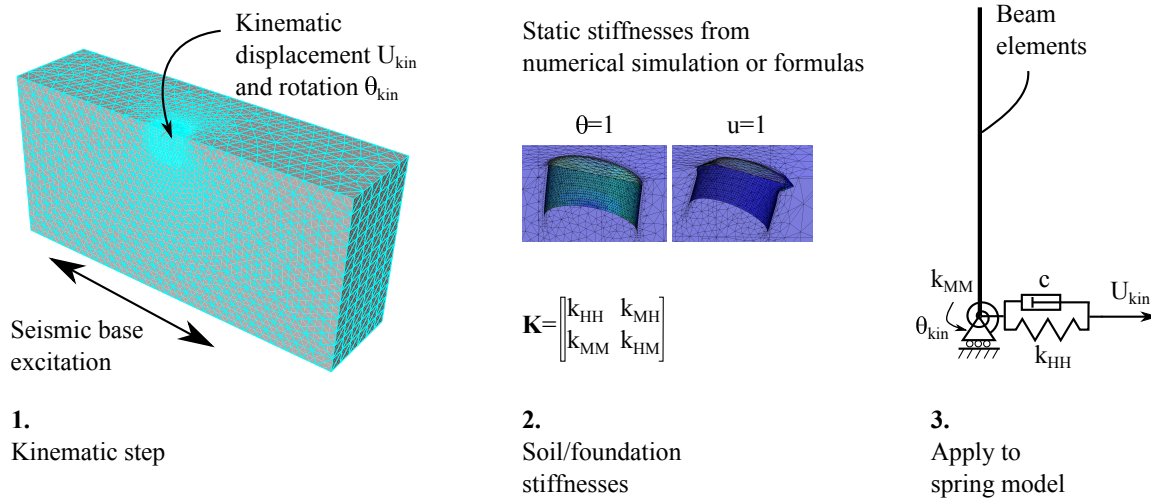


Figure 8.8: Numerical procedure to create a spring model in accordance to the three-step-method.

The spring model approach has two main benefits compared to a fully integrated soil and structure model; *a)* the simulation time is considerably lower compared to a fully integrated model *if* the kinematic base translations and rotations can be estimated from formulas and *b)* the response of different soil/foundation systems can easily be computed by changing the spring properties. The latter becomes even faster if the same kinematic inputs can be used for several geometries.

The spring and dashpot model is faster with respect to modeling and computational time and requires considerably less storage space compared to a fully integrated soil/wind turbine system. In addition, a simple beam model is highly appreciated by FE-analysts because it makes it practical feasible to run parametric studies in a short amount of time.

The spring and dashpot model contains several simplifications and estimations as explained by the following points:

1. *Frequency independent springs and dashpots:* The stiffness and damping of a dynamic system depend on the excitation frequency of the load. The spring model has only frequency independent properties.
2. *Independent spring definitions:* The model excludes the off-diagonal terms in the stiffness matrix. Hence, the magnitude of the rotations occurring from displacements in the spring is determined by the pure rotational stiffness k_{MM} and vice versa.
3. *Damping:* When the structure is added in the inertial step, the skirted foundation vibrates against the surrounding soil, which creates waves in the soil. The value of this radiation damping is highly uncertain.

An eigenmode analysis of the shell model and two beam models provide satisfactory results for the shell model and the two beam models on different base shown in figure 8.9. It is seen that the eigenfrequencies for the beam on flexible base is reduced as expected.

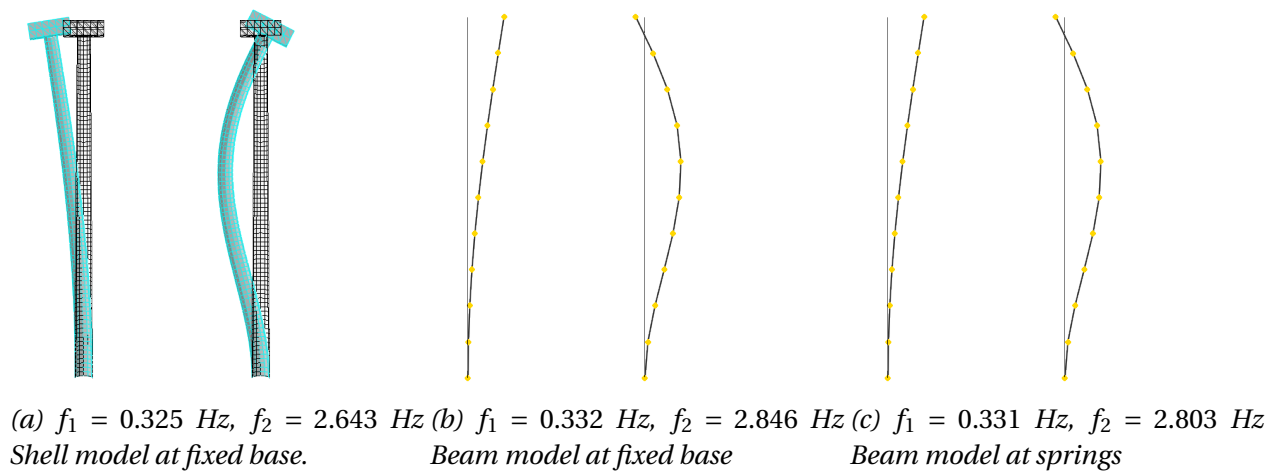


Figure 8.9: The two first fore-aft eigenfrequencies of the Vestas wind turbine.

Chapter 9

Results

This chapter presents the seismic response of the Vestas wind turbine for the established spring model and the fully integrated model. The results are divided into two parts:

Part A: Three-Step Method demonstrates the accuracy of the established spring model in terms of time history responses along the tower compared to the fully integrated model. The influence of different soil materials to the response is investigated for *a)* a homogeneous stiff soil and *b)* a three-layered soil with a relatively weak upper layer. Responses from flexible-base and fixed-base conditions are compared and the importance of kinematic interaction is investigated for the skirted foundation.

Part B: Parametric Study investigates changes in maximal responses along the tower for variations in *a)* the geometry of the skirted foundation with respect to radius and depth and *b)* the tower height.

All simulations are restricted to the linearly elastic range for both the soil and the wind turbine. Further, only static stiffnesses are applied to the springs and constant radiation damping is assumed in all simulations. The soil is bounded to the skirted foundation which prevents the occurrence of gaps and sliding at the soil/foundation interface.

9.1 Part A: Three-Step Method

Figure 9.1 shows the two models of interest in this comparative study. Model *a*) is referred to as the full model (1-step in the graphs) which assembles the soil, foundation and wind turbine. This model is the reference when studying the accuracy of the simplified models. Model *b*) is referred to as the spring model which separates the kinematic and inertial responses. The seismic response are compared in terms of displacement, acceleration, moment and shear time history plots for the four points along the tower previously shown.

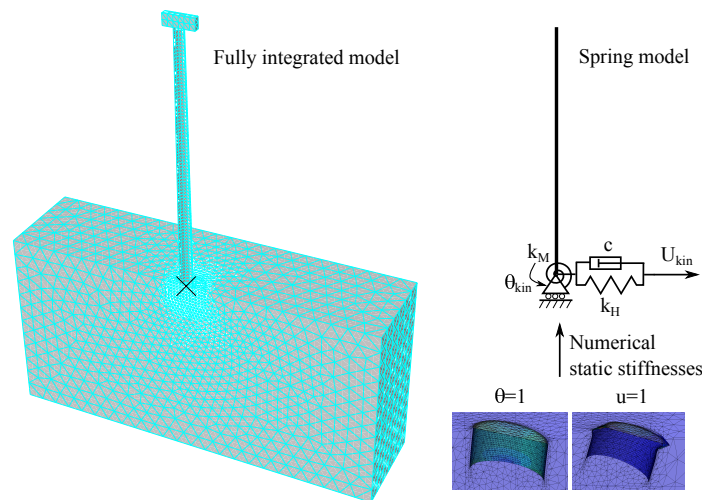


Figure 9.1: The model setups for the comparisons.

Table 9.1 gives the material properties for the two soil profiles shown in figure 9.2. Soil profile *a*) is a homogeneous soil and is referred to as the stiff soil due to its relatively high shear wave velocity. Soil *b*) is a three-layered soil with a weak upper layer. A comparison of the seismic response from the two soil profiles is carried out to demonstrate the effect of different site conditions, but is not given further focus throughout this thesis.

The *accuracy* of the spring approach is measured in terms of the translation and rotation at the bottom beam node relative to the bottom node at the full model. The seismic response of the higher nodes are to a larger extent influenced by the properties of the applied numerical beam elements. Nevertheless, a comparison of responses between several points along the tower provides useful information about the numerical algorithm defined.

Table 9.1: Soil material properties

Soil type	Shear wave velocity $V_S[m/s]$	Mass density $\rho[kg/m^3]$	Youngs Modulus $E[MPa]$	Poisson's ratio ν
Stiff soil	200	1700	200	0.47
Soft soil	50/150/250	1700	13/110/310	0.47

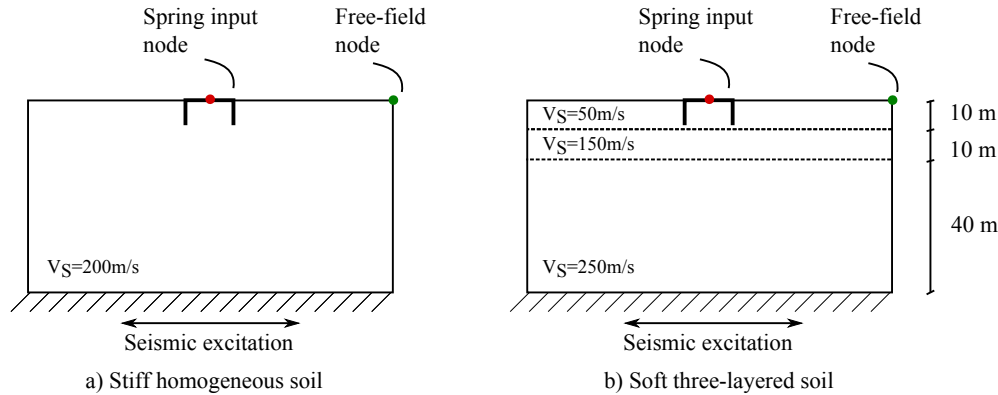


Figure 9.2: A homogenous and a layered soil stratum used in the comparison between the shell model and the three-step-method.

The seismic behaviour along the tower for the spring and shell model is given in figure 9.3, 9.4, 9.5 and 9.6 for the stiff soil profile. The axes are of equal magnitude to make it easier to observe differences in response along the tower. Almost identical displacements are obtained for the bottom nodes, whereas increasing deviations between the models occur for higher points. It is mainly differences in the amplitudes, whereas the *dynamic* is correctly represented by the spring model as it displays the same oscillation tendency. The largest deviation occur in the top node where the peak displacement is overestimated by 39%. This deviation can be a consequence of the different nacelle representations, where the shell model has a distributed mass, whereas the spring model has a lumped point mass.

Larger deviations were expected for the accelerations since this quantity is highly sensitive to the displacement history. The largest accelerations occur in the middle section due to the dominating higher modes oscillations illustrated in figure 9.8a. This property is also demonstrated by the spring model, but underestimates the peak acceleration with 45% in the upper node.

The maximum moments and shear forces shown in figure 9.5 and 9.6 occur in the base of the wind turbine, but also the middle section experiences large loads of 5MNm and 200kN respec-

tively. It is recommended that also the middle section is carefully considered in the seismic design of high wind turbines and similar tall and slender structures. Again, the spring model underestimates important design responses.

This is a disadvantageous property of the spring model and must be corrected to provide conservative results. This property can be due to the applied Timoshenko shear flexible beam. Further work may suggest to use the Euler-Bernoulli beam element which are better suited for dynamic vibration with distributed inertia forces [1].

Figure 9.7 shows the accuracy of the displacements and rotations of the bottom node compared to the reference model for the stiff soil. The displacements are satisfactorily represented, whereas the spring model underestimates the rotation during the earthquake and overestimates it in the free-vibration phase. The reason for the large rotational deviations is assumed to be the frequency independent springs. Also the missing representation of the cross-term in the stiffness matrix and the beam properties are sources of errors. Even though large differences are observed in the rotational term, the rotations are very small (scale $1 \cdot 10^5$) compared to the dominating translational excitation. A simulation with and without the rotational term showed that the rotational term was insignificant to the overall response. The result can be found in figure D.9 and D.10 in the appendix.

Figure 9.8 shows typical deformation profiles for the soil and tower for the stiff and soft soil profile, while figure 9.9 gives a closer view of the foundation rotations. It is evident that the softer soil undergoes larger rotations than the stiff soil. Further, figure 9.8b shows how the weaker upper layer elongates the period of the seismic waves. The presence of weaker materials does also elongate the systems natural equivalent period expressed as

$$T_{eq}^2 = T_0^2 + T_h^2 + T_r^2 \quad (9.1)$$

$$T_h = 2\pi \sqrt{\frac{m_{tower}}{k_{HH}}} \quad (9.2)$$

$$T_r = 2\pi \sqrt{\frac{I_r}{k_{MM}}} \quad (9.3)$$

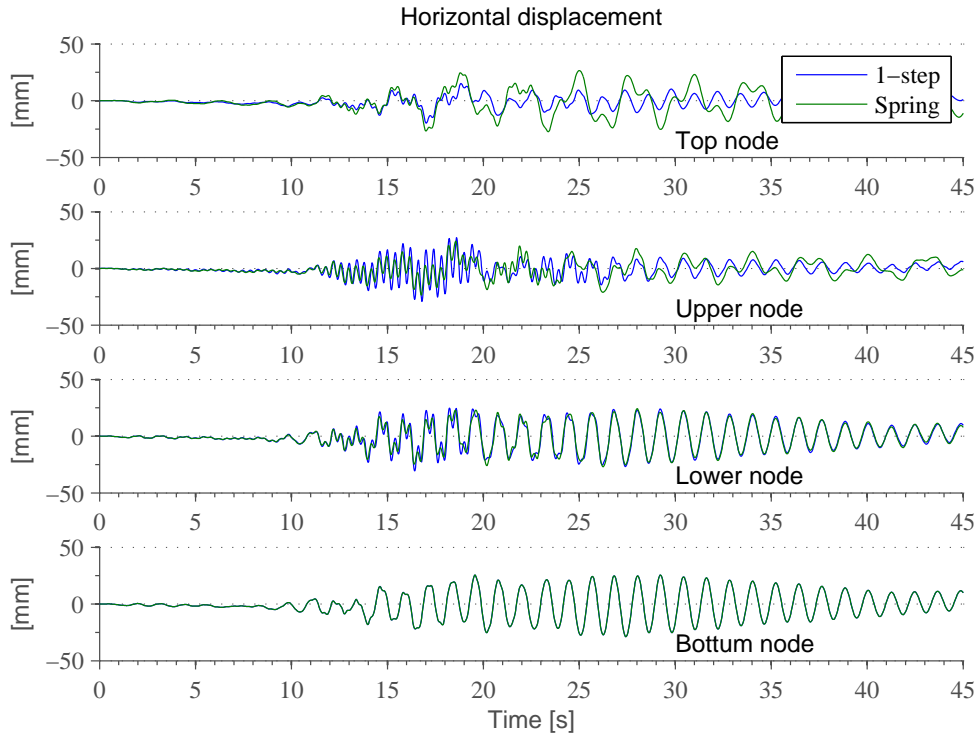


Figure 9.3: Horizontal time history displacement for the fully integrated model the a spring model for the stiff soil condition.

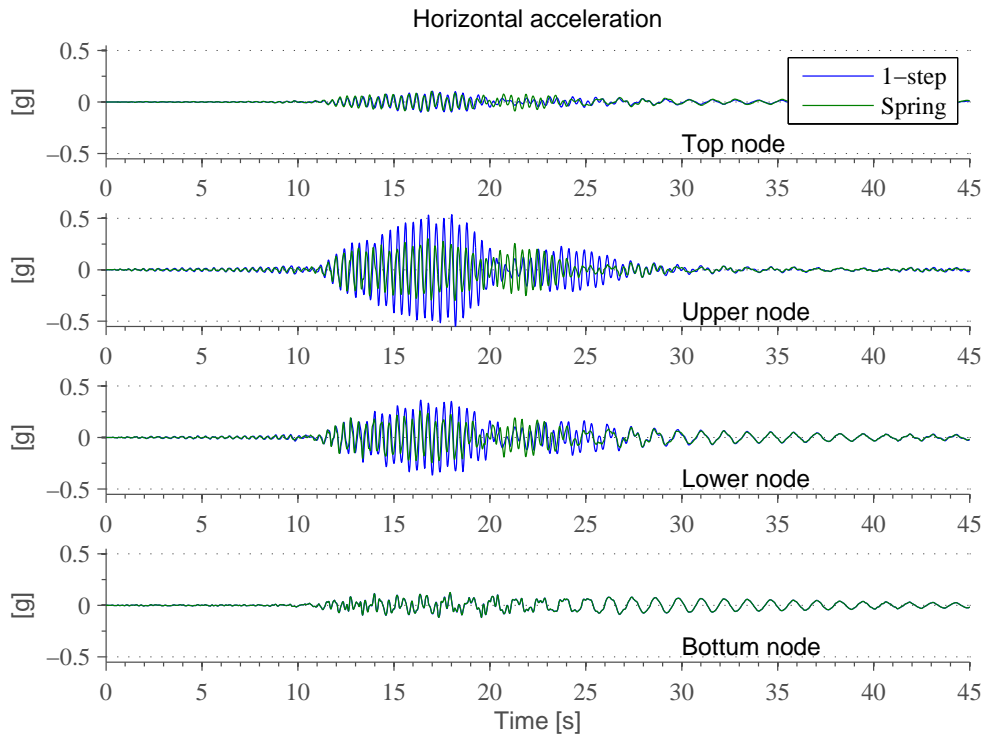


Figure 9.4: Acceleration along the tower for the fully integrated model and the spring model for the stiff soil condition.

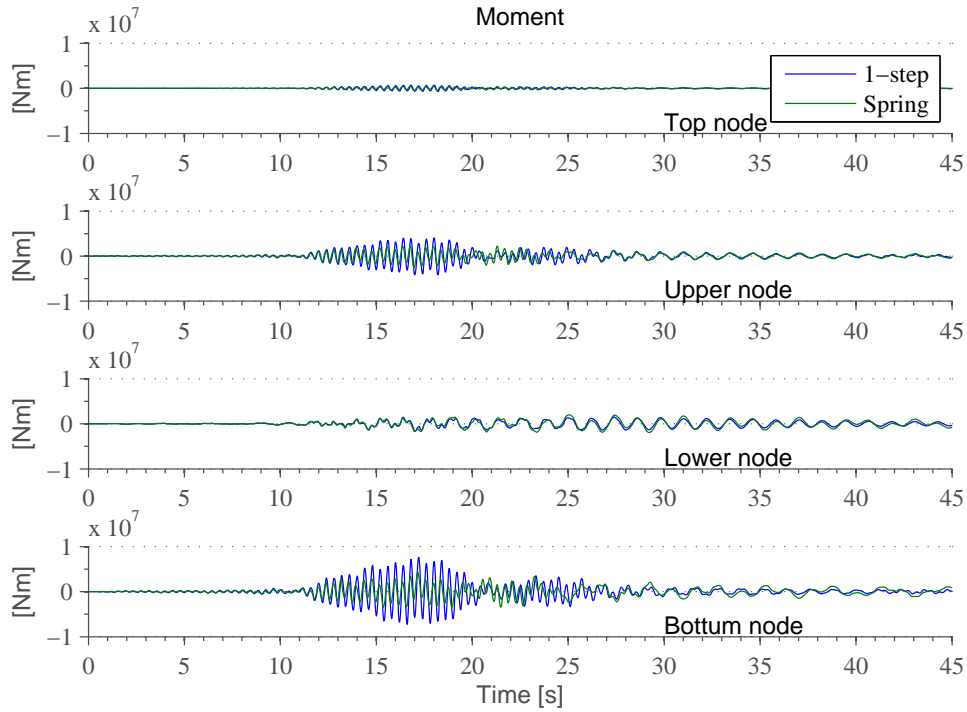


Figure 9.5: Moment along the tower for the full model and the spring model for the stiff soil condition.

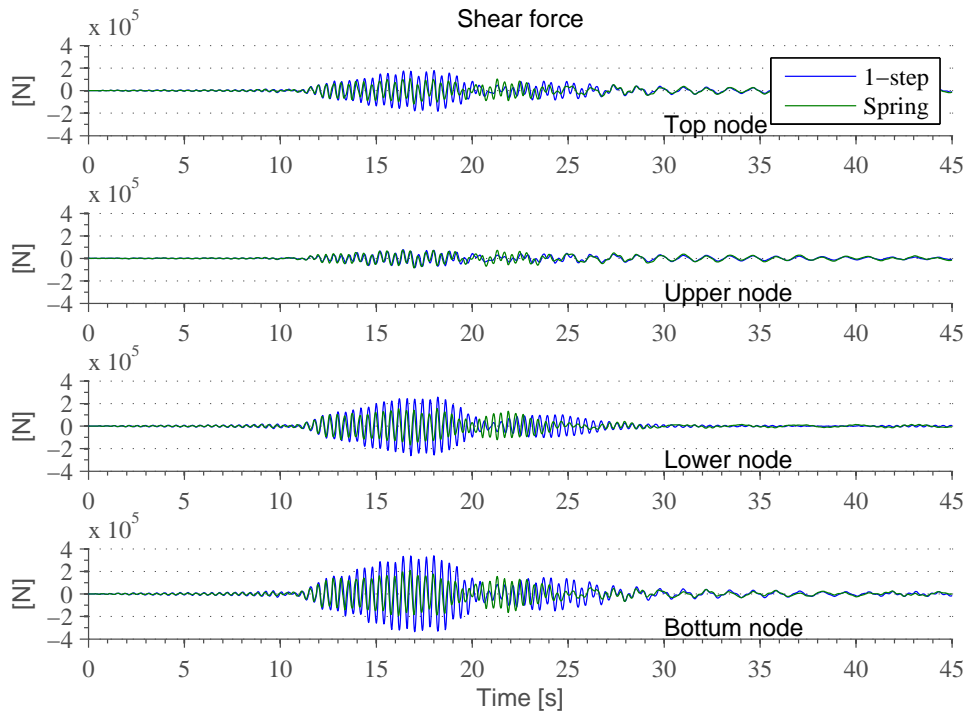


Figure 9.6: Shear forces along the tower for the fully integrated model and the spring model for the stiff soil condition.

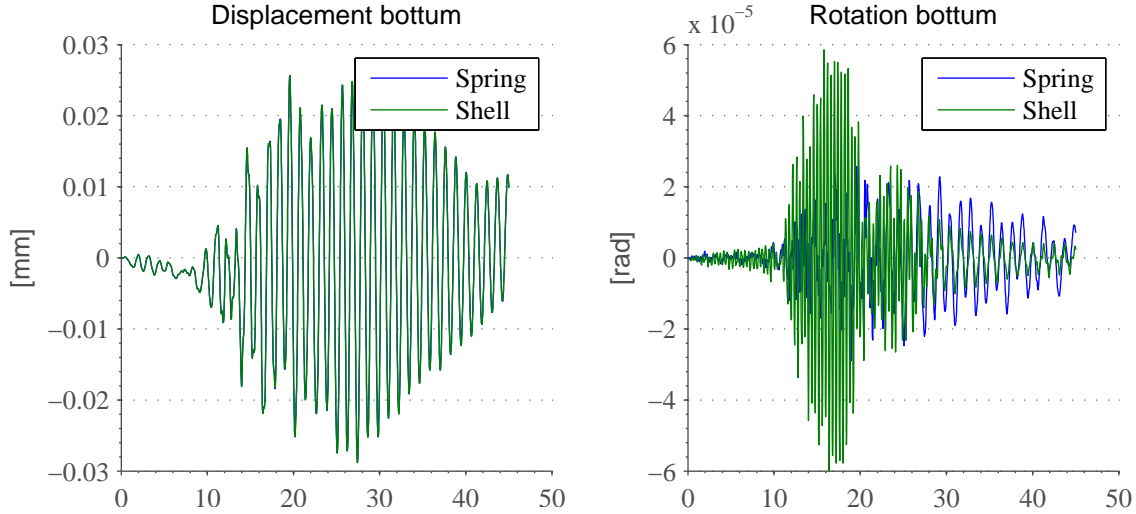


Figure 9.7: Accuracy of the spring model bottom displacement and rotation compared to the reference shell model.

where T_0 is the period of the fixed-base wind turbine, T_h is the swaying period, T_r is the rocking period of the skirted foundation and I_r is the mass inertia of the tower. Wind turbines have large fundamental periods compared to the foundation/soil system. The wind turbine has a fixed base period of $T_0 = \frac{1}{0.325\text{Hz}} = 3.1\text{s}$, while the skirted foundation has periods of $T_H = 2\pi\sqrt{\frac{267 \cdot 10^3 \text{kg}}{3.33 \cdot 10^9 \text{N/m}}} = 0.06\text{s}$ and $T_R = 2\pi\sqrt{\frac{3.81 \cdot 10^9}{1.83 \cdot 10^{11}}} = 0.91\text{s}$ for the stiff soil profile.

Since the wind turbine tower is very soft compared to the soil/foundation system, changes in the soil materials will not influence the equivalent period significantly. The period elongation brings the fundamental mode of the wind turbine further away from the frequency content at the soil surface for an typical earthquake. For a wind turbine of this size, it is seen that higher modes dominate the seismic response along the tower. In general, attention should be given to systems where the natural periods of the soil and the equivalent system are close. For such cases, amplification of the input motion at the base can be severe.

Figure 9.10 shows the inertial disturbance for the stiff and soft soil. The inertial disturbance is measured as changes in the spring input due to inertia forces at the bottom. It is seen that the *translational* spring input is insignificantly influenced by the inertial interaction for the stiff soil, whereas the *rotational* input is influenced due to the large base moments. On the other hand, it is seen that inertial effects influence both swaying and rocking for the soft soil. For cases where the inertial contribution is expected to be of importance for the total response, the

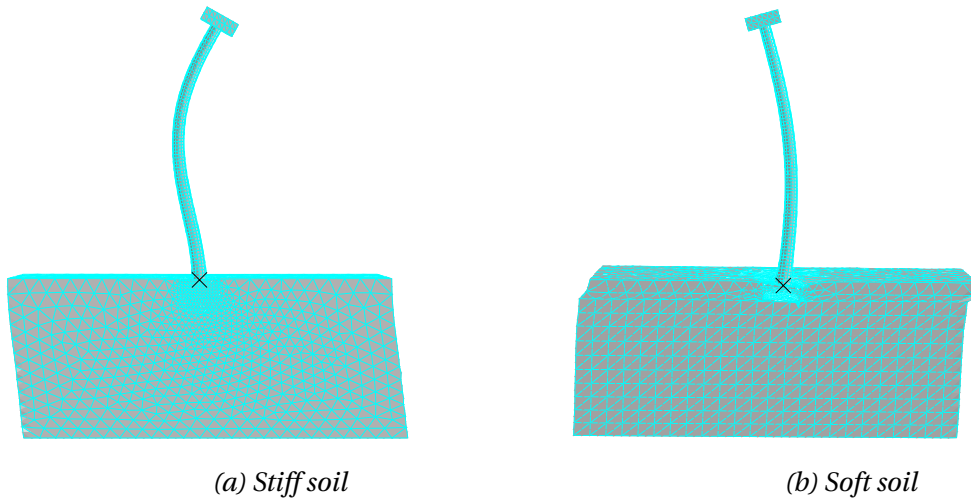


Figure 9.8: Deformation profiles during seismic excitation for the two soil deposits.

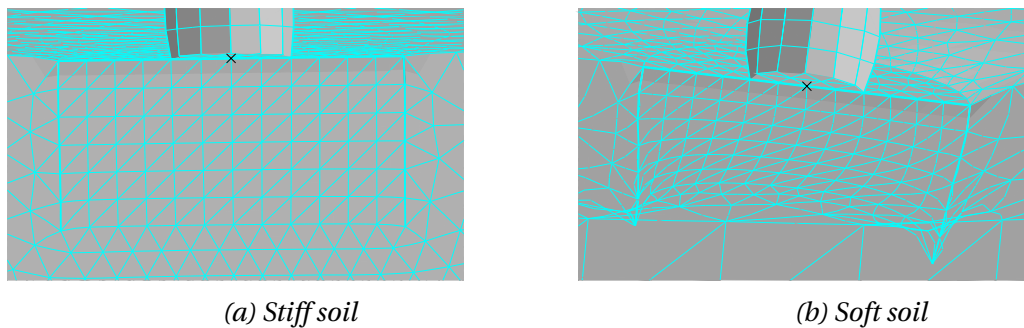


Figure 9.9: Close up of the skirted foundation during seismic excitation for the two soil deposits.

spring properties should also be carefully determined.

The seismic response along the tower for the two soil profiles is given in figure 9.11, 9.12, 9.13 and 9.14. The same excitation is applied at the bedrock to illustrate how different soil properties influence the seismic response along the tower. It is seen that the response is highly dependent on the underlying soil properties. This observation emphasizes the importance of correct site response analyses.

In addition, a comparison between the seismic response for the full model and the spring model is given in figure D.3, D.4, D.5 and D.6 in the appendix for the soft soil profile. In this case the displacements and accelerations deviates more, whereas accurate shear forces and moments are obtained. The reason for the better match regarding the loads for the soft soil compared to the stiff soil is unknown.

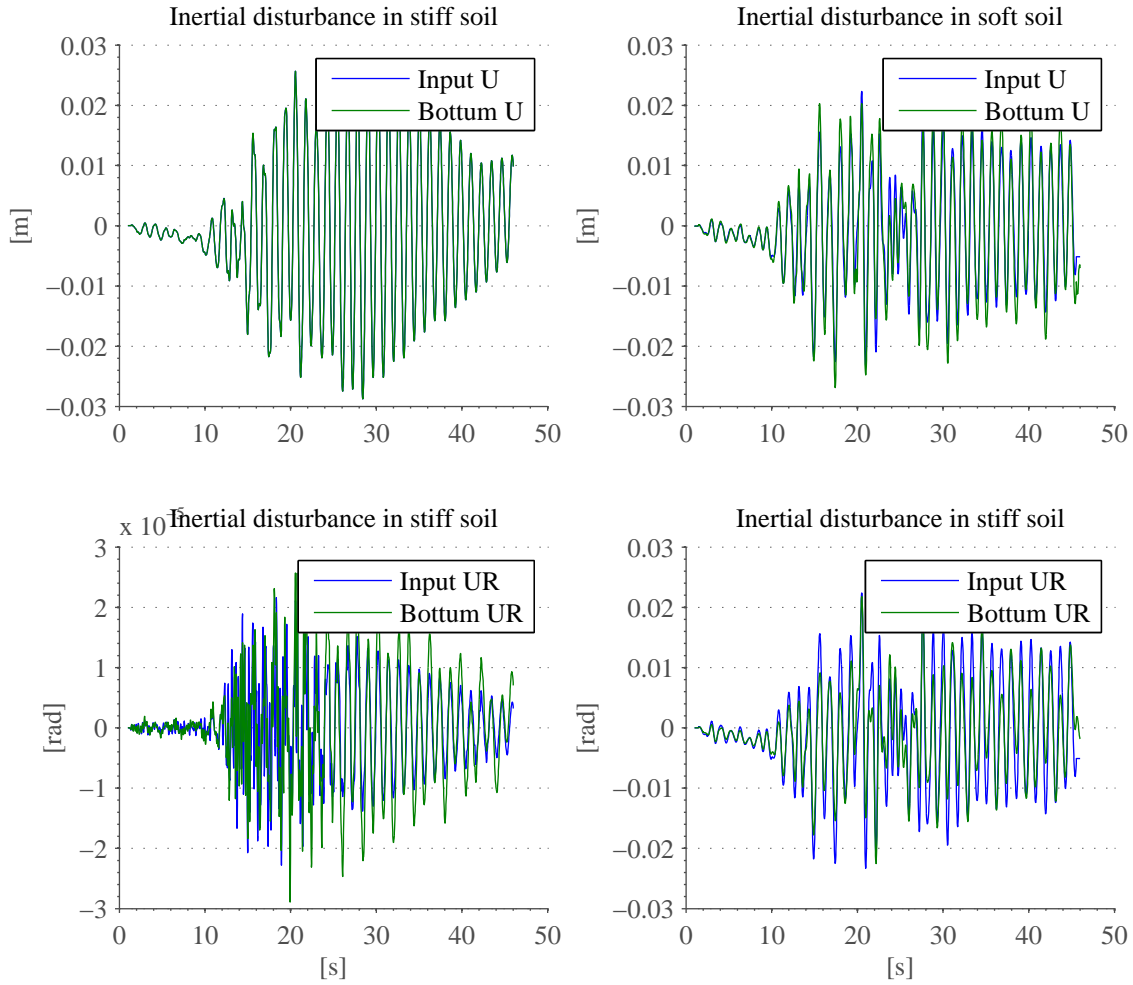


Figure 9.10: Comparison of the spring input translation and rotation against the bottom beam node. The graphs shows the inertial interaction for the two soil profiles.

Figure 9.15, 9.16, 9.17 and 9.18 show the flexible-base response and the fixed-base response for the stiff soil profile where the models are provided with the same base input. In the fixed-base configuration the seismic excitation at the surface is applied directly at the bottom node. It is seen that the inertial effects on the bottom node reduces the moments and the shear forces in the tower, whereas the displacements are expected to increase due to the flexible base. The latter is not very visible at the graph, but is expected to increase with softer soil.

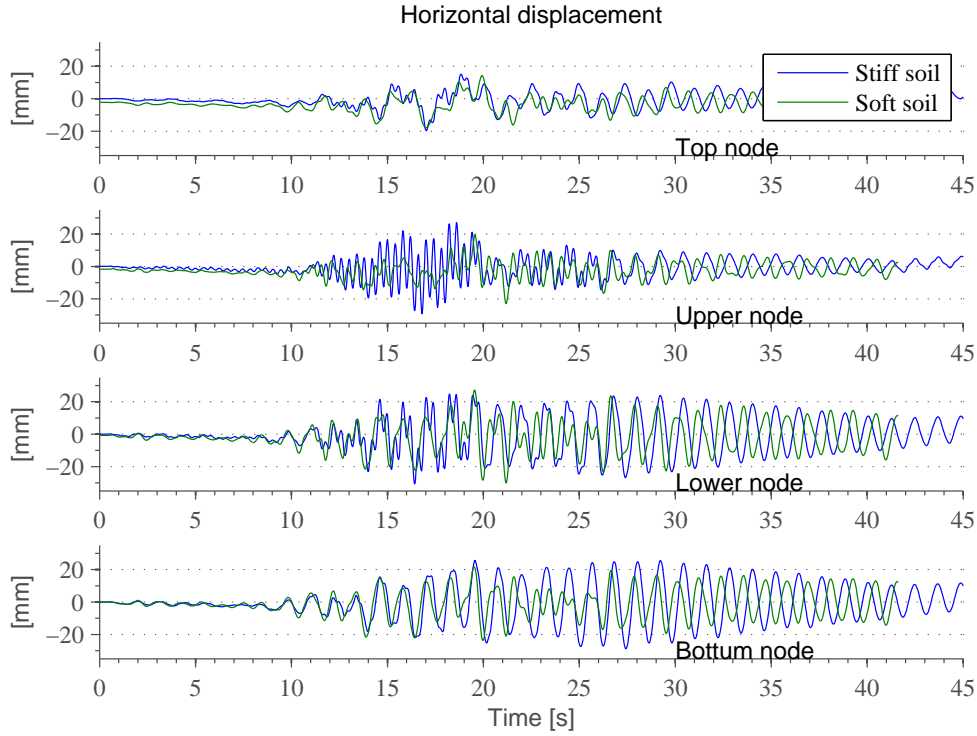


Figure 9.11: Displacements for a stiff and a soft soil; (1) a homogeneous soil with $V_S = 200 \frac{m}{s}$ and (2) a three-layered soil with $V_S = 50 \frac{m}{s}$ for the weakest upper layer.

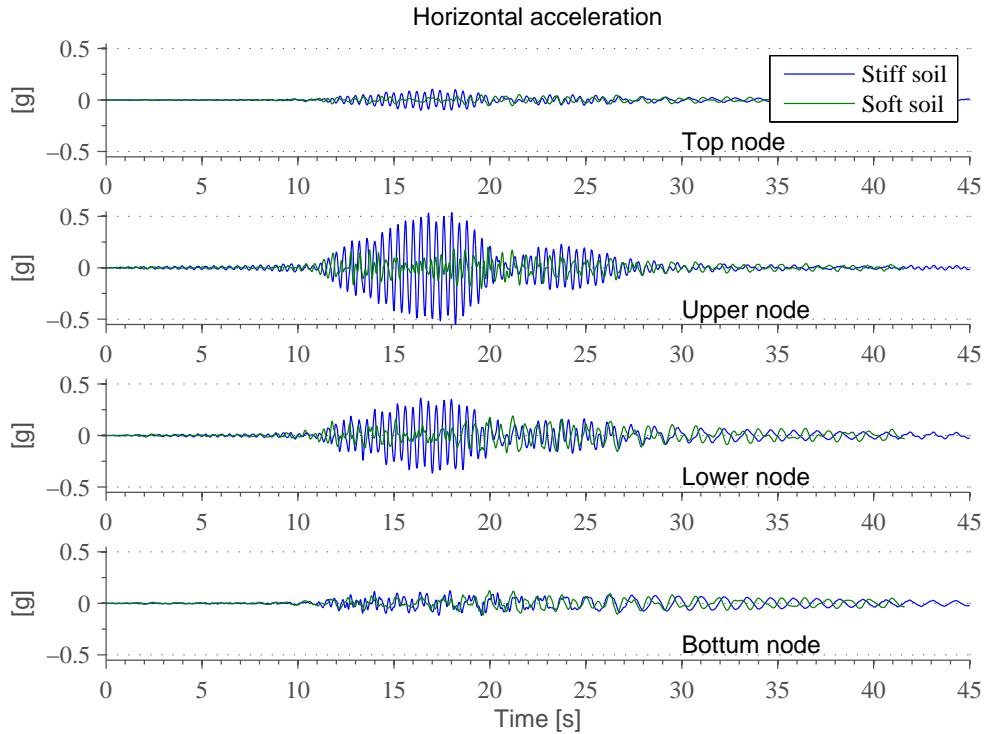


Figure 9.12: Accelerations for a stiff and a soft soil; (1) a homogeneous soil with $V_S = 200 \frac{m}{s}$ and (2) a three-layered soil with $V_S = 50 \frac{m}{s}$ for the weakest upper layer.

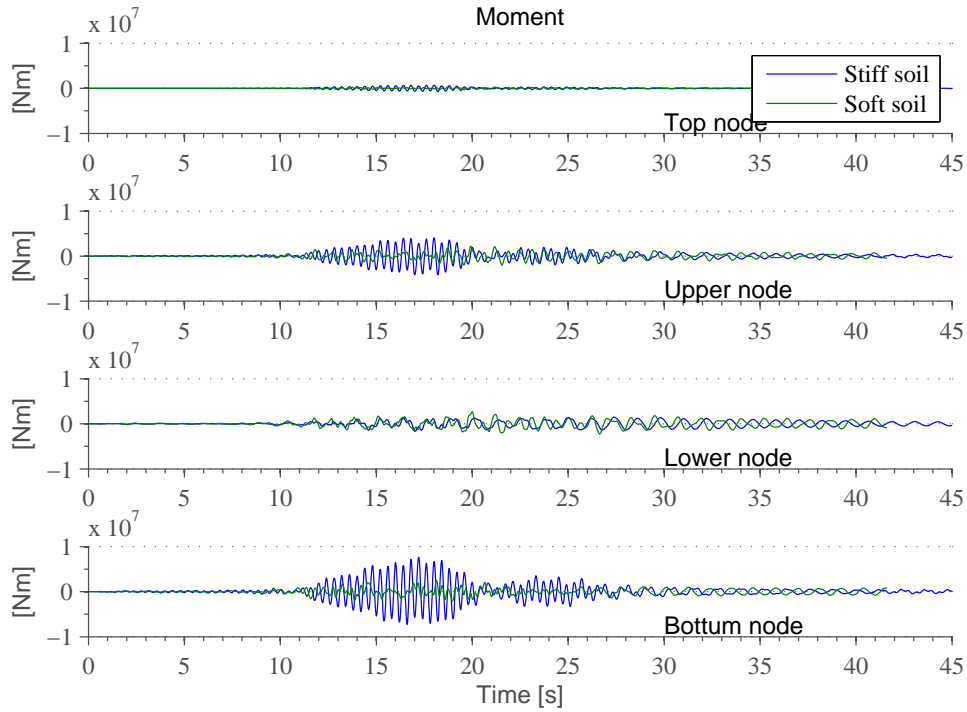


Figure 9.13: Moments for a stiff and a soft soil; (1) a homogeneous soil with $V_S = 200 \frac{m}{s}$ and (2) a three-layered soil with $V_S = 50 \frac{m}{s}$ for the weakest upper layer.

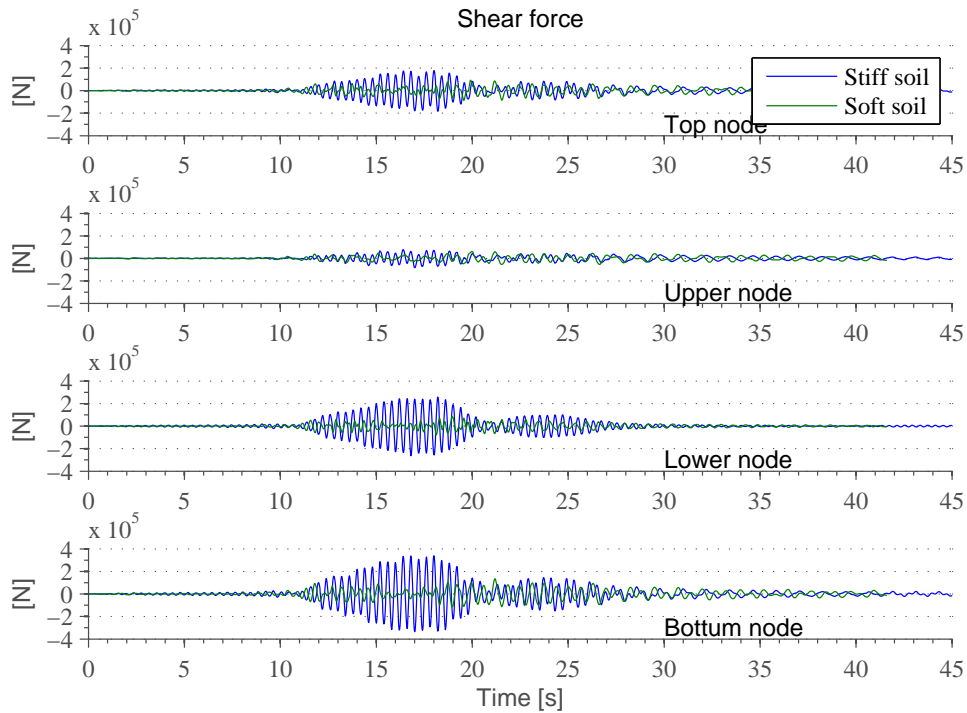


Figure 9.14: Shear forces for a stiff and a soft soil; (1) a homogeneous soil with $V_S = 200 \frac{m}{s}$ and (2) a three-layered soil with $V_S = 50 \frac{m}{s}$ for the weakest upper layer.

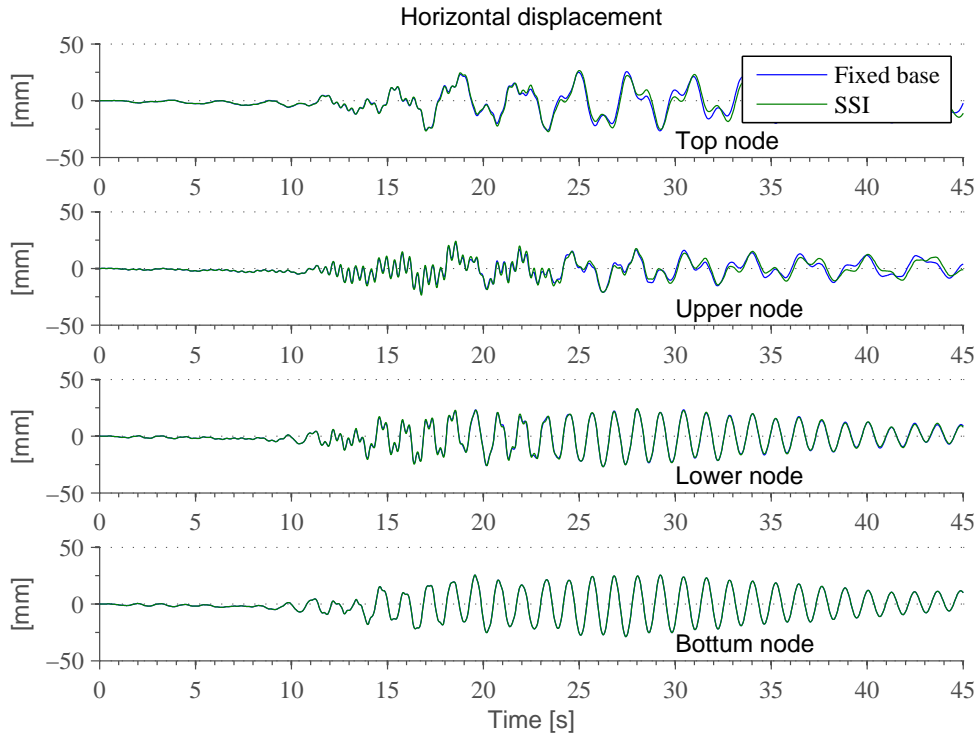


Figure 9.15: Displacements for (a) a fixed base and (b) a flexible base for the stiff soil condition.

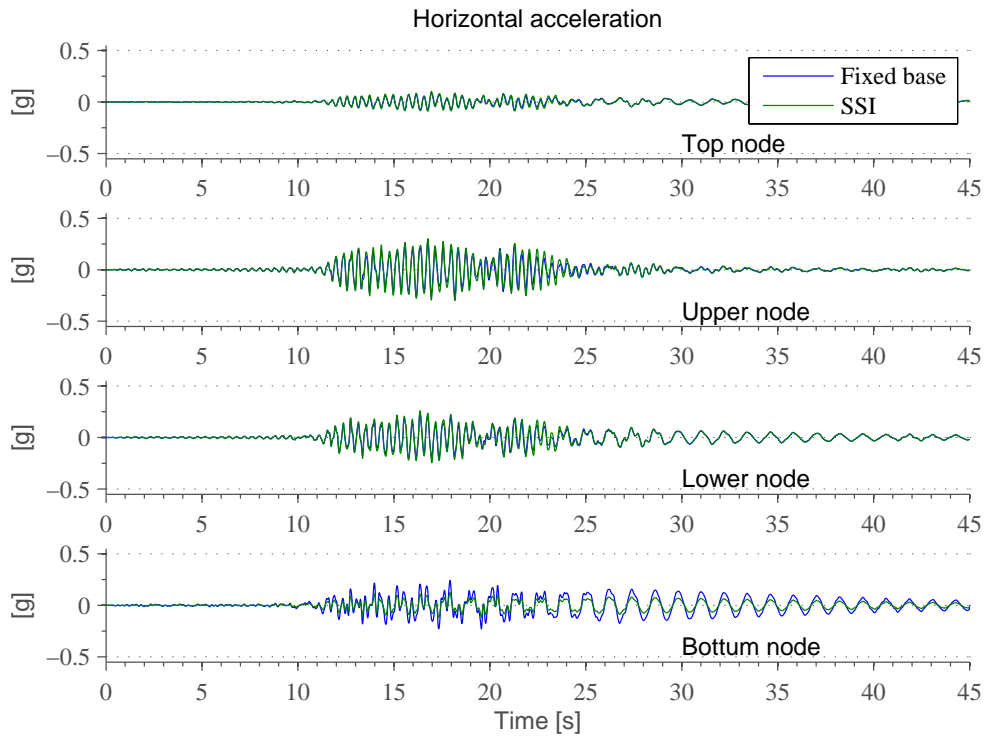


Figure 9.16: Accelerations for (a) a fixed base and (b) a flexible base for the stiff soil condition.

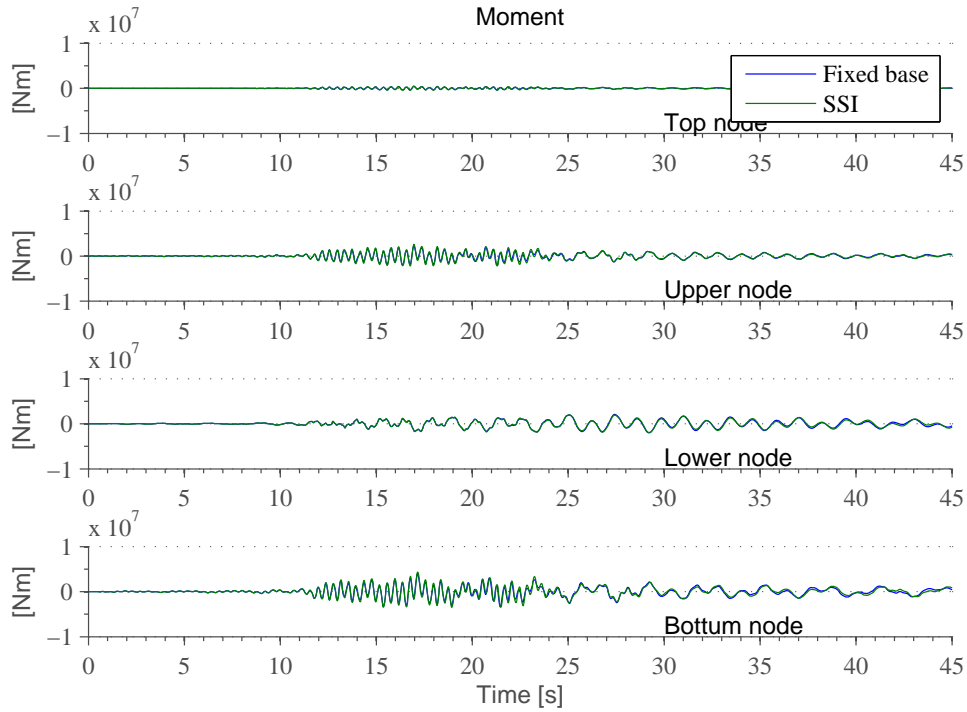


Figure 9.17: Moments for (a) a fixed base and (b) a flexible base for the stiff soil condition.

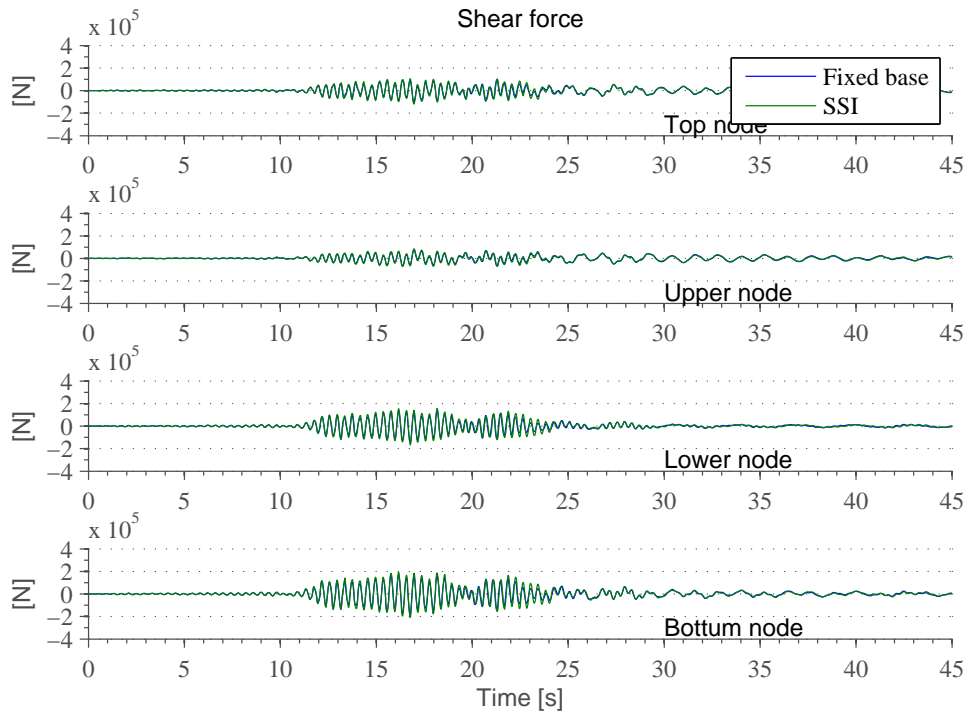


Figure 9.18: Shear forces for (a) a fixed base and (b) a flexible base for the stiff soil condition.

9.2 Part B: Parametric Study

Part B focuses on the inertial interaction between the soil/foundation and the wind turbine, whereas part A investigated the accuracy of the spring model and carried out a site response analysis for two soil profiles. Now, the same base excitation is applied in all simulations. The aim of the parametric study is to examine how changes in the foundation geometry influence the distribution of peak displacement, accelerations, moments and shear forces along the tower. In addition, the tower's height is varied to study changes in base demand.

The kinematic spring excitation corresponds to the stiff soil profile in part A and is used in all simulations. Only the horizontal part is included. The soil has material properties $E = 50\text{MPa}$ and $V_s = 100\frac{m}{s}$ which is within the range the theoretical stiffness formulas can be accurately applied. This give a first natural period of $T_1 = 2.4\text{s}$ for a soil depth of $H = 60\text{m}$.

9.2.1 Geometry of the skirted foundation

It is important to investigate the distribution of maximal responses along the tower such that sufficient seismic design can be provided for all tower sections. The tower's dynamic behaviour depends on the spring properties applied to the base since these influence the seismic deformation pattern along the tower. The stiffnesses can be varied in two ways; either by changing the foundation radius or depth. This parametric study consider both possibilities.

Both the foundation radius and depth is varied in the range $D, R \in [4\text{m}, 8\text{m}]$ with $D = R = 6\text{m}$ being the reference geometry represented by the coincident points in figure 9.19. The figure shows the swaying and rocking stiffnesses as a function of radius (depth is kept constant) and depth (radius is kept constant). It is seen that changes in radius influence the foundation stiffnesses more than the depth. The static spring stiffnesses applied in the parametric study are given in table D.1 and table D.2 in the appendix.

Figure 9.20 and 9.21 show the peak displacements, accelerations, shear forces and moments distribution along the tower for different foundation geometries. Each point corresponds to a seismic simulation where maximum responses are collected. The fixed-base solution is given

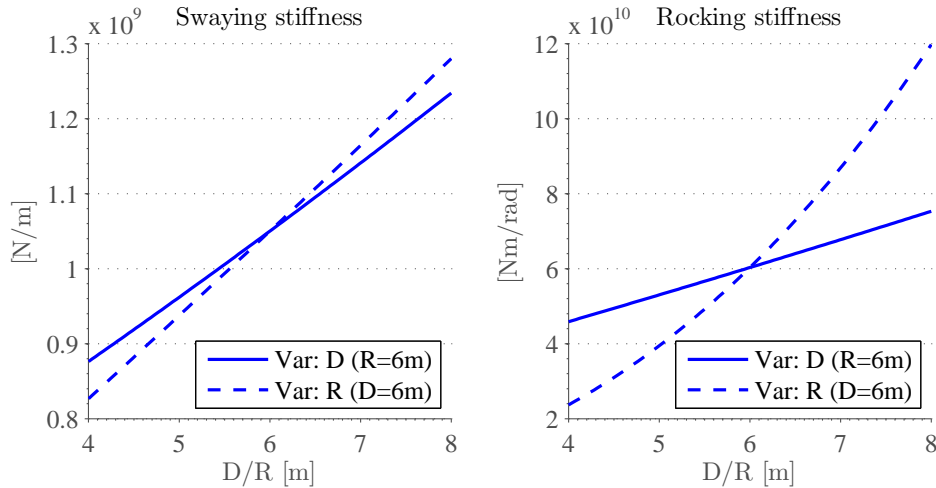


Figure 9.19: Swaying and rocking static stiffnesses for different bucket depths and radius.

by the solid line and reflects the configuration where the seismic excitation is applied directly at the rigid tower base. It is seen that the responses converge toward the fixed base solution for large geometries. A general observation is that all responses increase as the foundation gets smaller. In other words, a softer system gives larger responses for this slender wind turbine.

It is seen that changes in radius influence the peak responses to a larger extent than the depth. This observation is consistent with the expected results, since the radius is more important to the rocking stiffness.

The displacement and acceleration in the bottom node for the flexible base configurations are not influenced by changes in radius nor depth. The reason why the fixed-base configuration shows a different acceleration in the bottom node is due to the lacking dashpot. The inertia forces are not large enough to create significant deviations in the swaying motion for the different geometries.

On the other hand, the dominating rocking mode of the tower creates different rotations at the base for all of the foundation geometries. This is seen by the increasing deviation between the different foundation geometries.

Different base conditions influence the excited mode shapes in the tower. By visual observation of the seismic behaviour for each case in *ABAQUS*, it is seen that the base conditions influ-

ence the deformation pattern and the accelerations along the tower. Of course, this will further influence the distribution and magnitude of the inertia forces. This is why a softer system still can achieve larger moments and shear forces as seen in figure 9.20.

The relative distribution of peak responses along the tower is maintained in all cases, except for $R = 4m$. For this geometry, a very low rocking stiffness is obtained which in turn creates significant rotations at the base. This is why the maximum displacement occurs in the middle section for this case, whereas the base has the highest displacements for the other cases.

It is seen from the acceleration plots that higher modes are excited for all geometries for the 80m high wind turbine. As a consequence, the acceleration in the nacelle does not get amplified, but stands rather still. For smaller wind turbines, as Nordtank in chapter 6, the seismic response was dominated by the first bending mode. This demonstrates that higher modes are of upper importance for the seismic response for tall wind turbines.

The largest moments and shear forces occur at the base for all geometries, but it is seen that also the middle sections experience severe forces and moments. This results may suggest that also the middle section of a wind turbine should be carefully design for seismic demand.

A comparison between figure 9.20 and 9.21 shows that lower amplitudes are obtained in the latter. Note that an decrease in foundation depth from $D = 6m$ to $D = 4m$ does not cause the displacement to change localization along the tower as is the case for the radius. The graphs concludes that the dynamic behaviour of the tower is indeed more sensitive to changes in the foundation radius than depth.

Since the base experiences the highest moments and shear forces, these results are normalized in figure 9.22 with respect to the results obtained for the reference geometry. Since the nacelle contains sensitive equipment, displacements and acceleration are given for the top node. The horizontal foundation stiffness is taken as the x-axis with $k_{HH,ref}$ being the reference stiffness. It is seen that a 20% decrease in horizontal stiffness gives 120% increase in nacelle acceleration, 80% increase in base moment and 110% increase in base shear if the radius is changed. If the depth is changed, the tower will experience approximately 25% increase in nacelle acceleration, 20% increase in base moment and 30% increase in base shear.

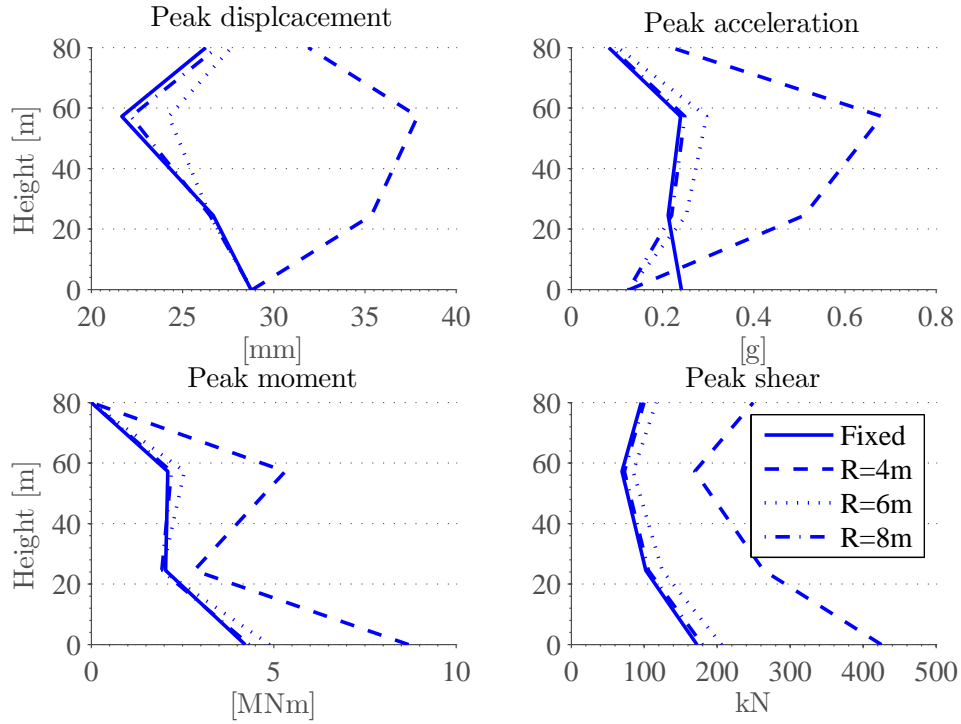


Figure 9.20: Changes in peak response quantities along the tower as a function of foundation radius R . The same spring input motion is applied in all cases.

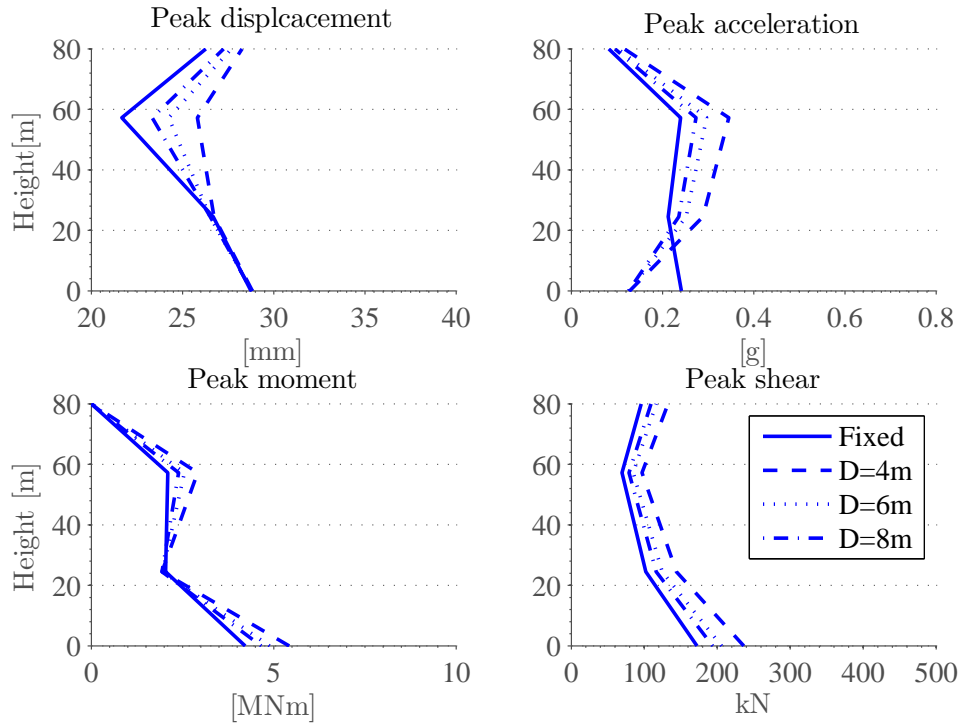


Figure 9.21: Changes in peak response quantities along the tower as a function of foundation depth D . The same spring input motion is applied in all cases.

The foundation are assumed bounded to the soil in the numerical models. In reality, gaps and weaker soil materials will be present at the interface which in turn will reduce the stiffnesses. The result from section 8.1.2 can be used with figure 9.22 to estimate changes in peak responses due to weaker soil materials in the foundation/soil contact zone.

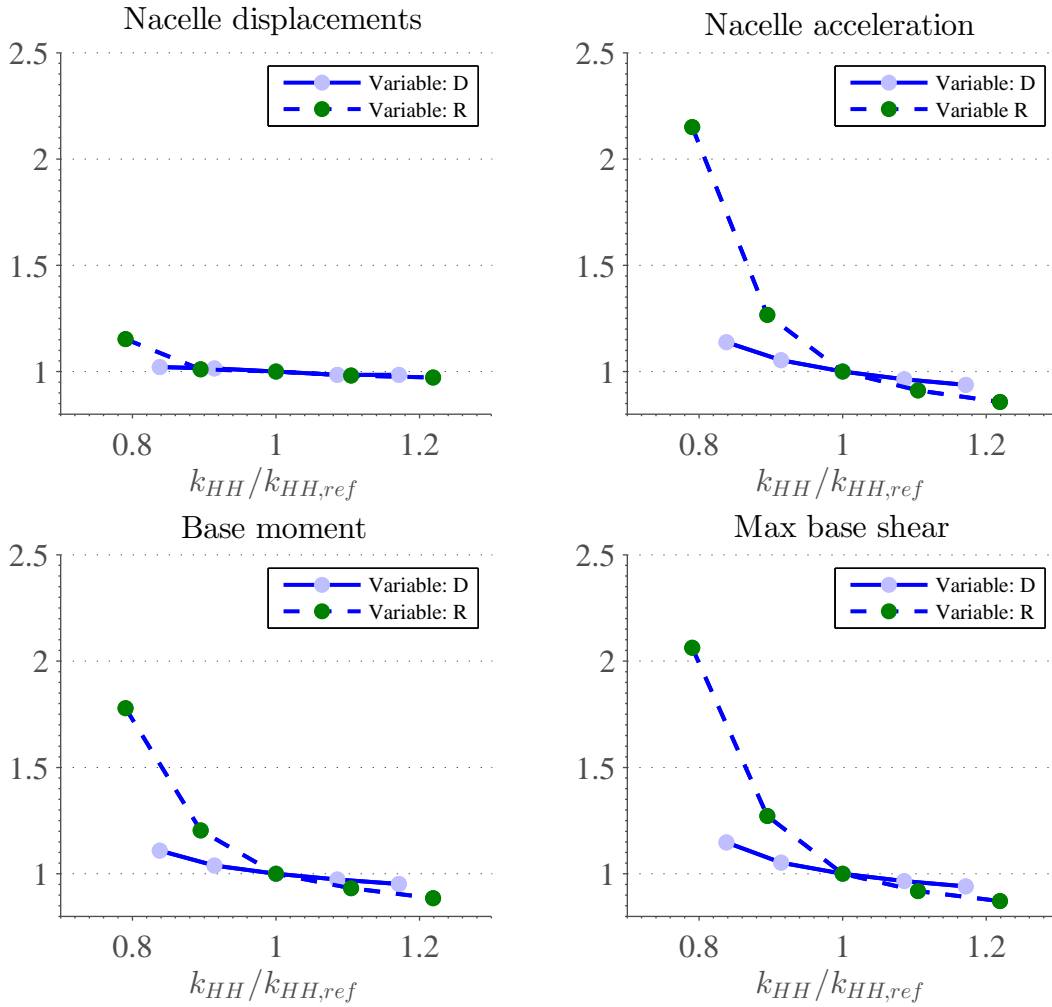


Figure 9.22: Change in peak responses as a function of a geometric foundation changes relative to the reference geometry ($D = R = 6m$). The variables D and R are independently varied.

9.2.2 Response for different tower heights

A larger amount of masses is subjected to seismic excitation when the tower's height increases. It is intuitive to think that an increase in tower mass in combination with a larger force arm

creates larger base moments during seismic excitation, which is demonstrated to not be true. In this sections it is investigated how changes in tower heights influence the seismic response.

The tower heights considered are $H = 75m, 80m, 85m$ and $100m$. All heights are assigned a homogenous cross section with diameter $D = 3.67m$ for simplicity and attached to the reference foundation. The diameter corresponds to the mean diameter in the reference wind turbine. Further, the reference foundation geometry is used in all simulations.

Figure 9.23 shows the peak responses as a function of changes in tower height. A general observation for all quantities is that they tend to increase or decrease up to certain heights, and thereafter the tendency turns. The time history plots for each point is provided in figure D.23, D.24, D.25 and D.26 in the appendix. It is seen that each height has its own oscillation characteristic.

For the height $H = 85m$, the combination of the seismic load frequencies and the tower's eigenmodes is demonstrated to be very disadvantageous since it results in a significant increase in peak responses along the tower. As much as 760% increase in nacelle acceleration, 150% increase in base moment and 265% increase in base shear is obtained for this particular combination of foundation geometry, load frequencies and tower height. Figure 9.23 further demonstrates that the peak responses will decrease for a certain (but unknown) height after $H = 85m$.

9.2.3 Period elongation

In addition, a period elongation analysis is carried out to study the change in natural frequency between a flexible base configuration and its corresponding fixed base configuration. The period elongation is measured as the ratio between the tower's flexible base natural frequency and its corresponding fixed base frequency. Figure 9.24 shows the period elongation for *a*) changes in foundation geometry (or equivalent stiffness) and *b*) changes in the tower height. The period elongation is plotted as a function of tower/foundation-stiffness ratio.

It is seen that an increase in tower stiffness compared to the foundation results in a softer system and that the deviation between the fixed-base configuration and flexible-base configuration increases with decreasing foundation stiffness. Although period elongation is not very important

to the tall and slender wind turbines due to their already high periods, it can influence the seismic response of smaller and more compact structures as it can bring the structures fundamental frequency closer to the load frequencies. In a typical wind turbine, the excitation frequencies and the fundamental frequency are already well separated.

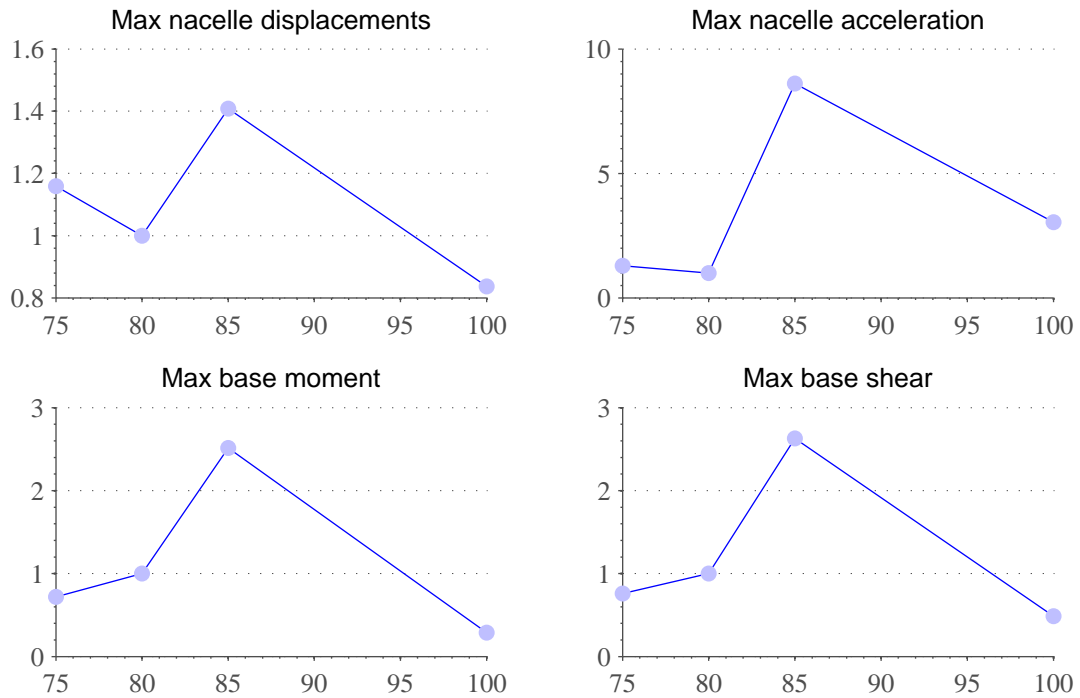


Figure 9.23: Maximum responses for varying tower height.

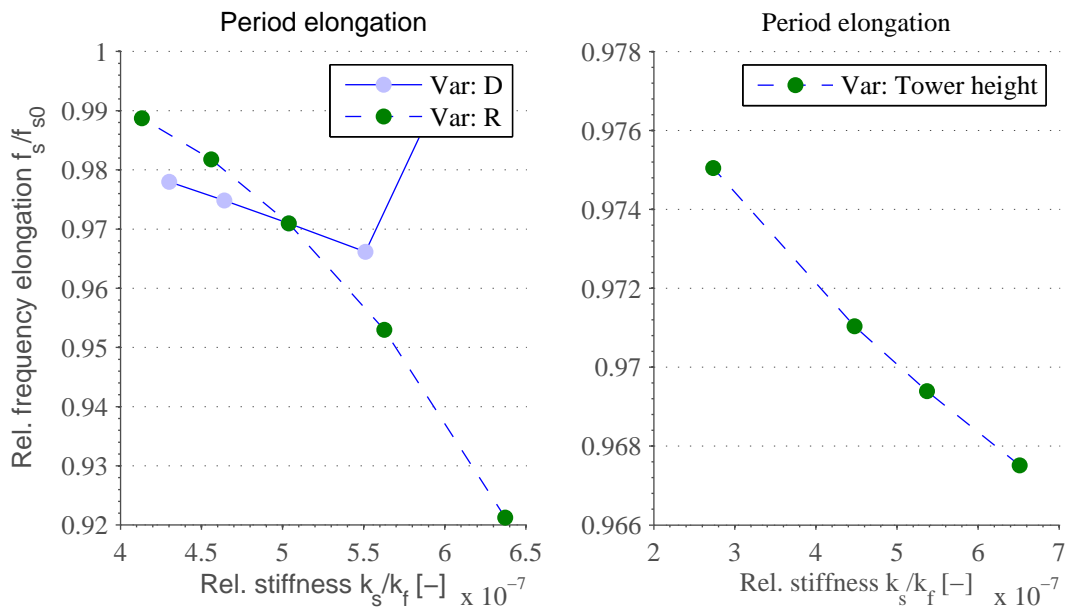


Figure 9.24: Natural frequency elongation as a function of tower/foundation stiffness ratio. The first graph studies changes in bucket geometry and the second studies changes in tower height.

Chapter 10

Conclusions & Further Work

This thesis focused on the global seismic response of a parked wind turbine installed at a skirted foundation. The fully integrated model and the simplified spring model demonstrated to be capable of simulating the seismic behaviour of a wind turbine tower accounting for SSI-effects; even with the relatively simple modeling techniques used. The models are restricted to the linearly elastic range and assume that the foundation is fully bounded to the soil during seismic excitation. The latter implies that the computed stiffnesses represent an upper limit since gaps and sliding occur in real-life structures.

Several simulations were performed on the fully integrated model and the spring model to answer the stated problem definitions. The following conclusions were made:

1. The simple spring model underestimates important design parameters along the tower, such as emerging shear forces and moments. Improvements must be made to make the spring approach more reliable regarding simulation of real-life structures.
2. The free-field translation can replace the kinematic translation without significant changes in the response arising. Due to the relatively small foundation geometry compared to the propagating wave lengths, the foundation can easily adjust to the free-field motion and hence the effect of kinematic interaction can be neglected.
3. Higher order mode shapes were shown to contribute significantly to the seismic response

for wind turbine heights in the range considered. This result shows the importance of preventive seismic design for all tower sections.

4. Tall and slender structures cannot uncritically be simplified as rigid-base structures since the inertial effects can be tremendous to the seismic response. Effects of SSI are shown to be both advantageous and disadvantageous and must hence be investigated for each case of interest.
5. For the stiff and soft soil profile it was shown that SSI reduced the shear forces and moments along the tower compared to the flexible-base solution. The soft soil deviated the most from the fixed-base solutions and showed a reduction of 53% and 63% for the peak shear and moment at the base when SSI was included. In other words, SSI *can* have a beneficial effect on the structural response.
6. A contrary conclusion was made for the parametric study which investigated changes in peak responses for different foundation geometries. It was shown that flexible bases is disadvantageous to the seismic response in terms of increasing shear forces, moments, displacements and accelerations for the particular foundation geometries and soil properties studied.

The inertial forces along the tower creates significant bending moments around the tower base. The flexible base causes the tower base to rotate, which further influence the deformation pattern and acceleration in the tower. It is demonstrated that the inertial contribution can be of strongest importance in the seismic response. In addition, it was shown that the base was subjected to the highest shear forces and moments in all the investigated cases.

7. The foundation radius is the most important design parameter regarding rocking stiffness. This fact in combination with the dominating rocking mode of the wind turbine makes the seismic response more dependent on the foundation radius than on the foundation depth.
8. Lastly, it was shown that particular combinations of tower heights, excitation frequency and foundation stiffnesses could lead to large amplification of the responses along the

tower. Careful consideration must be taken when the natural frequencies of the soil are close to the natural frequencies of the combined structure and foundation.

Further Work

The models established in this thesis involve several assumptions and simplifications. An extension into the non-linear range for both soil and structure would add an extra dimension to the results. Constant radiation damping for all foundation geometries and frequency independent springs represent both considerable simplifications and could be modified for future work.

The following suggestions for future work are proposed:

1. Establish a more complex spring model which accounts for non-linearities as well as frequency dependent spring properties.
2. Repeat the parametric study for a different soil material because the choice of soil material influences the excitation at the soil surface.
3. Study the recommendations given in current design guidelines regarding seismic response of structures and compare it to the numerical results.

Appendix A

MatLAB Scripts

A.1 Theoretical Amplification Function

The following script produces the amplification function between the surface and the bedrock for a homogeneous soil.

```
% DESCRIPTION: This script calculates and plots the theoretical transform
% function H(w) soil subjected to harmonic basemotion.
%
% SYMBOLS:
% H=          height of soil-layer      [m]
% Vs=         shear wave velocity      [m/s]
% xi=         damping coefficients      [-]
% f=          frequency                 [Hz]
% z=          vertical axis             [m]
% n=         number of computed eigenfrequencies and eigenmodes
%
% INPUT:
% [Vs,H,xi,w]
%
% OUTPUT:
% Mode shapes and analytic solution of the displacement amplification
```



```

% factor for a soil layer
%
% Written by Jeanett Rorvig, January 2014
% Master Thesis on Wind Turbines

close all
clear all
clc

Vs=[300 500 700];
H=50;
xi=[0.02 0.05 0.10];
w=linspace(0,94,300);
f=linspace(0,15,300);
z=linspace(0,40,200);
%% Mode shapes for Vs=300

Rd_nodmp=abs(1./(cos(w*H/Vs(1))));

n=4; % number of wanted modeshapes
wn=zeros(1,n);
phi_nodmp=zeros(length(z),n);

g=figure(1);
for i=1:n
wn(i)=(2*i-1)/2*(pi*Vs(1)/H);
phi(:,i)=sin(wn(i).*z/Vs(1));
subplot(1,n,i)
plot(phi(:,i),z)
xlim([-1,1]);
ylabel('Soil depth z (m)')
PrettyPlotgca
end

%% Theoretical solution for three different damping coefficient

```

```
% Note that this solution has the same damping coefficient to all
% eigenfrequencies. If Rayleigh damping is used, the damping coefficient
% will vary over the frequency range.
```

```
Rd_dmp300=zeros(length(w),length(xi));
```

```
Rd_dmp500=zeros(length(w),length(xi));
```

```
Rd_dmp700=zeros(length(w),length(xi));
```

```
% Vs=300
```

```
Rd_dmp300(:,1)=1./sqrt(cos(w*H/Vs(1)).^2 + (xi(1)*w*H/Vs(1)).^2);
```

```
Rd_dmp300(:,2)=1./sqrt(cos(w*H/Vs(1)).^2 + (xi(2)*w*H/Vs(1)).^2);
```

```
Rd_dmp300(:,3)=1./sqrt(cos(w*H/Vs(1)).^2 + (xi(3)*w*H/Vs(1)).^2);
```

```
%Vs=500
```

```
Rd_dmp500(:,1)=1./sqrt(cos(w*H/Vs(2)).^2 + (xi(1)*w*H/Vs(2)).^2);
```

```
Rd_dmp500(:,2)=1./sqrt(cos(w*H/Vs(2)).^2 + (xi(2)*w*H/Vs(2)).^2);
```

```
Rd_dmp500(:,3)=1./sqrt(cos(w*H/Vs(2)).^2 + (xi(3)*w*H/Vs(2)).^2);
```

```
%Vs=700
```

```
Rd_dmp700(:,1)=1./sqrt(cos(w*H/Vs(3)).^2 + (xi(1)*w*H/Vs(3)).^2);
```

```
Rd_dmp700(:,2)=1./sqrt(cos(w*H/Vs(3)).^2 + (xi(2)*w*H/Vs(3)).^2);
```

```
Rd_dmp700(:,3)=1./sqrt(cos(w*H/Vs(3)).^2 + (xi(3)*w*H/Vs(3)).^2);
```

```
% END
```

A.2 Fourier Amplitude Spectra

An earthquake time series or any response time series fulfilling certain criterias can be expressed as an infinite sum of sinusoid

$$\ddot{u}_g(t) \approx c_0 + \sum_{n=1}^{\infty} c_n \sin(\omega_n t + \phi_n) \quad (\text{A.1})$$

where c_0 is the average value of the input signal, c_n is the amplitude, ω_n is the frequency and

ϕ_n is the phase of the n -th sinusoidal. A normal simplification for earthquakes is to put $c_0 = 0$ since they oscillate evenly about the x-axis. The amplitude of the different Fourier coefficients are given as

$$c_n = \sqrt{a_n^2 + b_n^2} \quad (\text{A.2a})$$

$$a_n = \frac{2}{t_{end}} \int_0^{t_{end}} \ddot{u}_g(t) \cos(\omega_n t) dt \quad (\text{A.2b})$$

$$b_n = \frac{2}{t_{end}} \int_0^{t_{end}} \ddot{u}_g(t) \sin(\omega_n t) dt \quad (\text{A.2c})$$

```
% DESCRIPTION:
% This script calculates and plots the Fourier Amplitude
% Spectra of a given earthquake ground acceleration record.
%
% INPUT:
% A=          Data to perform a FFT on
%
% OUTPUT:
% FFT=       the Fourier transformed vector
% f=         vector containing the range of frequencies
%
% OTHER SYMBOLS:
% t=         time [s]
% signal=    ground acceleration [g]
% dt=        time interval between each sampling
% v=         ground velocity
% d=         grouond displacement
% nyqf=      Nyquist frequency
% fs=        samples pr. unit time
% aVf=       the flucturating part of the grund acceleration
% ak=        a vector containg values of the first Fourier coeffisient
% bk=        a vector containg values of the second Fourier coeffisient
```

```

%
% Written by JEANETT RORVIG, January 2014
% Exercise 1 on earthquake

function [f,FFT]=Fourier_Amp_Spectra(signal,t)

close all
dt=t(2)-t(1);

fs=1/dt;
nyqf=fs/2;
n=length(signal);
f=linspace(0,nyqf,round(n/2));

aVf=signal-mean(signal);
fftaVf=2*(fft(aVf))/round(n);
ak=(imag(fftaVf(1:round(n/2))));
bk=(real(fftaVf(1:round(n/2))));
ck=sqrt(ak.^2+bk.^2);
FFT=ck;

g=figure(2);
plot(f,FFT);
axis([0 10 0 1.05*max(ck)]);
xlabel('Frequency [Hz]')
ylabel('Amplitude c_k [g]')

%END

```

A.3 Pseudo-Acceleration Response Spectra

The following script produces the pseudo-acceleration and displacement spectra of a given earthquake input \ddot{u}_g . The script uses Newmarks' numerical integration method assuming lin-

early varying acceleration between each time step.

```

% DESCRIPTION: This script calculates and plots the pseudo-acceleration
% response spectra of a given earthquake ground acceleration record. The
% equation of motion for a SDOF-system is solved numerically by Newmarks
% integration method.
%
%
% INPUT:
% acc      = ground acceleration data [m/s^2]
% dt       = homogenous time increment [s]
% Tend     = maximal natural frequency of interest [s]
% xi       = damping in the SDOF-system [-]
%
% OUTPUT:
% Sd=      vector containing values of the Response Displacement Spectra
% Sa=      vector containing values of the Response Acceleration Spectra
% T=       vector containing natural periods
%
% OTHER SYMBOLS:
% a        = structure acceleration
% v        = ground velocity
% d        = ground displacement
%
% Written by JEANETT RORVIG, March 2014
% Exercise 1 on earthquake

function [T,Sd,Sa]=Response_Spectrum(t,acc,xi)
close all
clc

gamma=1/2;           % Newmarks constants
beta=1/6;
Tend=3;

```

```

dt=t(2)-t(1);
n=length(t);
u=zeros(n,1);      % Time-history responses
v=zeros(n,1);
a=zeros(n,1);

T=zeros(200,1);
dT=Tend/length(T); % frequency increments

for i=1:length(T);
    m=1;
    w(i)=2*3.14/T(i);
    k=w(i)^2*m;
    c=2*xi*w(i)*m;
    a1=(1/(beta*dt^2))*m+gamma*c/(beta*dt);
    a2=(1/(beta*dt))*m+(gamma/beta-1)*c;
    a3=(1/(2*beta)-1)*m+dt*(gamma/(2*beta)-1)*c;
    keff=k+a1;
    for j=1:n-1
        peff(j+1)=-m*acc(j+1)+a1*u(j)+a2*v(j)+a3*a(j);
        u(j+1)=peff(j+1)/keff;
        v(j+1)=gamma/(beta*dt)*(u(j+1)-u(j))+(1-gamma/beta)*v(j)+dt*(1-gamma/(2*beta))*a(j);
    end
    Sd(i)=max(abs(u));
    Sa(i)=Sd(i)*w(i)^2;
    T(i+1)=T(i)+dT;
end

T(end)=[]; % Need to delete last cell in T to make it the same length as Sa

a=figure(1);
plot(T,Sa)
hold on
PrettyPlotgca
xlabel('Natural period T [s]')
ylabel('S_A')

```

```

title('Pseudo-acceleration response spectra')

%% EC8 design response spectra

% S_d      = design pseudo-acceleration
% T_i      = the i-th period defined in EC8
% a_g      = design ground acceleration on type A soil.
% a_gR     = reference peak ground acceleration on type A soil
% a_g40Hz  =
% imp      = important class

q=1;
N=500;
s=1;

a_g=0.8*1*1.51;          % a_g=imp*a_gR=imp*0.8*a_g40Hz
T_B=0.01;
T_C=0.25;
T_D=1.5;

T_EC=linspace(0,Tend,N);
S_d=zeros(1,N);
for i=1:N
    if T_EC(i)<=T_B;
        S_d(i)=a_g*s*(2/3 + T_EC(i)/T_B*(2.5/q - 2/3));
    end
    if T_EC(i)> T_B && T_EC(i)<=T_C
        S_d(i)=a_g*s*2.5/q;
    end
    if T_EC(i) > T_C && T_EC(i) <= T_D;
        S_d(i)=a_g*s*2.5/q*T_C/T_EC(i);
    end
    if T_EC(i)> T_D;
        S_d(i)=a_g*s*2.5/q*(T_C*T_D/(T_EC(i))^2);
    end
end

```

```
end
```

```
% END
```


Appendix B

Additional Theory

B.1 Direct Numerical Integration

Direct integration refers to the calculation of response history using step-by-step integration in time, without changing the form of the dynamic equilibrium equations as is done in modal methods. The time period T of interest is divided into time increments $\Delta t = T/N$ and response is calculated at each time instance $\Delta t, 2\Delta t, 3\Delta t, \dots, n\Delta t$, and so on. A general expression of the equation of motion suitable for non-linear problems at the n th time step is

$$\mathbf{M}\{\ddot{\mathbf{D}}\}_n + \mathbf{C}\{\dot{\mathbf{D}}\}_n + \{\mathbf{R}^{\text{int}}\}_n = \{\mathbf{R}^{\text{ext}}\}_n \quad (\text{B.1})$$

Numerical integration methods can be classified as *explicit* or *implicit*.

Newmark's method

Newmark's method is an unconditionally stable single-step implicit numerical integration algorithm based on the following equations:

$$\dot{u}_{i+1} = \dot{u}_i + [(1 - \gamma)\Delta t]\ddot{u}_i + (\gamma\Delta t)\ddot{u}_{i+1} \quad (\text{B.2a})$$

$$u_{i+1} = u_i + (\Delta t)\dot{u}_i + [(0.5 - \beta)(\Delta t)^2]\ddot{u}_i + [\beta(\Delta t)^2]\ddot{u}_{i+1} \quad (\text{B.2b})$$

The parameters γ and β define the variation of the acceleration over a time step and determine the stability and accuracy of the solution. The values $\gamma = \frac{1}{2}$ and $\beta = \frac{1}{6}$ correspond to the assumption of a *linear* variation of acceleration over each time step Δt as shown in figure B.1.

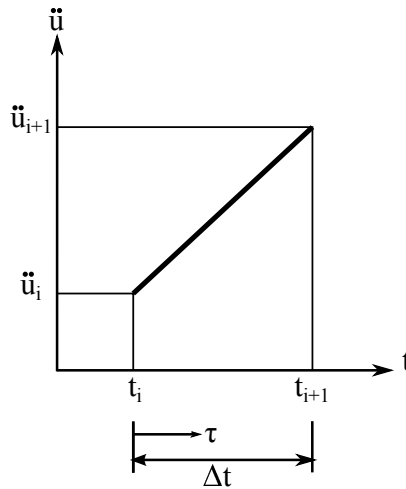


Figure B.1: Linear acceleration in Newmark's method

From equation (B.2b), \ddot{u}_{i+1} can be expressed in terms of the unknown variable u_{i+1} as

$$\ddot{u}_{i+1} = \frac{1}{\beta(\Delta t)^2}(u_{i+1} - u_i) - \frac{1}{\beta\Delta t}\dot{u}_i - \left(\frac{1}{2\beta} - 1\right)\ddot{u}_i \quad (\text{B.3})$$

Substituting this into equation (B.2a) gives \dot{u}_{i+1} in terms of u_{i+1}

$$\dot{u}_{i+1} = \frac{\gamma}{\beta\Delta t}(u_{i+1} - u_i) + \left(1 - \frac{\gamma}{\beta}\right)\dot{u}_i + \Delta t \left(1 - \frac{\gamma}{2\beta}\right)\ddot{u}_i \quad (\text{B.4})$$

The equation of motion for a *linear* system at time $i + 1$ is

$$m\ddot{u}_{i+1} + c\dot{u}_{i+1} + ku_{i+1} = p_{u+1} \quad (\text{B.5})$$

When the expressions for \ddot{u}_{i+1} and \dot{u}_{i+1} are substituted into the equation of motion for linear systems the following expressions for the response u_{i+1} is obtained

$$\hat{k}u_{i+1} = \hat{p}_{i+1} \quad (\text{B.6})$$

where

$$\hat{k} = k + \frac{\gamma}{\beta\Delta t}c + \frac{1}{\beta(\Delta t)^2}m \quad (\text{B.7})$$

and

$$\begin{aligned} \hat{p}_{i+1} = p_{i+1} + & \underbrace{\left[\frac{1}{\beta(\Delta t)^2}m + \frac{\gamma}{\beta\Delta t}c \right]}_{a_1} u_i + \underbrace{\left[\frac{1}{\beta\Delta t}m + \left(\frac{\gamma}{\beta} - 1\right)c \right]}_{a_2} \dot{u}_i \\ & + \underbrace{\left[\left(\frac{1}{2\beta} - 1\right)m + \Delta t \left(\frac{\gamma}{2\beta} - 1\right)c \right]}_{a_3} \ddot{u}_i \end{aligned} \quad (\text{B.8})$$

B.2 Derivation of the solution to the harmonic equation of motion $m\ddot{u} + c\dot{u} + ku = P_0 \cos(\omega t)$

The equation of motion for a system with a harmonic cosine load and viscous damping reads

$$m\ddot{u} + c\dot{u} + ku = p_0 \cos(\omega t) \quad (\text{B.9})$$

The particular solution to this inhomogenous partial differential equation is proportional to the loading, but generally out of phase through a complex amplitude $A(\omega)$. A particular solution is generally written on the form

$$u_p = Ae^{i\omega t} \quad (\text{B.10})$$

which gives for the response derivatives

$$\dot{u}_p = Ai\omega e^{i\omega t} \quad (\text{B.11a})$$

$$\ddot{u}_p = -\omega^2 Ae^{i\omega t} \quad (\text{B.11b})$$

Insert this into the equation of motion to obtain

$$Ae^{i\omega t} [-m\omega^2 + i\omega c + k] = p_0 e^{i\omega t} \quad A [1 - \beta^2 + 2i\xi\beta] = \frac{p_0}{k}$$

Insert $c = 2\xi m\omega_n$ and $k = \omega_n^2 m$ where $\beta = \frac{\omega}{\omega_n}$. Hence

to obtain $A = \frac{p_0}{k} \frac{1}{(1 - \beta^2) + i2\xi\beta}$

(B.12)

This expression for the complex response amplitude A is easier drawn in a diagram if the imaginary part can be isolated. Multiplying the fraction by the complex conjugate $(1 - \beta^2 - i2\xi\beta)$ the following complex expression is obtained

$$A = \frac{p_0}{k} \frac{1}{(1 - \beta^2)^2 + (2\xi\beta)^2} (1 - \beta^2 - i2\xi\beta) \quad (\text{B.13})$$

The particular solution is then

$$\begin{aligned} u_p(t) &= \text{Re} \left[A e^{i\omega t} \right] = \text{Re} \left[\frac{p_0}{k} \frac{1}{(1 - \beta^2)^2 + (2\xi\beta)^2} (1 - \beta^2 - i2\xi\beta) e^{i\omega t} \right] \\ &= \frac{p_0}{k} \frac{1}{(1 - \beta^2)^2 + (2\xi\beta)^2} \left[(1 - \beta^2) \cos \omega t + 2\xi\beta \sin \omega t \right] \end{aligned} \quad (\text{B.14})$$

From this it is obvious that the response is lagging behind by the representation of the sinusoidal term. An alternative representation of the response is found by rewriting the complex amplitude with modulus and an phase angle. The phase angle used defines the time lag of the resultant response relative to the amplitude of the loading. Hence

$$A(\omega) = \underbrace{\frac{p_0}{k} \frac{1}{\sqrt{(1 - \beta^2)^2 + (2\xi\beta)^2}}}_{\rho} e^{-i\theta} = \rho e^{-i\theta} \quad (\text{B.15})$$

where ρ is the length of the complex number and θ is the phase angle defined as

$$\theta = \arctan \left(\frac{2\xi\beta}{1 - \beta^2} \right) \quad (\text{B.16})$$

Finally, the solution is found as

$$u_p(t) = \text{Re} \left[A e^{i\omega t} \right] = \text{Re} \left[\rho e^{-i\theta} e^{i\omega t} \right] = \rho \text{Re} \left[e^{i(\omega t - \theta)} \right] \quad (\text{B.17})$$

Figure B.2 shows the configuration for the harmonic load $p_0 \cos \omega t = \text{Re} \left[p_0 e^{i\omega t} \right]$ and the response $u_p = \rho \text{Re} \left[e^{i(\omega t - \theta)} \right]$ for the time $t = 0$. It is clear that the response lag behind with an angle θ defined by the dashed lines (note: the values of the dashed lines do not represent the length of the complex amplitude ρ).

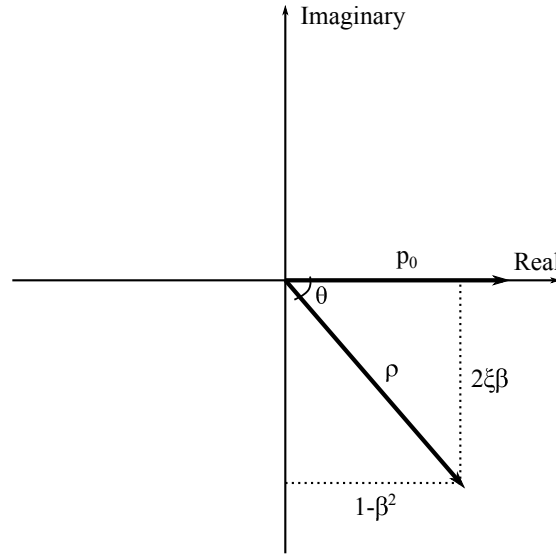


Figure B.2: The response $u_p = \rho e^{i(\omega t - \theta)}$ drawn in an Argand diagram.

B.3 Derivation of the Dynamic Impedance Function for a Single Oscillator

Roesset [26] gives an instructive analogy between the dynamic response of the simple oscillator and of a three-dimensional massless foundation-soil system. For an external harmonic load $p(t) = p_0 e^{i\omega t}$ the displacement is given on the form $u(t) = u_0 e^{i\omega t}$.

$$u(t) = u_0 e^{i\omega t} \quad \dot{u}(t) = i\omega u(t) \quad \ddot{u}(t) = -\omega^2 u(t) \quad (\text{B.18})$$

Insert this into the equation of motion $m\ddot{u} + c\dot{u} + ku = p(t)$ gives

$$(k - m\omega^2) + ic\omega = \frac{p(t)}{u(t)} \quad (\text{B.19})$$

and by comparison with equation (3.59)

$$K_1 = k - m\omega^2 \quad (\text{B.20a})$$

$$K_2 = c\omega \quad (\text{B.20b})$$

Rewrite equation (B.19) to express the dynamic impedance as a product of the static stiffness and a dynamic part.

$$K^* = k \left[\underbrace{\left(1 - \frac{\omega^2}{\omega_n^2}\right)}_k + i \underbrace{2\xi \frac{\omega}{\omega_n}}_{c_s} \right] \quad (\text{B.21})$$

The dynamic stiffness and damping coefficients of a SDOF-oscillator is shown in figure B.3. In general, k and c_s in a foundation-soil system have a complex distribution, depending primary on the mode of vibration, the geometry, rigidity and embedment of the foundation and the soil properties.

The frequency dependent part of the dynamic stiffness is suggested by Harte [13] to be important in soft soil conditions.

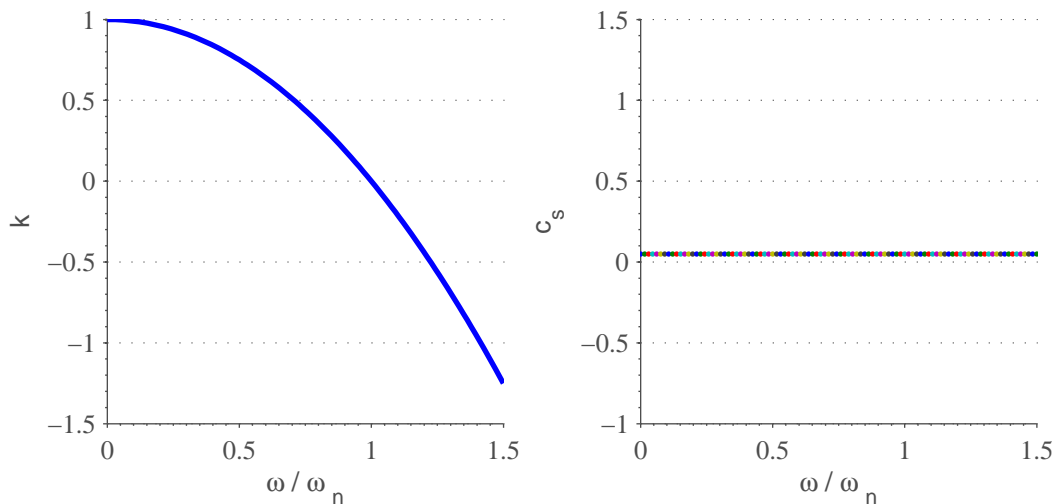


Figure B.3: Dynamic stiffness and damping coefficients of a 1-DOF oscillator.

Appendix C

Additional Information

C.1 Influence of damping on seismic response

Figure C.1 shows how the response of a structure subjected to different earthquakes varies with the assigned modal damping ratios ξ . The figure shows the the response for $\xi = 0.5\%$ and $\xi = 5\%$ for the first mode.

C.2 EC8 Concepts

For the horizontal components of the seismic action the design spectrum $S_d(T)$ shall be defined by the following expressions

$$0 \leq T \leq T_B : \quad S_d(T) = a_g s \left[\frac{2}{3} + \frac{T}{T_b} \left(\frac{2.5}{q} - \frac{2}{3} \right) \right] \quad (\text{C.1a})$$

$$T_B \leq T \leq T_C : \quad S_d(T) = a_g s \frac{2.5}{q} \quad (\text{C.1b})$$

$$T_C \leq T \leq T_D : \quad S_d(T) = a_g s \frac{2.5 T_C}{q T} \quad (\text{C.1c})$$

$$T_D \leq T : \quad S_d(T) = a_g s \frac{2.5 T_C T_D}{q T^2} \quad (\text{C.1d})$$

and

$$a_g = \gamma_1 a_{gR} = \gamma_1 0.8 a_{g40Hz} \quad (\text{C.2})$$

where a_g is the design ground acceleration for type A soil, s is the soil factor which represent the amplification of the input acceleration, q is the ductility coefficient ($q = 1$ for elastic response spectra), γ_1 is the seismic important coefficient and a_{g40Hz} is the peak ground acceleration with a return period of 475 years for Norway. From the seismic map in EC8 a value of $a_{g40Hz} = 0.55 \frac{m}{s^2}$ is used.

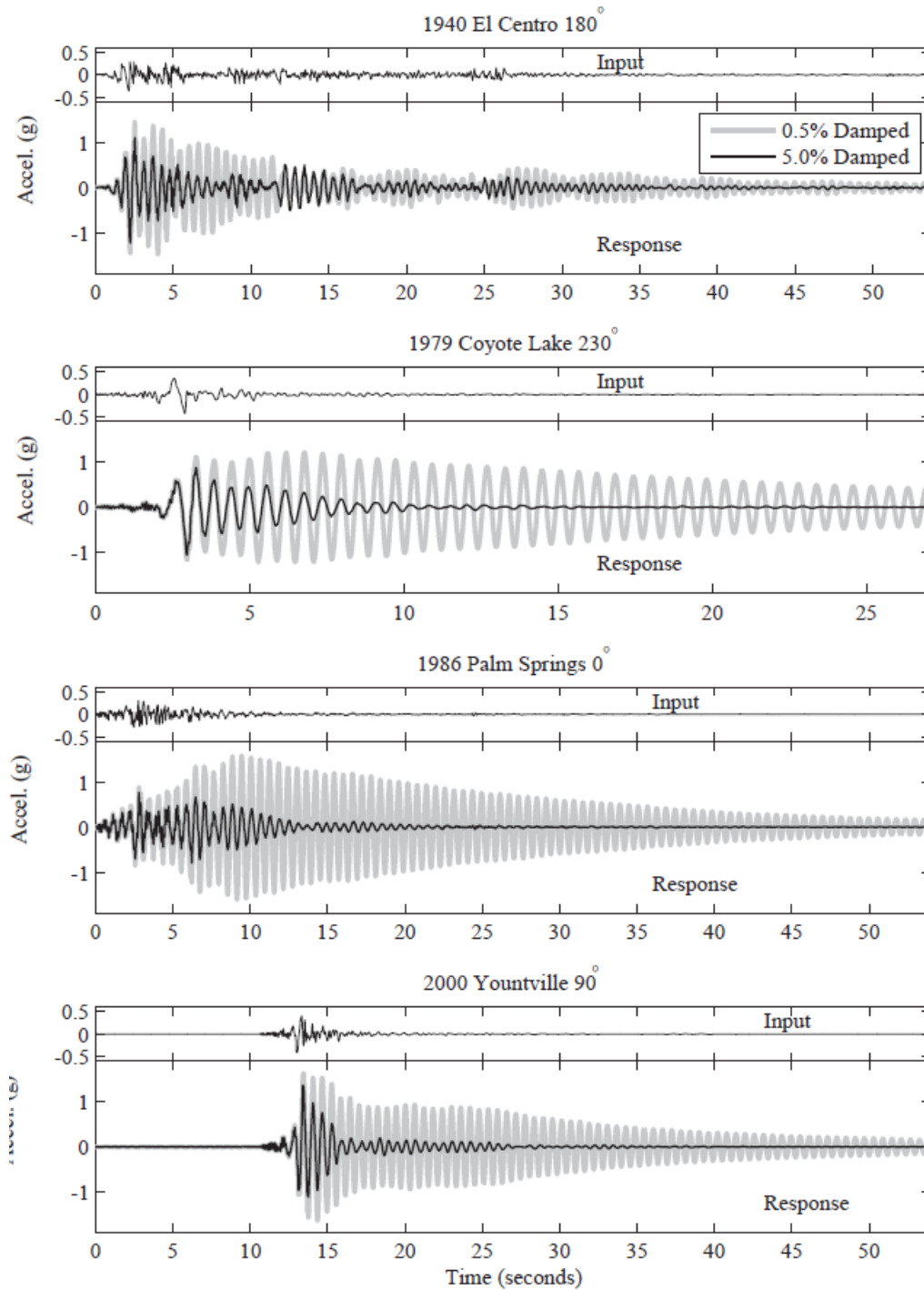


Figure C.1: Influence of damping on seismic response for different earthquake records. A critical modal damping ratio of 5% and 0.5% of the first modes are used.

Ground type	Description of stratigraphic profile	Parameters		
		$v_{s,30}$ (m/s)	N_{SPT} (blows/30cm)	c_u (kPa)
A	Rock or other rock-like geological formation, including at most 5 m of weaker material at the surface.	> 800	–	–
B	Deposits of very dense sand, gravel, or very stiff clay, at least several tens of metres in thickness, characterised by a gradual increase of mechanical properties with depth.	360 – 800	> 50	> 250
C	Deep deposits of dense or medium-dense sand, gravel or stiff clay with thickness from several tens to many hundreds of metres.	180 – 360	15 - 50	70 - 250
D	Deposits of loose-to-medium cohesionless soil (with or without some soft cohesive layers), or of predominantly soft-to-firm cohesive soil.	< 180	< 15	< 70
E	A soil profile consisting of a surface alluvium layer with v_s values of type C or D and thickness varying between about 5 m and 20 m, underlain by stiffer material with $v_s > 800$ m/s.			
S_1	Deposits consisting, or containing a layer at least 10 m thick, of soft clays/silts with a high plasticity index ($PI > 40$) and high water content	< 100 (indicative)	–	10 - 20
S_2	Deposits of liquefiable soils, of sensitive clays, or any other soil profile not included in types A – E or S_1			

Figure C.2: Classification of ground types according to EC8 [22].

Appendix D

Additional Results

D.1 Validation of the Soil

Figure D.1 shows the transfer function of the homogeneous soil profile using quadratic tetrahedron elements.

Amplification of ground displacement from soil model for quadratic tetrahedron element

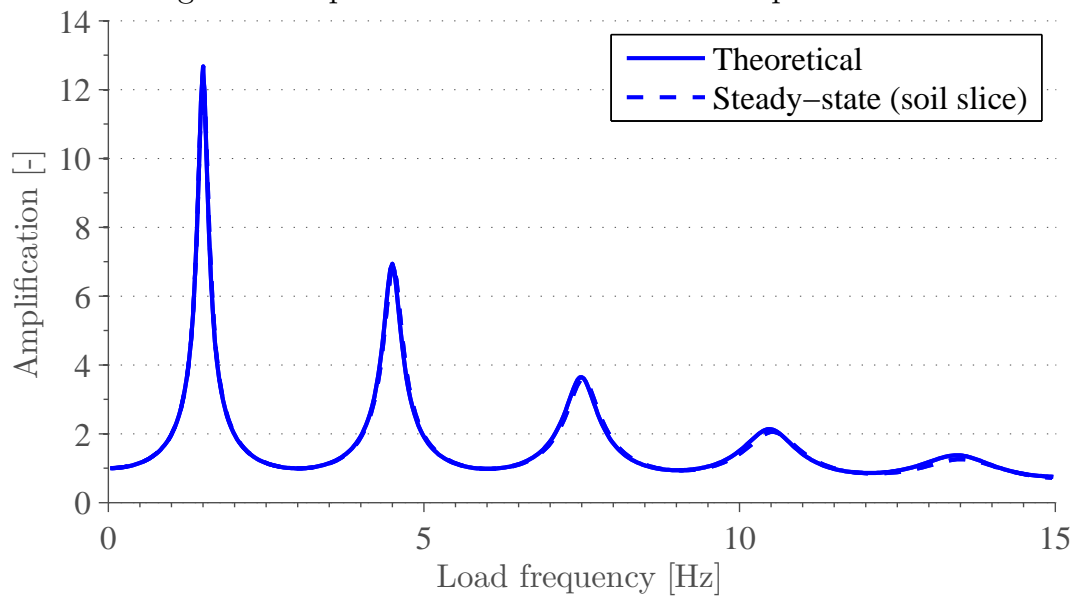


Figure D.1: Amplification of homogeneous soil with harmonic base excitation, 5 % Rayleigh damping, $V_s = 300$ m/s and quadratic tetrahedron elements.

D.2 Validation of Nordtank Wind Turbine Model

Time history responses

Figure [D.2](#) shows the displacement time history for model 1 and model 2 subjected to the horizontal Landers earthquake component.

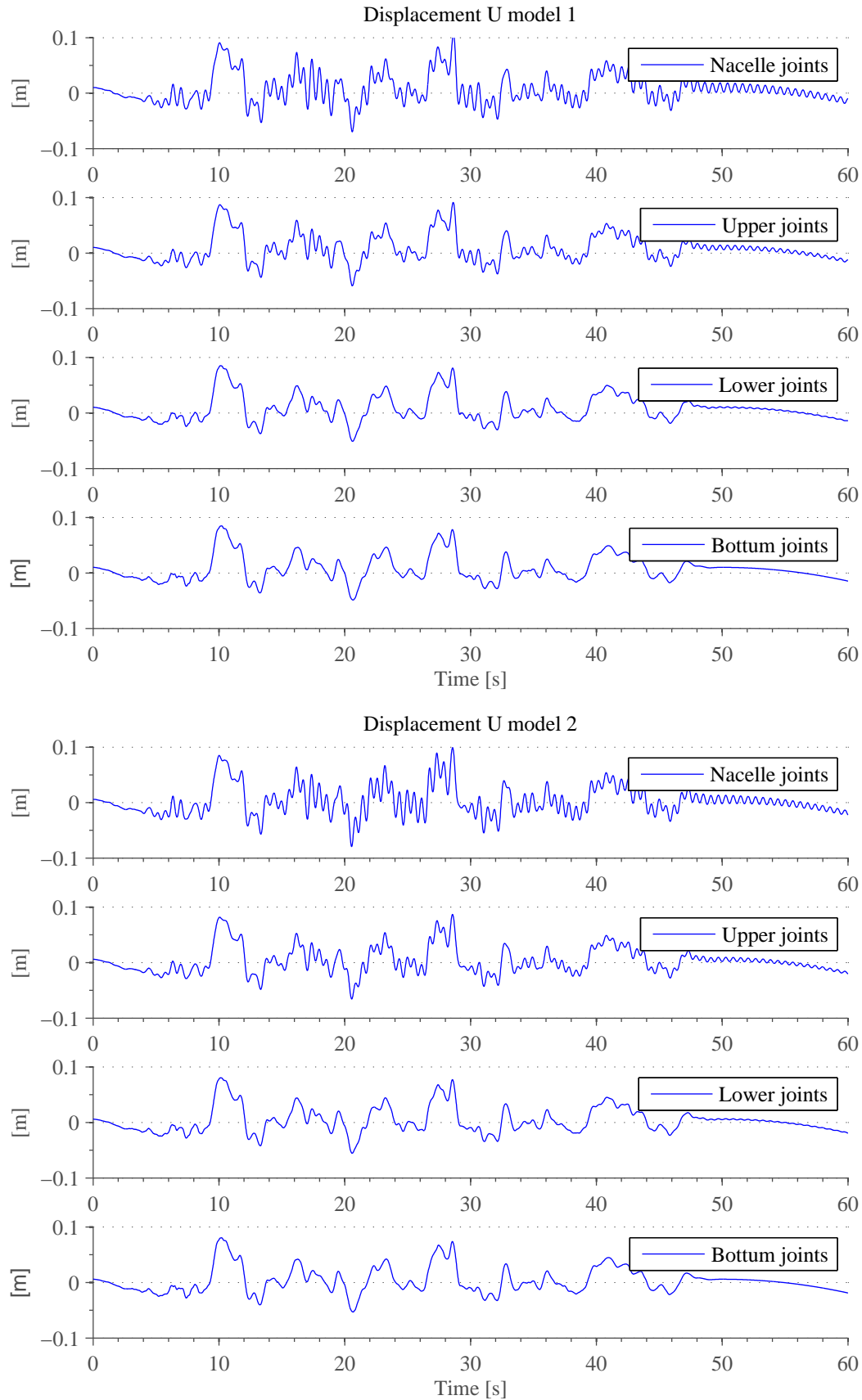


Figure D.2: Displacement time response of the shell model for a) model 1 which has a lumped mass representation of the nacelle and blades and b) model 2 which explicitly represent the nacelle and blades

D.3 Time history seismic response of the spring model

Part A: Three-Step-Method for the Soft Soil Profile

The time history comparison between the spring model and the full model for the soft soil profile is given in figure [D.3](#), [D.4](#), [D.5](#) and [D.6](#).

Part A: Kinematic Interaction vs. Free-field

It is shown in figure [D.7](#) and [D.8](#) that the kinematic interaction in the skirted foundation is negligible.

Part A: Importance of Rotational Term

It is shown in figure [D.9](#) and [D.10](#) that the rotational term is insignificant to the overall seismic response along the tower.

Part A: Fixed-base vs. Flexible-base for Soft Soil

Figure [D.11](#), [D.12](#), [D.13](#) and [D.14](#) show that difference in response for a fixed-base configuration and a flexible-base configuration for the soft soil profile.

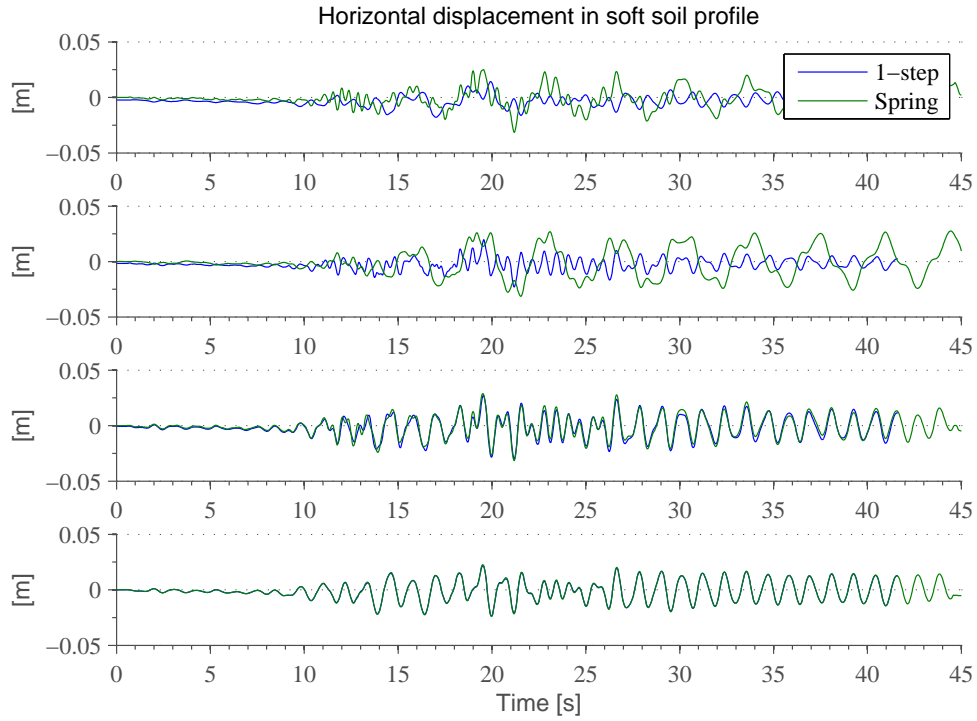


Figure D.3: Displacements along the tower for the full model and the spring model for the soft soil condition.

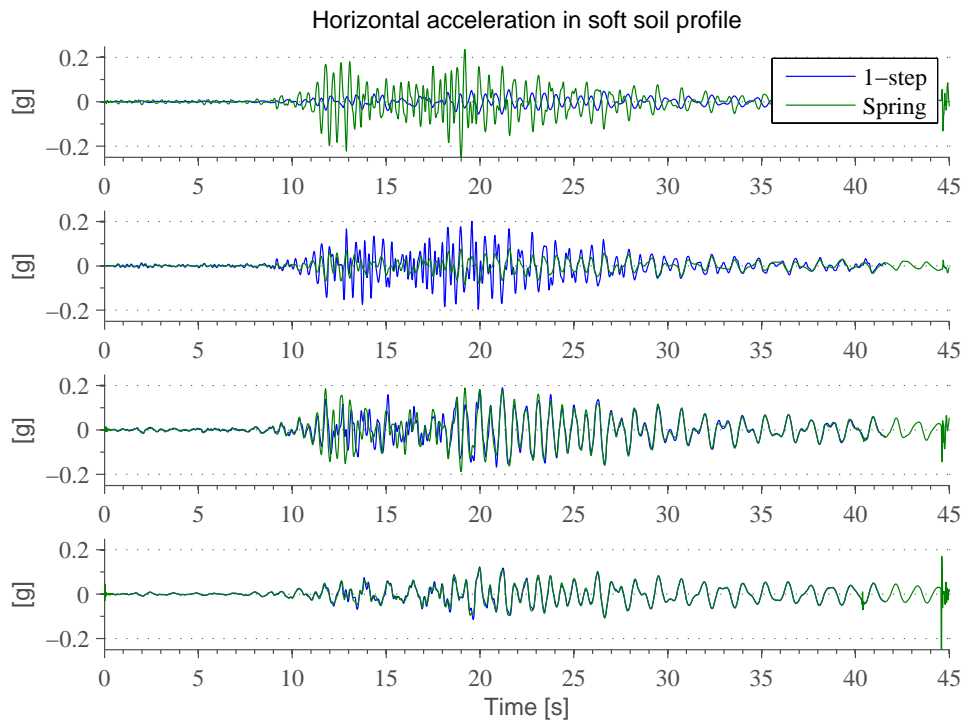


Figure D.4: Accelerations along the tower for the full model and the spring model for the soft soil condition.

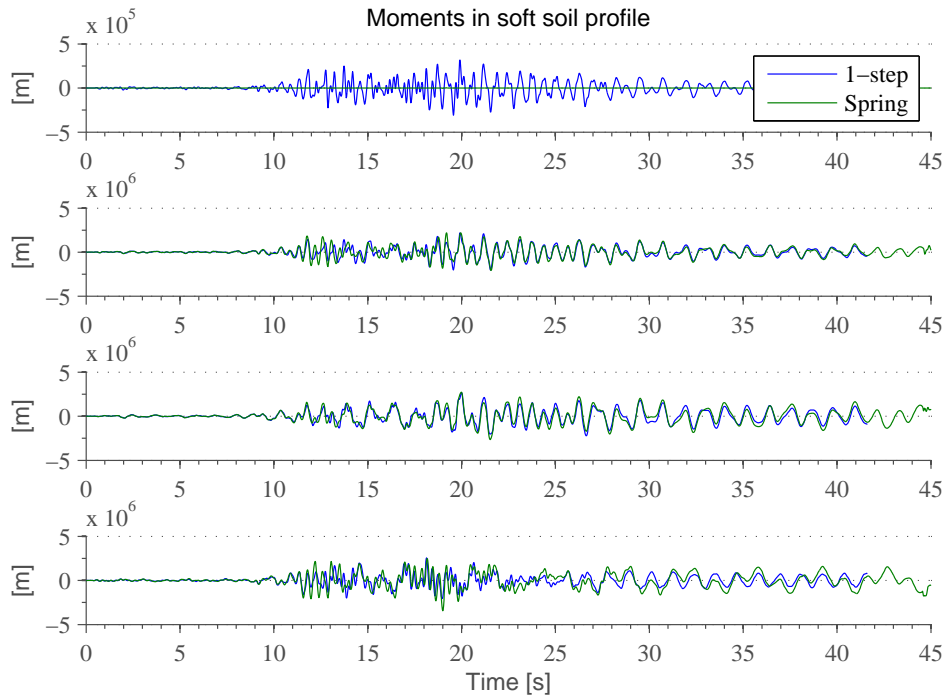


Figure D.5: Moments along the tower for the full model and the spring model for the soft soil condition.

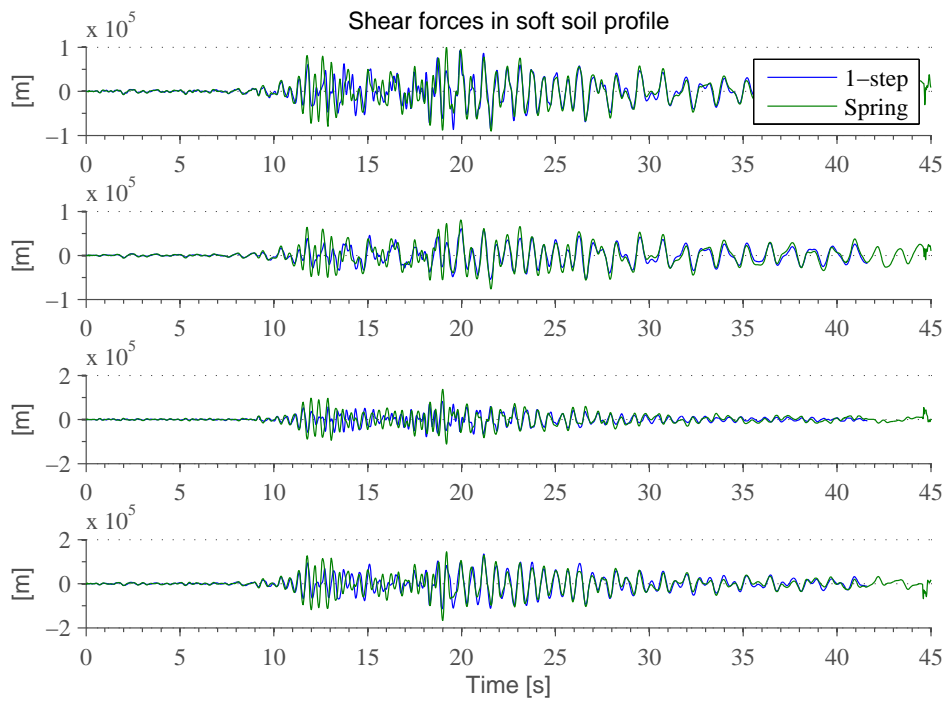


Figure D.6: Shear forces along the tower for the full model and the spring model for the soft soil condition.

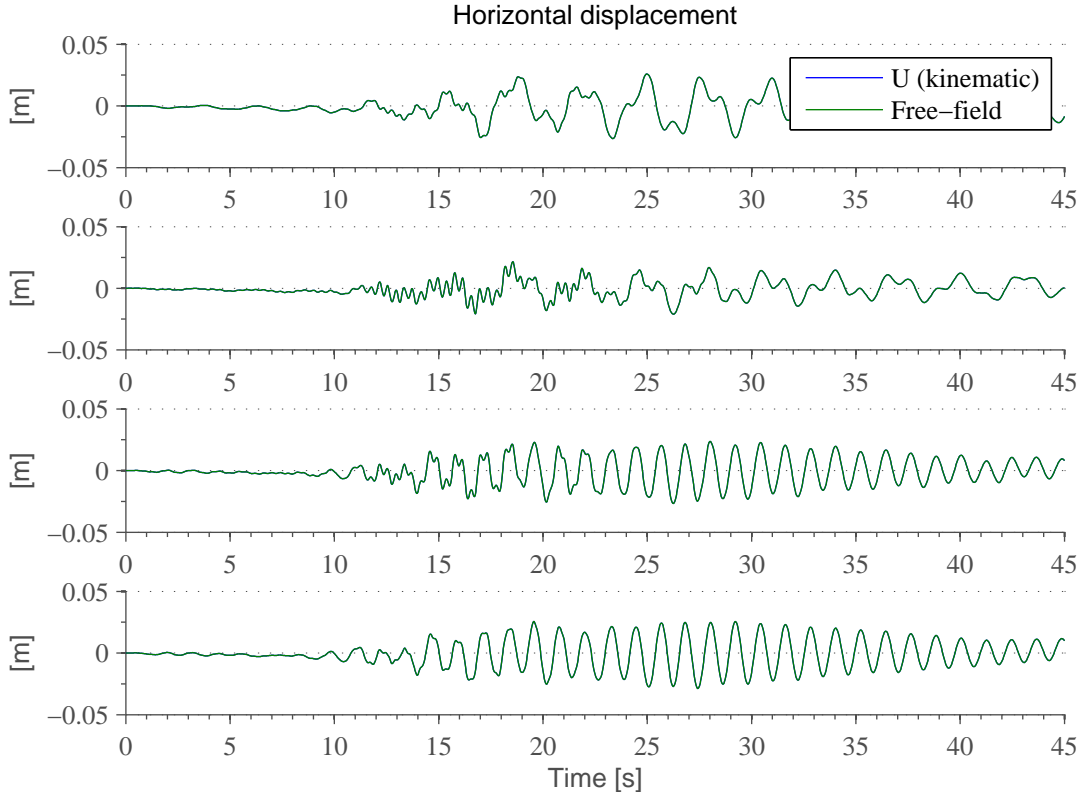


Figure D.7: Time history displacement along the tower for 1) kinematic spring input and 2) free-field input.

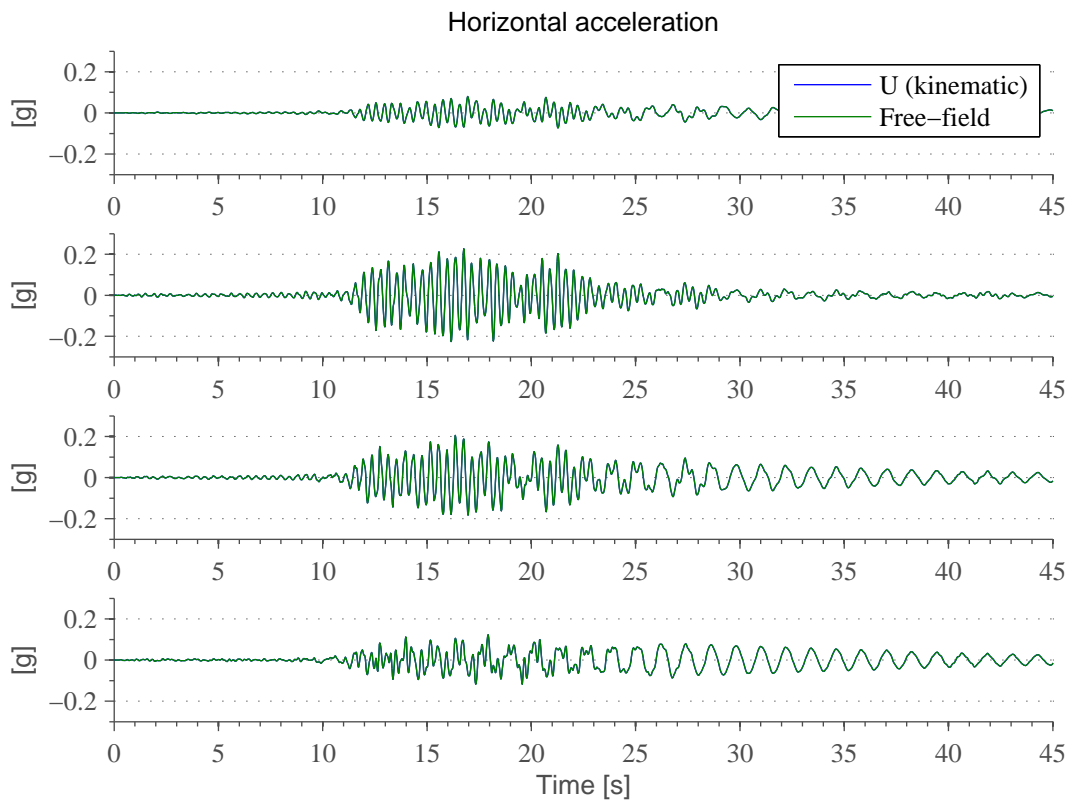


Figure D.8: Time history acceleration along the tower for 1) kinematic spring input and 2) free-field input.

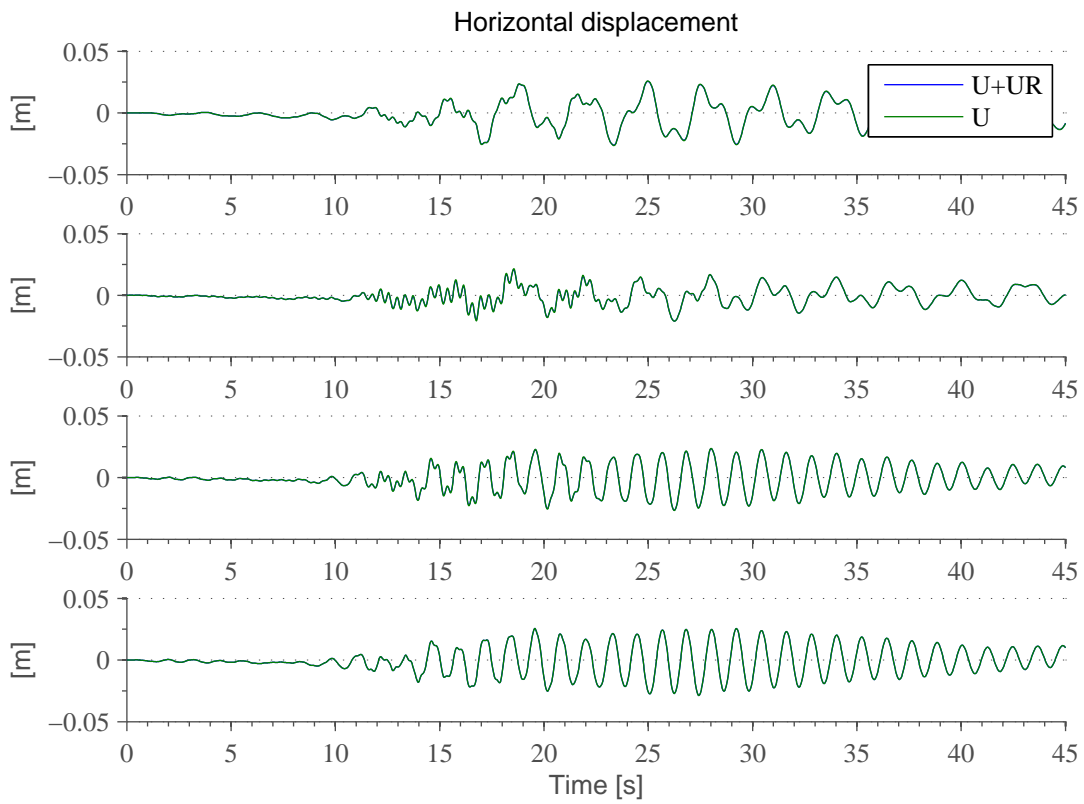


Figure D.9: Time history displacements along the tower for 1) translational and rotational spring input ($U+UR$) and 2) only translational spring input (U).

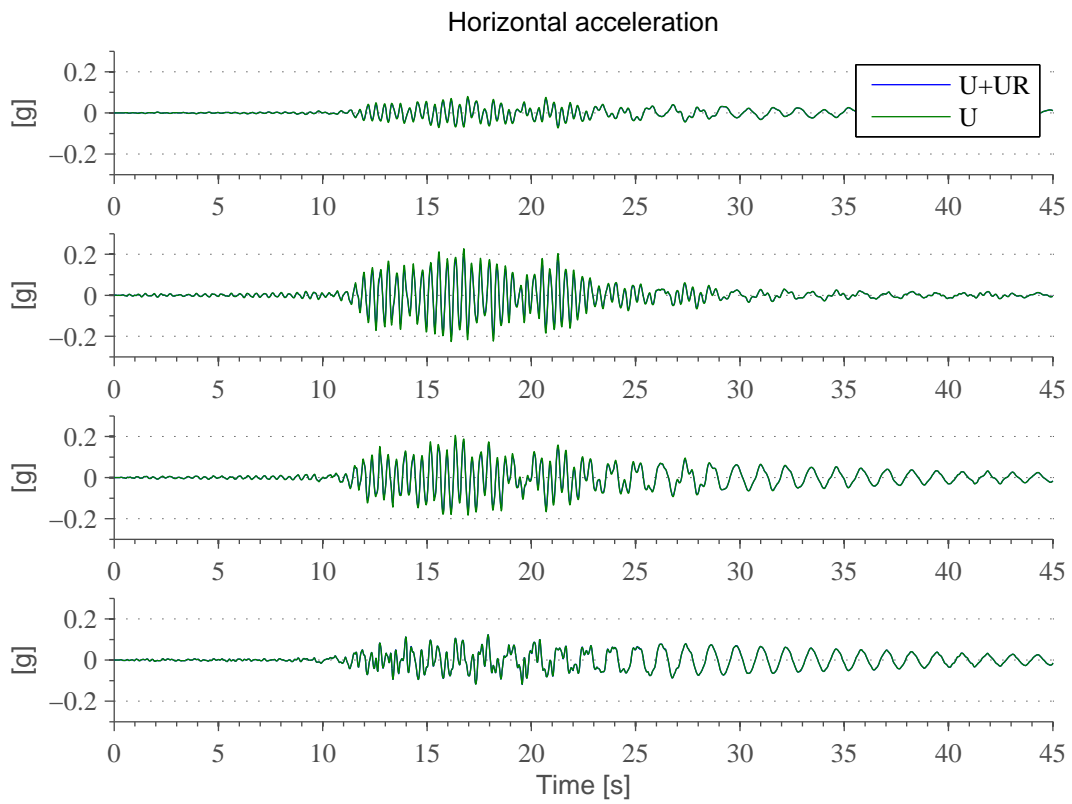


Figure D.10: Time history acceleration along the tower for 1) translational and rotational spring input ($U+UR$) and 2) only translational spring input (U).

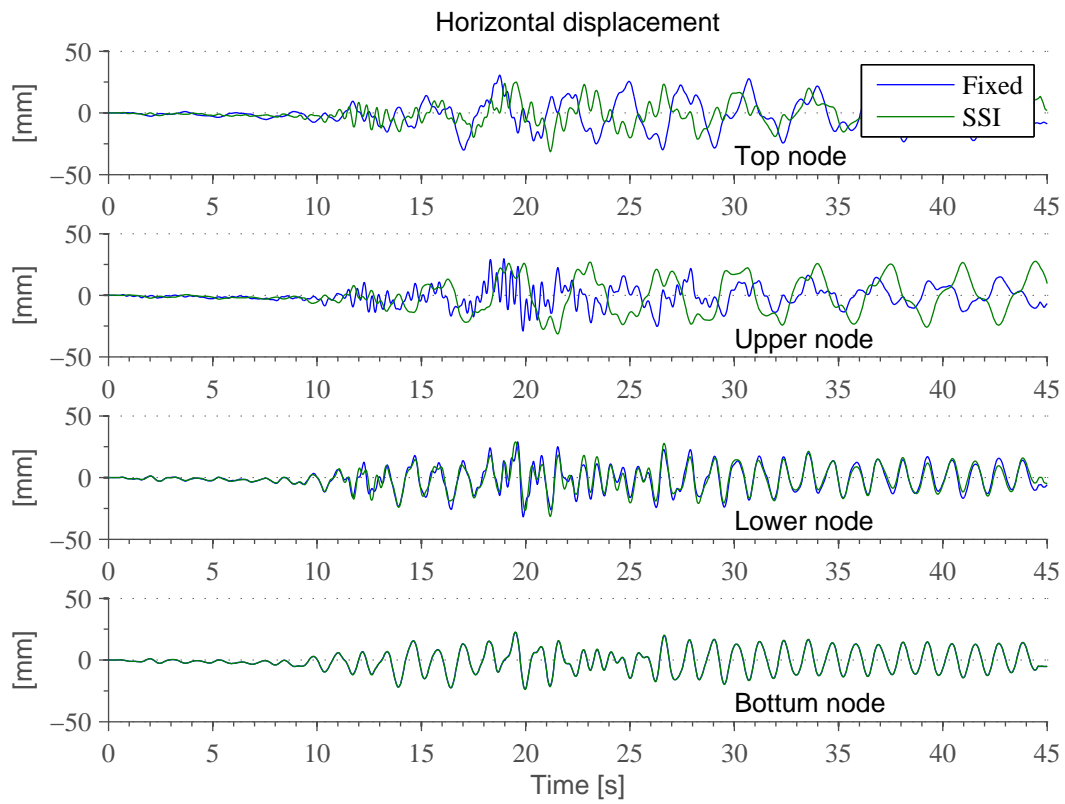


Figure D.11: Time history displacement along the tower for 1) a fixed-base configuration and 2) a flexible base configuration.

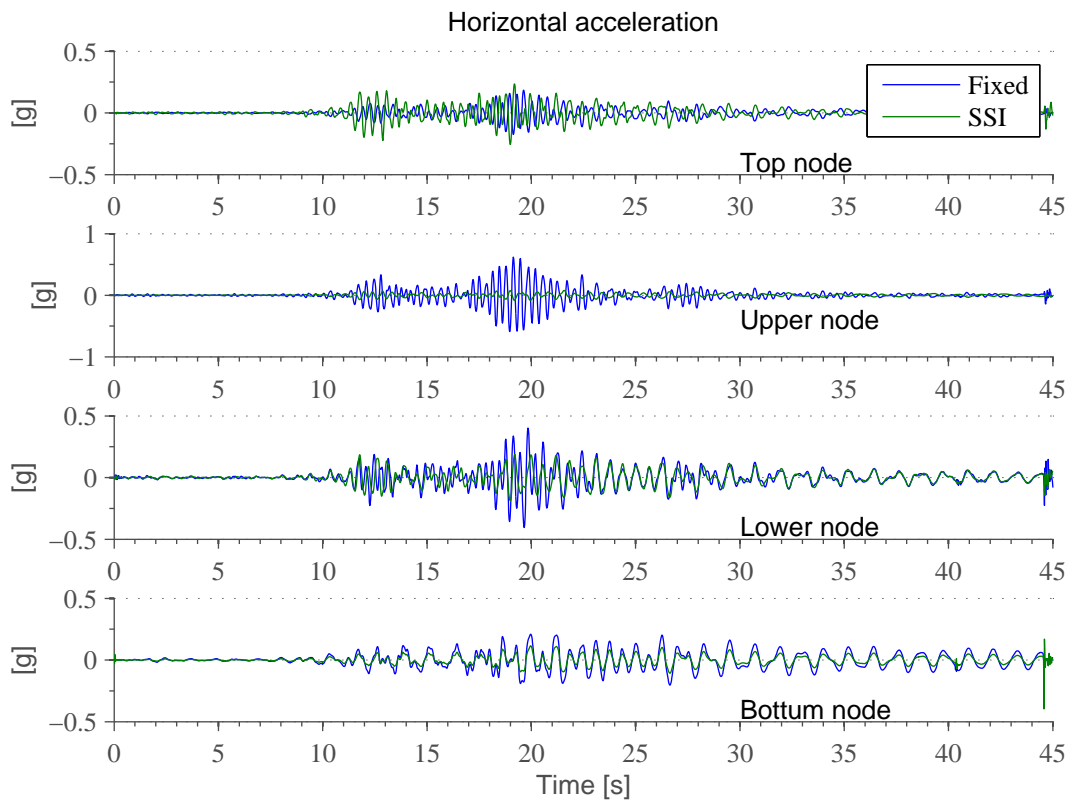


Figure D.12: Time history accelerations along the tower for 1) a fixed-base configuration and 2) a flexible base configuration.

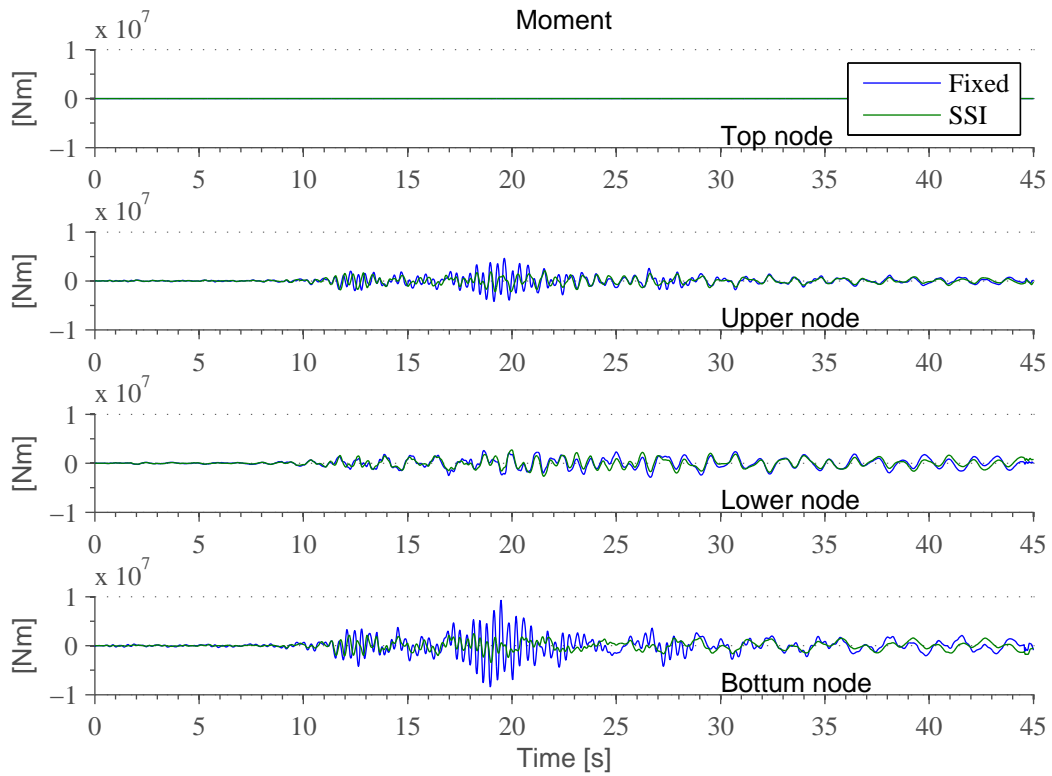


Figure D.13: Time history moments along the tower for 1) a fixed-base configuration and 2) a flexible base configuration.

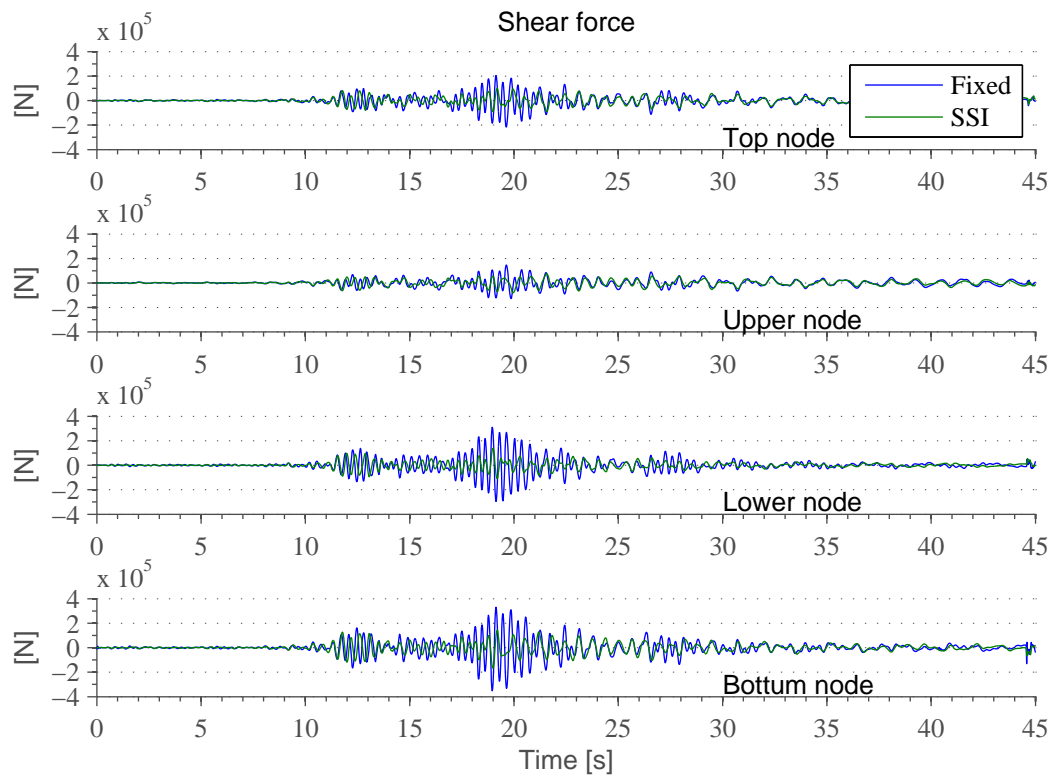


Figure D.14: Time history shear forces along the tower for 1) a fixed-base configuration and 2) a flexible base configuration.

Part B: Varying bucket radius

The time history responses in terms of the nacelle displacement and acceleration in addition to base moment and shear for different skirt radius are given in figure [D.15](#), [D.16](#), [D.17](#) and [D.18](#).

Part B: Varying bucket depths

The time history responses in terms of the nacelle displacement and acceleration in addition to base moment and shear for different skirt depths are given in figure [D.19](#), [D.20](#), [D.21](#) and [D.22](#).

Part B: Varying tower heights

The time history responses in terms of the nacelle displacement and acceleration in addition to base shear and moment for different tower heights are given in figure [D.23](#), [D.24](#), [D.26](#) and [D.25](#).

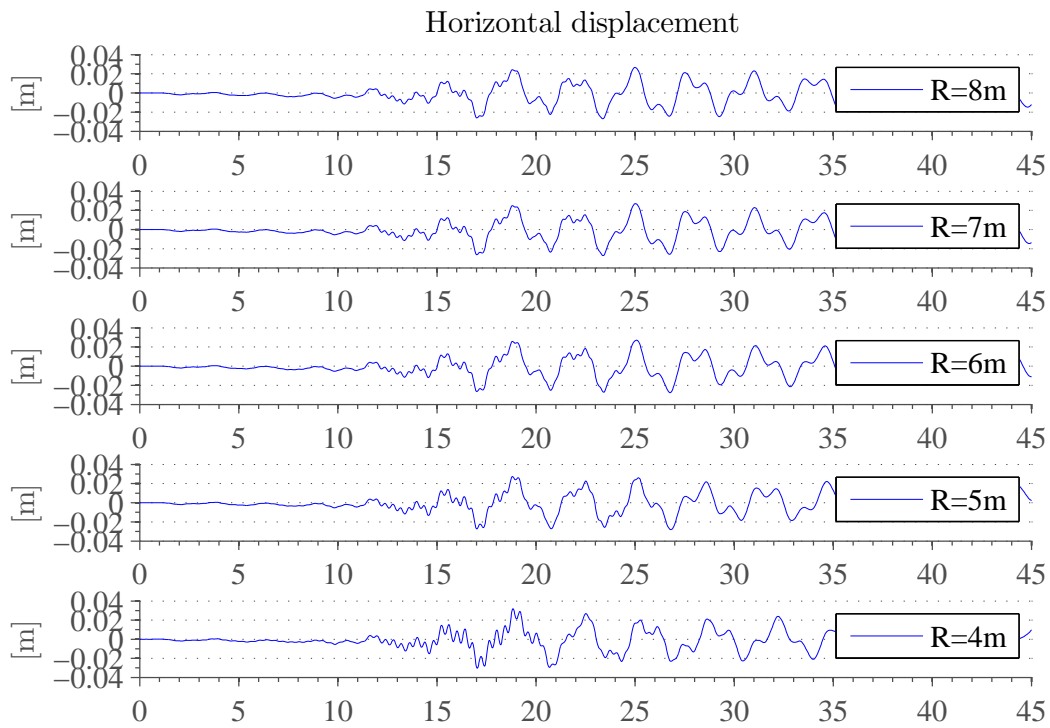


Figure D.15: Nacelle displacements for different bucket radius.

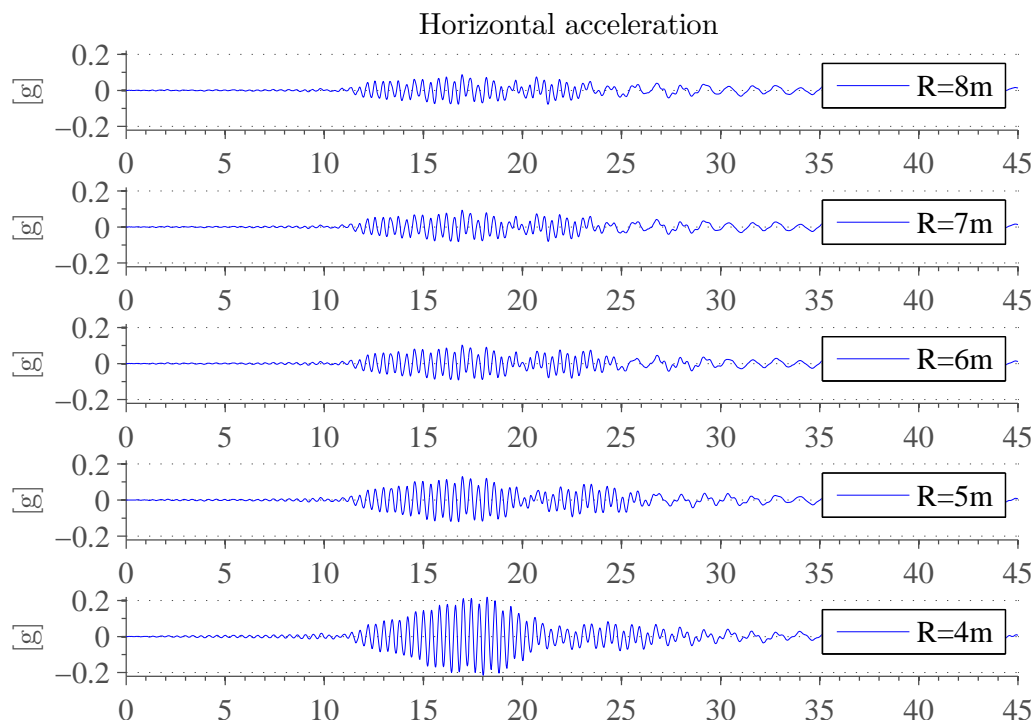


Figure D.16: Nacelle accelerations for different bucket radius.

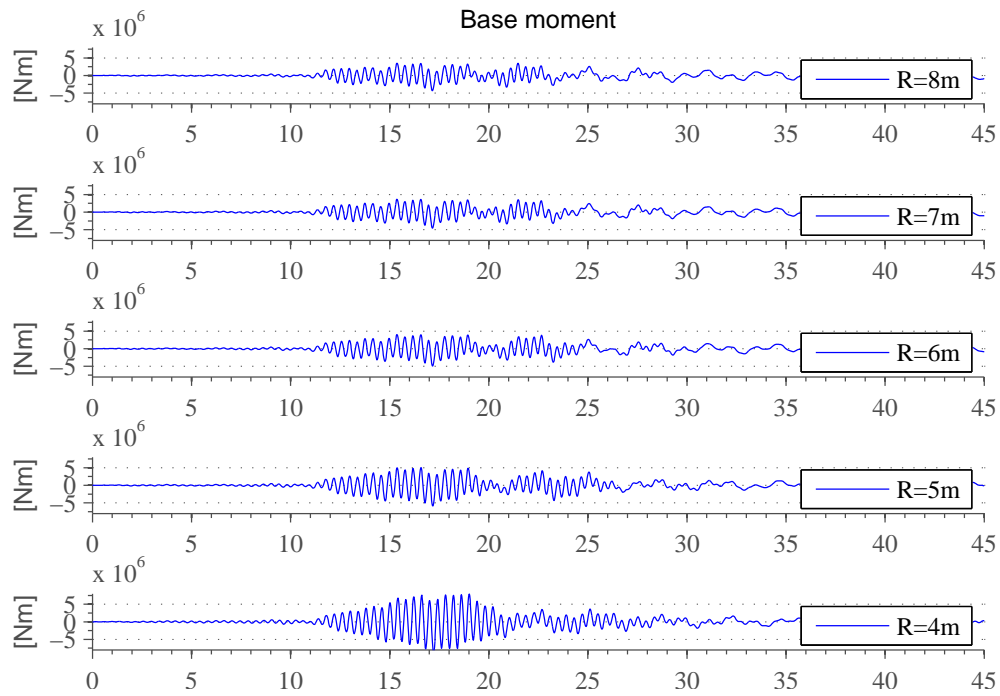


Figure D.17: Base moment for different skirt radius.

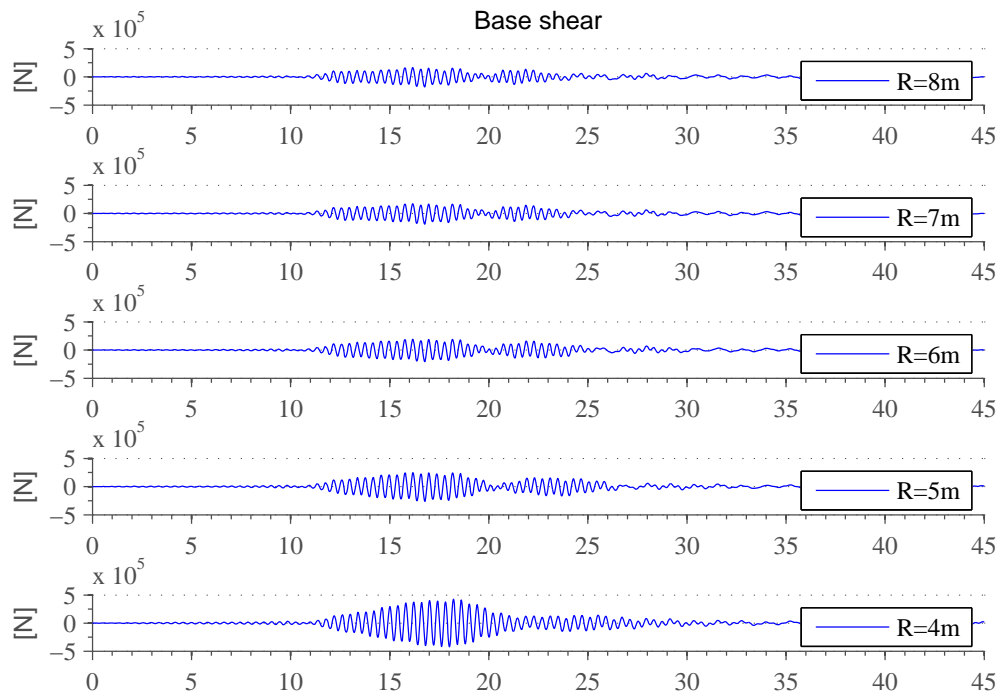


Figure D.18: Base shear for different skirt radius.

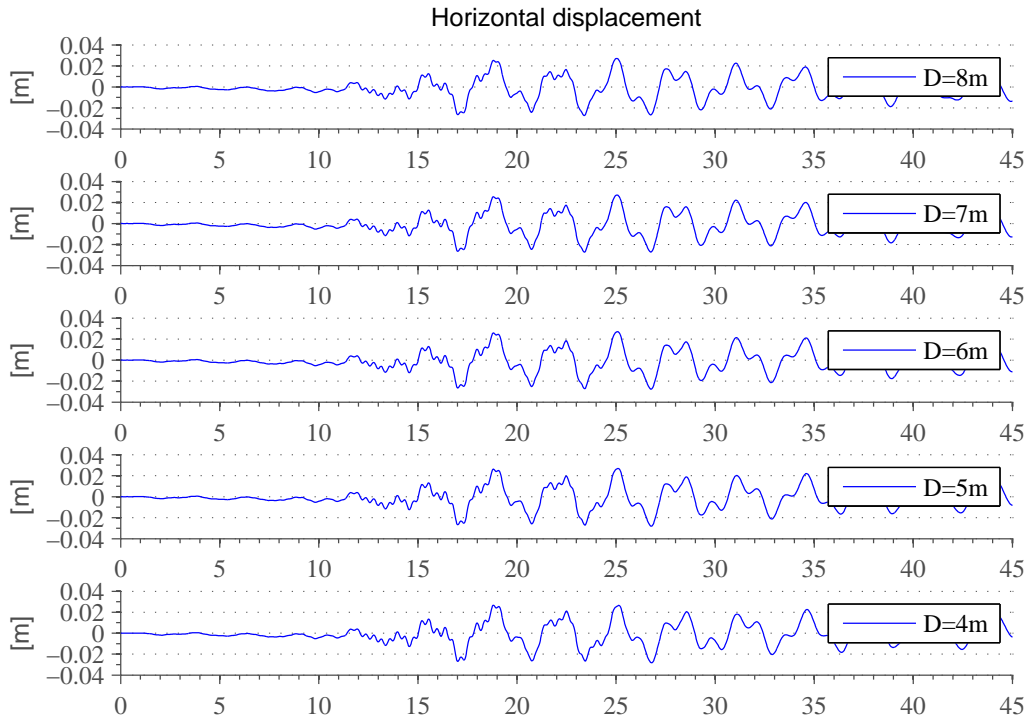


Figure D.19: Nacelle displacements for different bucket depths.

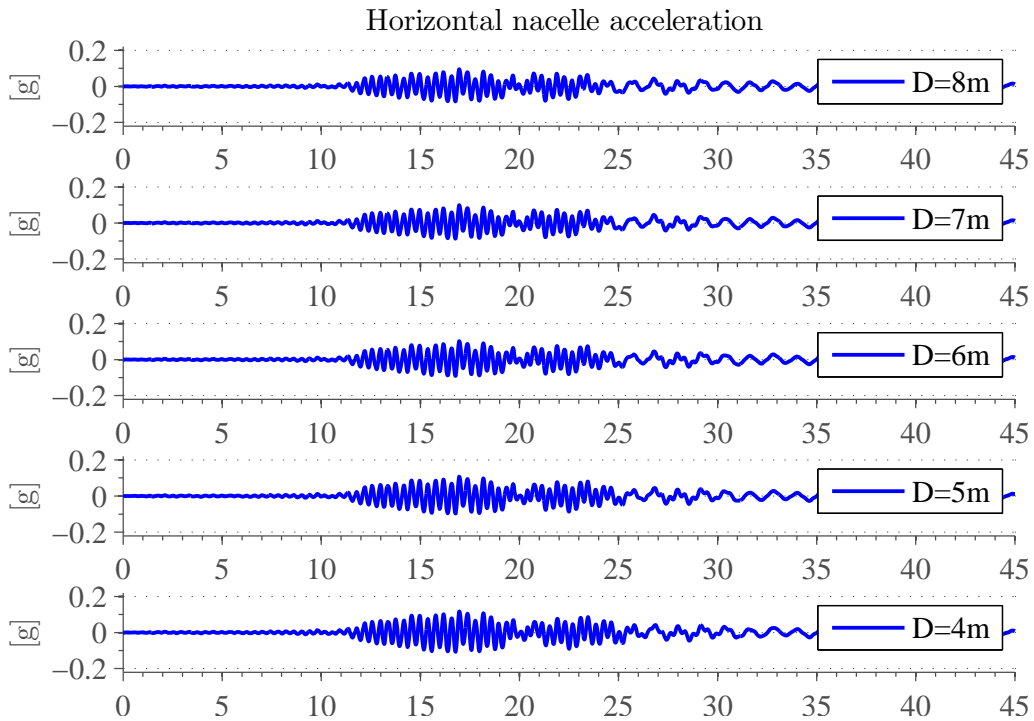


Figure D.20: Nacelle accelerations for different bucket depths.

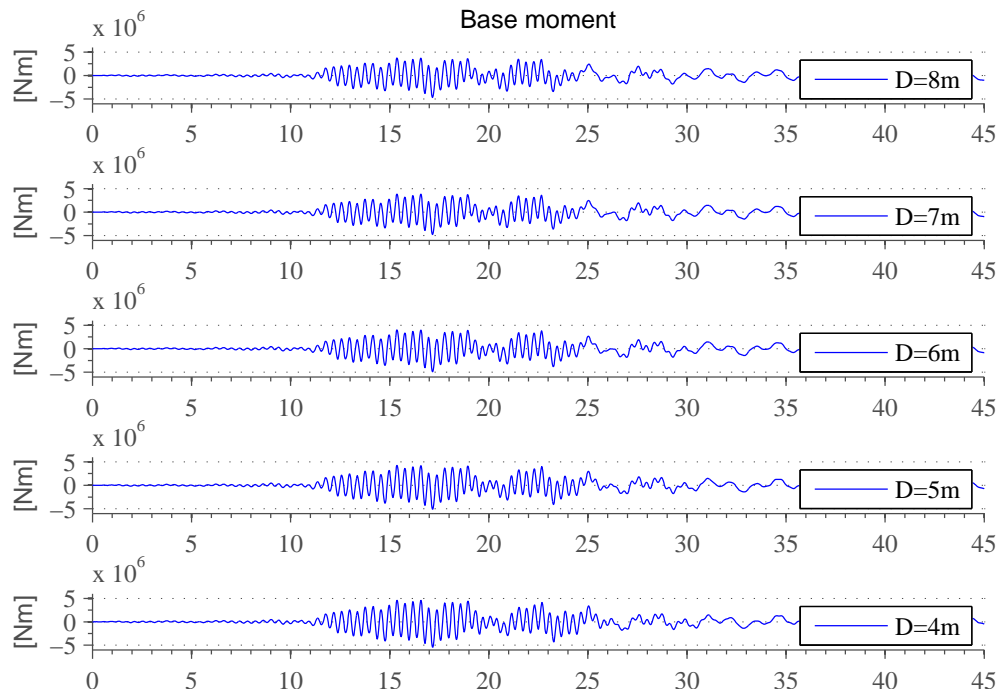


Figure D.21: Base moments for different skirt depths.

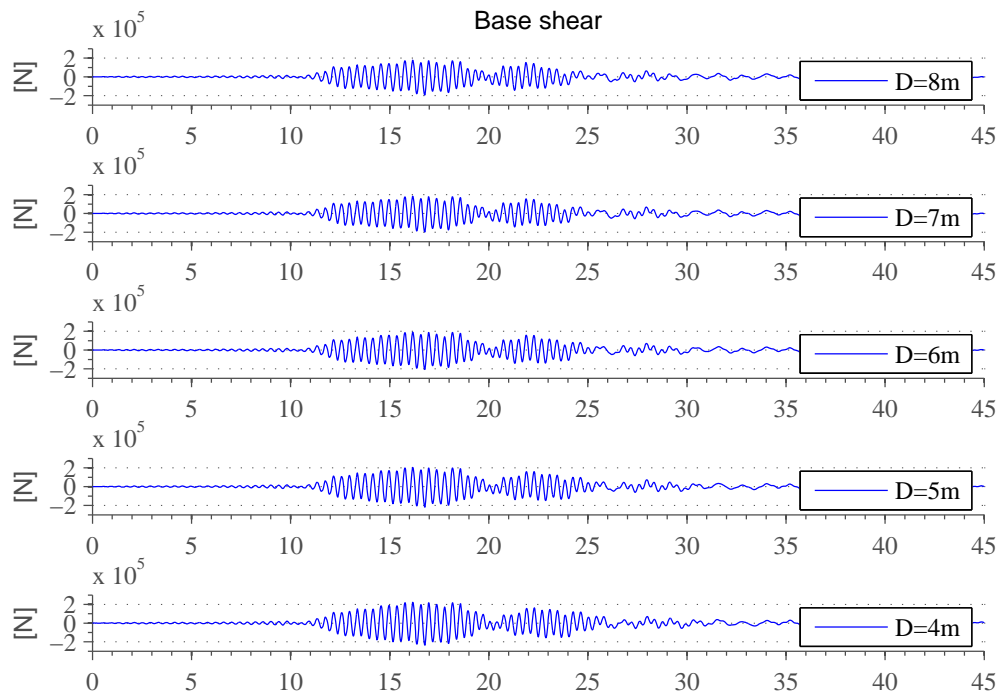


Figure D.22: Base shear for different skirt depths.

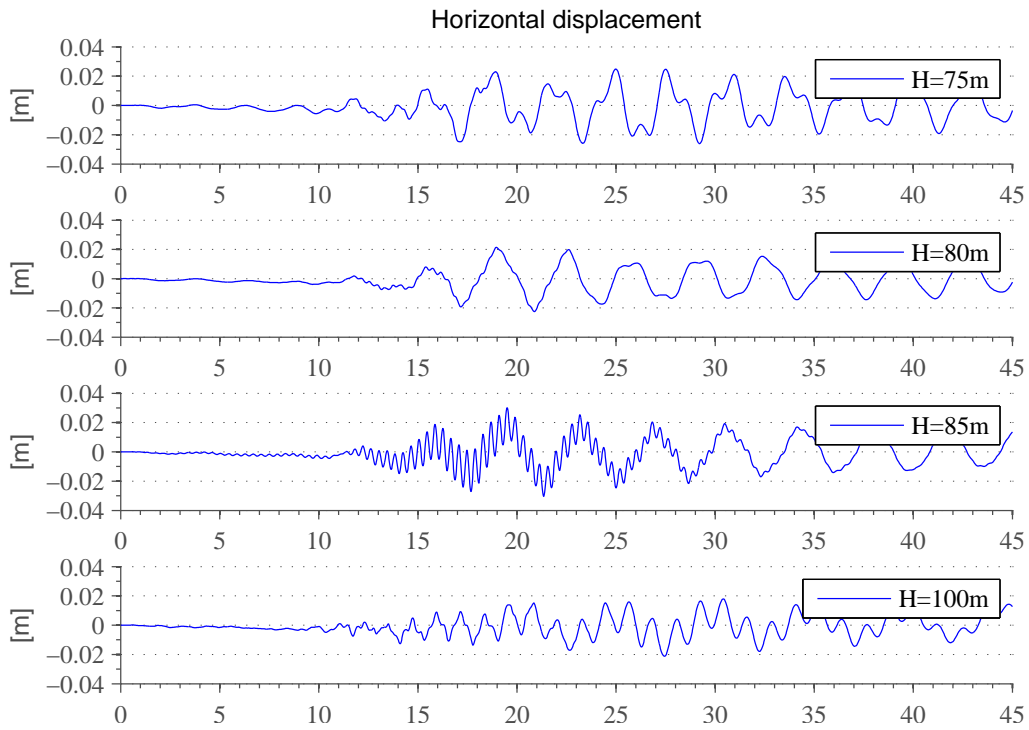


Figure D.23: Nacelle time history acceleration for different tower heights.

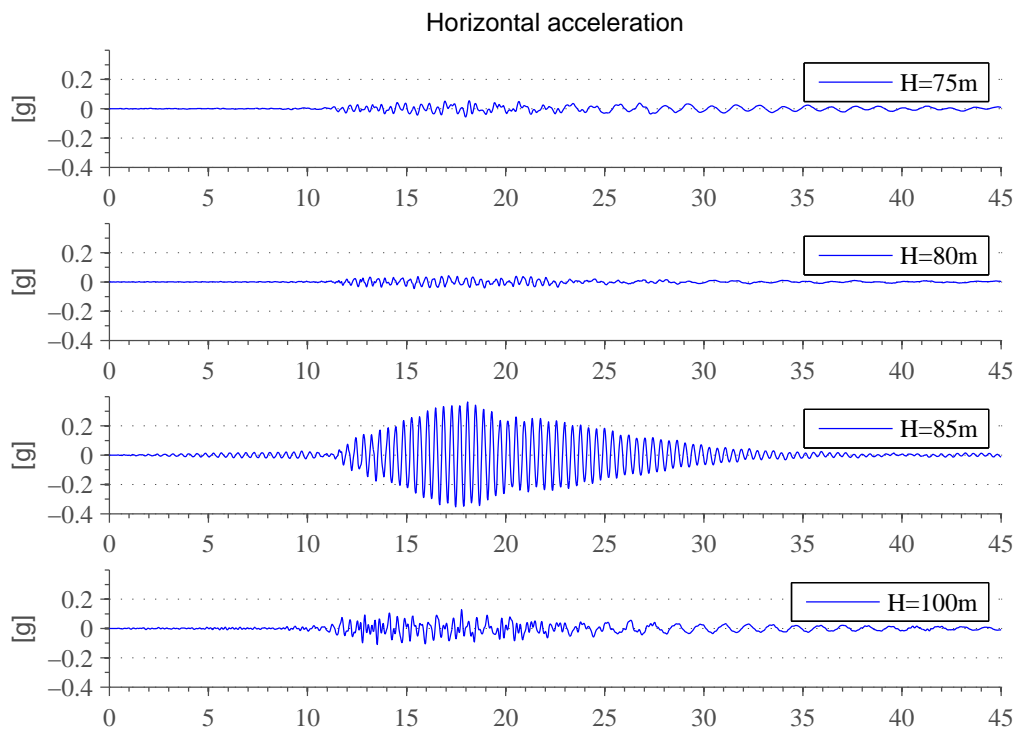


Figure D.24: Nacelle time history acceleration for different tower heights.

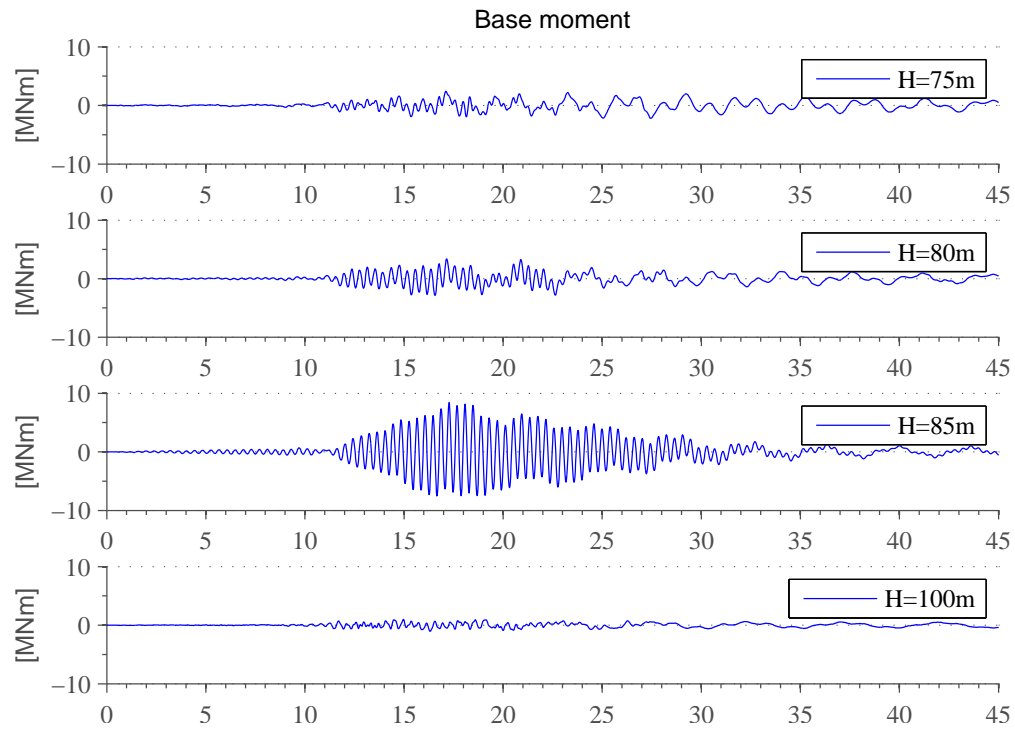


Figure D.25: Base moment (time history) for different tower heights.

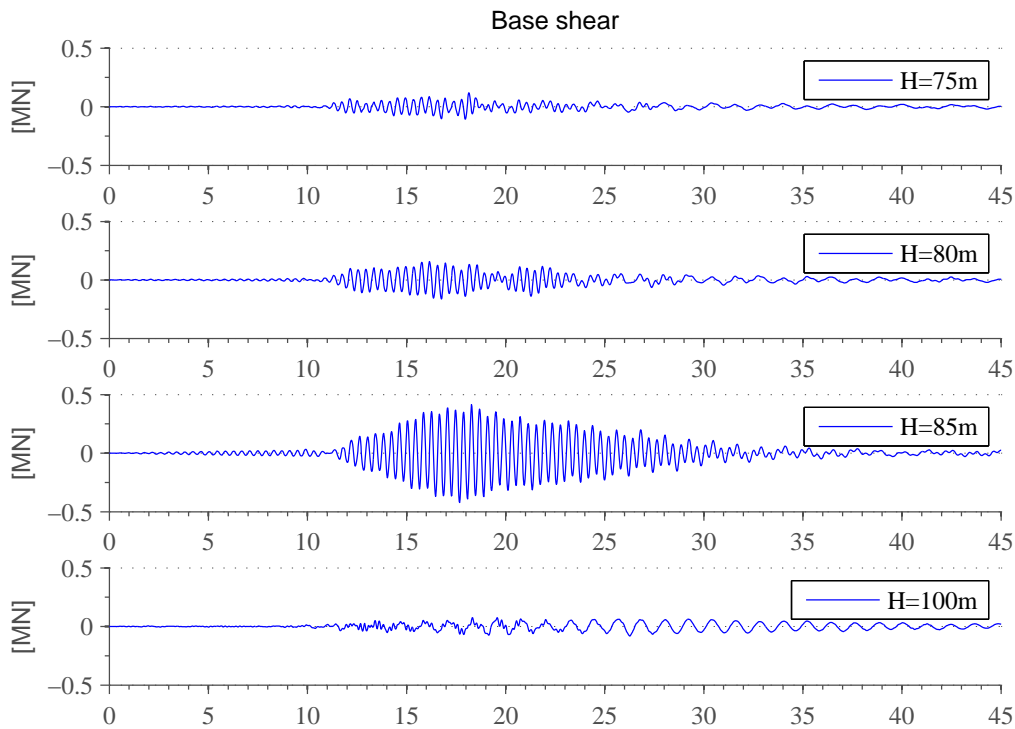


Figure D.26: Base shear (time history) for different tower heights.

D.4 Stiffnesses of the Skirted Foundation with varying geometry

Table D.1 and D.2 give the applied static stiffnesses for different foundation radius' and depths in the parametric study.

Table D.1: Static stiffnesses of the bucket foundation for different skirt radius and constant bucket depth of $D=6m$. $E = 50MPa$ and $V_S = 100\frac{m}{s}$.

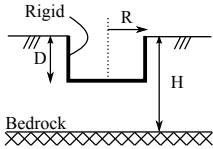
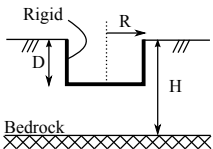
Radius	Ratio	Horizontal	Rocking	Profile
R	$\frac{D}{R}$	k_{HH}	k_{MM}	
[m]	[-]	$10^9[\frac{N}{m}]$	$10^{10}[\frac{Nm}{rad}]$	
4	1.5	0.83	2.37	 <p>Range of validity: D/R < 2 D/H ≤ 0.5</p>
5	1.2	0.94	3.94	
6	1	1.05	6.03	
7	0.86	1.16	8.69	
8	0.75	1.28	11.98	

Table D.2: Static stiffnesses of the bucket foundation for different skirt depths and constant bucket radius of $R=6m$. $E = 50MPa$ and $V_S = 100\frac{m}{s}$.

Depth	Ratio	Horizontal	Rocking	Profile
D	$\frac{D}{R}$	k_{HH}	k_{MM}	
[m]	[-]	$10^9[\frac{N}{m}]$	$10^{10}[\frac{Nm}{rad}]$	
4	0.67	0.88	4.59	 <p>Range of validity: D/R < 2 D/H ≤ 0.5</p>
5	0.83	0.96	5.30	
6	1	1.05	6.03	
7	1.17	1.14	6.78	
8	1.33	1.23	7.53	

Bibliography

- [1] *ABAQUS/CAE User's Manual for version 6.12.*
- [2] *Vestas V90 3.0 MW.*
- [3] Anil K. Chopra. *Dynamics of Structures - Theory and Applications to Earthquake Engineering.* Pearson Prentice Hall, 4 edition, 2012.
- [4] GWEC Global Wind Energy Council. Global statistics, May 2014.
- [5] Ricardo Dobry. Simplified methods in soil dynamics. *Soil Dynamics and Earthquake Engineering*, 61:246–268, 2014.
- [6] Ricardo Dobry and George Gazetas. Dynamic response of arbitrarily shaped foundations. *Journal of geotechnical engineering*, 112(2):109–135, 1986.
- [7] Ricardo Dobry, George Gazetas, and Kenneth H Stokoe. Dynamic response of arbitrarily shaped foundations: Experimental verification. *Journal of Geotechnical Engineering*, 112(2):136–154, 1986.
- [8] PEER Pacific earthquake engineering research center. Peer ground motion database, February 2014.
- [9] George Gazetas. Analysis of machine foundation vibrations: state of the art. *International Journal of Soil Dynamics and Earthquake Engineering*, 2(1):2–42, 1983.
- [10] George Gazetas. Formulas and charts for impedances of surface and embedded foundations. *Journal of Geotechnical Engineering*, 117(9):1363–1381, 1991.

- [11] George Gazetas and Kenneth H Stokoe. Free vibration of embedded foundations: theory versus experiment. *Journal of geotechnical engineering*, 117(9):1382–1401, 1991.
- [12] GeoMotions. Shake2000, June 2014.
- [13] M Harte and B Basu. Foundation impedance and tower transfer functions for offshore wind turbines. *Proceedings of the Institution of Mechanical Engineers, Part K: Journal of Multi-body Dynamics*, 227(2):150–161, 2013.
- [14] Guy T Houlsby, Lars Bo Ibsen, and Byron W Byrne. Suction caissons for wind turbines. In *International Symposium on Frontiers in Offshore Geotechnics*, volume 75, page 94, 2005.
- [15] Lars Bo Ibsen and Morten Liingaard. Prototype bucket foundation for wind turbines-natural frequency estimation. 2006.
- [16] Lars Bo Ibsen, S Liingaard, and Søren A Nielsen. Bucket foundation, a status. *Proceedings of the Copenhagen Offshore Wind*, 2005.
- [17] T Ishihara and MW Sarwar. Numerical and theoretical study on seismic response of wind turbines. In *European Wind Energy Conference and Exhibition*, pages 1–5, 2008.
- [18] Eduardo Kausel, Robert V Whitman, Joseph P Morray, and Farid Elsabee. The spring method for embedded foundations. *Nuclear Engineering and Design*, 48(2):377–392, 1978.
- [19] RS KOURKOULIS, PC LEKKAKIS, FM GELAGOTI, and AM KAYNIA. Suction caisson foundations for offshore wind turbines subjected to wave and earthquake loading: effect of soil–foundation interface. 2014.
- [20] Steven L. Kramer. *Geotechnical Earthquake Engineering*. Pearson Prentice Hall, 1 edition, 1996.
- [21] Søren Madsen, Lars Vabbersgaard Andersen, and Lars Bo Ibsen. Numerical buckling analysis of large suction caissons for wind turbines on deep water. *Engineering Structures*, 57:443–452, 2013.
- [22] Standard Norge. Eurokode 8: Prosjektering av konstruksjoner for seismiske påvirkning. del 1: Allmenne regler, seismiske laster og regler for bygninger. *NS-EN*, 1:2004, 1998.

- [23] Ian Prowell. An experimental and numerical study of wind turbine seismic behavior. 2011.
- [24] Ian Prowell, Ahmed Elgamal, Chia-Ming Uang, J Enrique Luco, Harold Romanowitz, and Edward Duggan. Shake table testing and numerical simulation of a utility-scale wind turbine including operational effects. *Wind Energy*, 2013.
- [25] Ian Prowell, Chia-Ming Uang, Ahmed Elgamal, J Enrique Luco, and Lanhui Guo. Shake table testing of a utility-scale wind turbine. *Journal of Engineering Mechanics*, 138(7):900–909, 2011.
- [26] Jose M Roesset. Stiffness and damping coefficients of foundations. In *Dynamic Response of Structures@ sExperimentation, Observation, Prediction and Control*, pages 1–30. ASCE, 1980.
- [27] Hooman Torabi and Mohammad T Rayhani. Three dimensional finite element modeling of seismic soil–structure interaction in soft soil. *Computers and Geotechnics*, 60:9–19, 2014.
- [28] Edward L Wilson. Three-dimensional static and dynamic analysis of structures. *Computers and Structures, Inc., Berkeley, CA*, 1996.